

Stability analysis of frozen soil slopes considering strain localization

Ali Rostami

A Thesis

In

The Department

Of

Building, Civil, and Environmental Engineering

Presented in Partial Fulfillment of the Requirements

For the Degree of

Master of Applied Science (Geotechnical Engineering) at

Concordia University

Montréal, Québec, Canada

August of 2022

© Ali Rostami, 2022

CONCORDIA UNIVERSITY
School of Graduate Studies

This is to certify that the thesis prepared

By: Ali Rostami

Entitled: Stability analysis of frozen soil slopes considering strain localization
and submitted in partial fulfillment of the requirements for the degree of

Master of Applied Science (Geotechnical Engineering)

complies with the regulations of the University and meets the accepted standards with respect to
originality and quality.

Signed by the final Examining Committee:

_____ Dr. Adel M. Hanna, Chair

_____ Dr. Adel M. Hanna, Examiner

_____ Dr. Attila M. Zsaki, Examiner

_____ Dr. Biao Li, Supervisor

Approved by: _____

Dr. Ashutosh Bagchi, Chair

Department of Building, Civil, and Environmental Engineering

Date:

Dr. Mourad Debbabi, Dean

Gina Cody School of Engineering and Computer Science

ABSTRACT

Stability analysis of frozen soil slopes considering strain localization

Ali Rostami

The study of frozen soil failure behavior has been a major issue to focus on over the past decades since the changing climate was known to be the main reason for the gradual degradation of permafrost (or frozen soil) in cold regions. The assessment of the variation of strength and deformation properties of frozen soils with temperature is very critical in geotechnical applications such as foundation design, slope stability analysis, etc. Over the years, many numerical, laboratory, and field studies have focused on characterizing the behavior of frozen soils at various negative temperatures. In this research, available studies in the literature are reviewed for characterizing appropriate temperature dependent strength and deformation parameters for the stability analysis of frozen soil slopes. Parameters including cohesion c , friction angle φ , Young's modulus E , and Poisson's ratio ν are determined as functions of negative temperature for three different frozen soils, i.e. clay, silt, and sand. These parameters are used as the input data for the 2D plane strain finite element (FE) modeling on the slope stability analysis at different temperatures and the Drucker-Prager (DP) model is applied as the yield criterion. The stability analysis is based on investigating the shear band development, considering strain localization at different temperatures. The results indicate that as the temperature decreases, the strength of slope against shearing and collapse increases. In cases where slope failure occurs, the plastic strain in the close vicinity of slope is significant, leading to developing a curved thin shear zone extending from the top to the toe of slope. This critical zone acts as the slip surface for the slope. At lower temperatures, in general, plastic straining throughout the domain decreases, and the critical shear zone would not develop completely, therefore lowering the possibility of slope collapse (=higher factor of safety). The numerical approach is capable of depicting the deformation and failure characteristics of frozen soil slopes sensitive to temperature changes.

Keywords: Frozen soil failure behavior, permafrost, uniaxial compression test, triaxial compression test, finite element (FE) MATLAB code, frozen slope stability, Drucker-Prager criterion

ACKNOWLEDGEMENTS

First, I would like to express my sincere thanks and gratitude to Professor Biao Li, my thesis supervisor, for all his support, guidance, and advisory throughout this research.

I am extremely grateful to the support provided by my family and friends during this whole period.

I would also like to thank the examination committee for reading this thesis and providing valuable comments. My profound gratitude to Professor Hanna and Professor Zsaki for their guidance.

Finally, I would like to acknowledge the financial support received from the Department of Building, Civil, and Environmental Engineering at Concordia University to make this research study possible.

TABLE OF CONTENTS

LIST OF FIGURES	viii
LIST OF TABLES	xiv
LIST OF SYMBOLS	xvi
1 Introduction.....	1
1.1 Objectives of the current study	6
1.2 Organization of the thesis	7
2 Literature Review	9
2.1 Frozen soil composition and rheology	9
2.1.1 Frozen soil vs. Permafrost.....	10
2.1.2 Mechanical (=strength and deformation) behavior of frozen soils.....	13
2.1.3 Strength of frozen soils	15
2.2 Studies on factors affecting the strength of frozen soils	19
2.3 Studies on frozen soil/rock slope stability	27
3 Theoretical basis and methodology	43
3.1 Classical yield criteria.....	46
3.1.1 The Tresca yield criterion	46
3.1.2 The von Mises yield criterion	48
3.1.3 The Mohr-Coulomb (MC) yield criterion.....	49
3.1.4 The Drucker-Prager (DP) yield criterion	52
3.2 Finite Element Method (FEM).....	54
3.3 The current MATLAB code incorporating FEM for slope stability analysis ...	60

4	Temperature-dependent mechanical properties of frozen soils	66
4.1	Clay soils.....	66
4.2	Silt soils.....	71
4.3	Sand soils	79
5	Results of the finite element (FE) slope stability analysis	86
5.1	Clay soils.....	89
5.2	Silt soils.....	115
5.3	Sand soils	130
6	Summary and recommendations for future work	144
6.1	Conclusions.....	144
6.2	Recommendations for future work	146
	References.....	149

LIST OF FIGURES

Figure 1.1. Degrading permafrost (warmer permafrost, thicker active layer) is a serious threat to the environment, roads, buildings (Hjort et al. 2022).	3
Figure 1.2. Permafrost degradation hazards damaging the infrastructures including the roads, pipelines, buildings, industrial facilities (Hjort et al. 2022).....	4
Figure 1.3. Infrastructure damage in North America due to permafrost degradation: (a) Longitudinal cracking along the Alaska Highway in Yukon, Canada, (b) thermokarst affecting the embankment of the Alaska Highway, Yukon, Canada, and (c) sinkhole in the Iqaluit runway, Nunavut, Canada (Hjort et al. 2022).....	4
Figure 2.1. Soil classification for frozen soils and permafrost samples (Linell and Kaplar 1966 and Johnston 1981).	11
Figure 2.2. Frozen soil classification: (a) Frozen soil classification according to the total volumetric ice content, (b) Schematic representation of frozen soil samples at different volumetric ice contents (Arenson et al. 2007).....	11-12
Figure 2.3. Axial stress-strain curves for frozen Ottawa sand and ice at large strains (Sayles 1974).	21
Figure 2.4. Mohr circles and Mohr envelopes for frozen Ottawa sand and ice. A-E and 1-5 on curves indicate different specimens of sands and ice (Sayles 1974).....	21
Figure 2.5. Log-log scale plot of compressive strength vs. below zero temperature, under different strain rates (Bragg and Andersland 1981).....	24
Figure 2.6. Log-log scale plot of initial tangent modulus E_i vs. below zero temperature, under different strain rates (Bragg and Andersland 1981).....	25

Figure 2.7. Schematic representation of permafrost distribution in a high river bank adjacent to the Mackenzie River (McRoberts and Morgenstern 1974).	28
Figure 2.8. The cross section at the Mountain River slide used in stability calculation (McRoberts and Morgenstern 1974).	29
Figure 2.9. Idealized stability development in ice rich frozen cut slopes (Mageau and Rooney 1984).	30
Figure 2.10. Location of study area and the observed landslide under investigation (Su et al. 2006).	32
Figure 2.11. Undrained shear strength of the active layer normalized by the overburden pressure (Su et al. 2006).	33
Figure 2.12. Slope/W analysis model for the initial slope instability of the observed landslide (Su et al. 2006).	33
Figure 2.13. Stability analysis parameters and results: (a) Undrained shear strength parameters, (b) Slope stability results (Su et al. 2006).	34
Figure 2.14. Temperature profiles from borehole measurement on the Muragl rock glacier (Nater et al. 2008).	36
Figure 2.15. Failure mechanisms for the (a) summer temperature profile with a global factor of safety FOS = 1.22 and (b) winter temperature profile with a global factor of safety FOS = 1.48. Numbers on the x and y axes are in meters (Nater et al. 2008).	37
Figure 2.16. Two-dimensional cross section of embankment slope showing installed monitoring instruments (Siva Subramanian et al. 2017).	40

Figure 2.17. Photo of the national highway slope failure (Siva Subramanian et al. 2017).	41
Figure 2.18. Two-dimensional numerical model for highway slope with boundary conditions (Siva Subramanian et al. 2017).	41
Figure 3.1. Idealized axial stress-strain curve, showing strain hardening (de Souza Neto et al. 2008).	44
Figure 3.2. Hardening function, also called hardening curve for a one-dimensional model (de Souza Neto et al. 2008).	45
Figure 3.3. The Tresca and von Mises yield surfaces in principal stress space (de Souza Neto et al. 2008).	47
Figure 3.4. (a) The π -plane in principal stress space, and (b) The projection of the Tresca and von Mises yield surfaces on the π -plane (de Souza Neto et al. 2008).	48
Figure 3.5. Mohr-Coulomb criterion in $\tau - \sigma$ space (de Souza Neto et al. 2008).	50
Figure 3.6. Mohr-Coulomb yield surface in principal stress space (de Souza Neto et al. 2008).	51
Figure 3.7. The Drucker-Prager yield surface in principal stress space (de Souza Neto et al. 2008).	52
Figure 3.8. The π -plane section of two approximations between the Drucker-Prager and the Mohr-Coulomb yield surfaces (de Souza Neto et al. 2008).	53
Figure 3.9. The finite element model of a 2D body, a thin plate with a hole: The loading on the side walls, the triangular finite element, and two types of mesh generated for the body (Fish and Belytschko 2007).	55

Figure 3.10. Body V subject to applied displacements and tractions.....	57
Figure 3.11. Body V divided into finite elements. Nodes along the sides of the element define its shape to be a square.....	58
Figure 3.12. Reducing the initial boundary value problem (IBVP) to a set of incremental finite element equations (de Souza Neto et al. 2008).	63
Figure 3.13. From the elastoplastic initial value problem (IVP) to the elastic predictor/return-mapping integration algorithm (de Souza Neto et al. 2008).	63
Figure 3.14. (a) Geometry of the slope stability analysis problem, (b) Finite element mesh-generated model with quadrilateral elements refined close to and within the slope's body (de Souza Neto et al. 2008).....	64
Figure 4.1. (a) initial tangent modulus vs. temperature and (b) modulus at 50% strength vs. temperature (Haynes and Karalius 1977).	73
Figure 4.2. Average compressive stress-strain curves for different total water content ranges at $T = -1.67$ °C (Sayles and Carbee 1981).	74
Figure 4.3. Plot of $\log \sigma_m$ vs. $\log (\theta / \theta_0)$ for different strain rates (Zhu and Carbee 1984).	76
Figure 4.4. (a) Initial tangent modulus vs. temperature and (b) tangent modulus at 50% strength vs. temperature (Zhu and Carbee 1984).	77
Figure 4.5. Variation of compressive strength σ_1 as a function of temperature (Parameswaran 1980).	81
Figure 4.6. Variation of initial tangent modulus E_i : (a) with \log (strain rate); and (b) with strain rate (log-log scale) (Parameswaran 1980).	81

Figure 5.1. Finite element mesh-generated model with quadrilateral elements refined close to and within the slope's body, comprising 768 eight-pointed quadrilateral elements with 2405 nodal points.....	86
Figure 5.2. (a) Loading path: Gravity load factor vs. settlement on top of slope, (b) Displacement pattern of slope at failure, (c) Plastic strain throughout the domain.....	88
Figure 5.3. $T = -3^{\circ}\text{C}$: (a) Loading path: Gravity load factor vs. settlement on top of slope, (b) Displacement pattern of slope, (c) Plastic strain throughout the domain.....	91
Figure 5.4. $T = -2^{\circ}\text{C}$: (a) Loading path: Gravity load factor vs. settlement on top of slope, (b) Displacement pattern of slope at collapse, (c) Plastic strain throughout the domain.....	94
Figure 5.5. $T = -4^{\circ}\text{C}$: (a) Loading path: Gravity load factor vs. settlement on top of slope, (b) Displacement pattern of slope at collapse, (c) Plastic strain throughout the domain.....	95
Figure 5.6. Displacement pattern and Plastic strain plots at different negative temperatures.....	96-97
Figure 5.7. Analysis results at $T= -2^{\circ}\text{C}$ for the frozen Kaolinite-Sand: (a) Displacement pattern of slope material, (b) Plastic strain throughout the domain (values shown on the side bar are in percent %)......	101
Figure 5.8. Analysis results at $T= -2^{\circ}\text{C}$ for the frozen Bentonite-Sand: (a) Displacement pattern of slope material, (b) Plastic strain throughout the domain (values shown on the side bar are in percent %)......	101

Figure 5.9. Analysis results at (a) $T = -2\text{ }^{\circ}\text{C}$, (b) $T = -4\text{ }^{\circ}\text{C}$, (c) $T = -6\text{ }^{\circ}\text{C}$, (d) $T = -7\text{ }^{\circ}\text{C}$, (e) $T = -8\text{ }^{\circ}\text{C}$, and (f) $T = -9\text{ }^{\circ}\text{C}$.	104-109
Figure 5.10. Analysis results at (a) $T = -2\text{ }^{\circ}\text{C}$, (b) $T = -5\text{ }^{\circ}\text{C}$, and (c) $T = -10\text{ }^{\circ}\text{C}$.	112-114
Figure 5.11. Analysis results at (a) $T = -2\text{ }^{\circ}\text{C}$, (b) $T = -4\text{ }^{\circ}\text{C}$, (c) $T = -6\text{ }^{\circ}\text{C}$, and (d) $T = -8\text{ }^{\circ}\text{C}$.	116-119
Figure 5.12. Analysis results at (a) $T = -2\text{ }^{\circ}\text{C}$, (b) $T = -4\text{ }^{\circ}\text{C}$, (c) $T = -6\text{ }^{\circ}\text{C}$, (d) $T = -8\text{ }^{\circ}\text{C}$, and (e) $T = -10\text{ }^{\circ}\text{C}$.	122-126
Figure 5.13. Analysis results at $T = -4\text{ }^{\circ}\text{C}$.	129
Figure 5.14. Analysis results at $T = -3.89\text{ }^{\circ}\text{C}$.	133
Figure 5.15. Analysis results at (a) $T = -2\text{ }^{\circ}\text{C}$, (b) $T = -3\text{ }^{\circ}\text{C}$, (c) $T = -4\text{ }^{\circ}\text{C}$, (d) $T = -5\text{ }^{\circ}\text{C}$, and (e) $T = -6\text{ }^{\circ}\text{C}$.	136-140
Figure 5.16. Analysis results at $T = -6\text{ }^{\circ}\text{C}$.	143

LIST OF TABLES

Table 4.1. Mechanical parameters according to the study by Akhtar and Li (2020).	67
Table 4.2 Mechanical parameters of frozen Kaolinite-Sand mixtures according to Girgis et al. (2020).	69
Table 4.3 Mechanical parameters of frozen Bentonite-Sand mixtures according to Girgis et al. (2020).	69
Table 4.4 Mechanical parameters of frozen Kasaoka clay according to Wang et al. (2017).	71
Table 4.5 Mechanical parameters of frozen Fairbanks silt according to Haynes and Karalius (1977).	72
Table 4.6 Mechanical parameters of frozen Fairbanks silt according to Sayles and Carbee (1981).	75
Table 4.7 Mechanical parameters of frozen silt according to Yugui et al. (2016).	78
Table 4.8 Mechanical parameters of frozen Ottawa sand according to Sayles (1974). ...	80
Table 4.9 Mechanical parameters of frozen sand from Qinghai-Tibet according to Yang et al. (2010b).	85
Table 5.1. Mechanical parameters for the unfrozen soil slope material.	86
Table 5.2. Mechanical parameters based on the approach by Akhtar and Li (2020).	89
Table 5.3. Mechanical parameters for an experimental frozen clay according to Li et al. (2015) and Bai et al. (2020).	92
Table 5.4. Mechanical parameters for the frozen Kaolinite-Sand according to the approach by Girgis et al. (2020).	99

Table 5.5. Mechanical parameters for the frozen Bentonite-Sand according to the approach by Girgis et al. (2020).	99-100
Table 5.6. Mechanical parameters for the frozen clay according to Li et al. (2019).	102
Table 5.7. Mechanical parameters for the frozen high plasticity Kasaoka clay.	111
Table 5.8. Mechanical parameters of the frozen Fairbanks silt according to Haynes and Karalius (1977).....	115
Table 5.9. Mechanical parameters of the frozen Fairbanks silt according to Zhu and Carbee (1984).....	120
Table 5.10. Mechanical parameters of frozen silt according to Yugui et al. (2016).	127
Table 5.11. Mechanical parameters of frozen Ottawa sand determined based on the study by Sayles (1974).....	131
Table 5.12. Mechanical parameters of frozen Ottawa sand determined based on the study by Parameswaran (1980).....	135
Table 5.13. Mechanical parameters of frozen sand based on the study by Yang et al. (2010).....	141

LIST OF SYMBOLS

c	Cohesion term of shear strength (kPa, MPa)
φ	Internal friction angle ($^{\circ}$)
$E, E_{50\%}, E_i$	Young's modulus (MPa)
E_i	Initial tangent modulus (MPa)
$E_{50\%}$	(secant or tangent) modulus at 50% peak strength (MPa)
ν, μ	Poisson's ratio
T	Temperature in degrees of centigrade $^{\circ}\text{C}$
G_s	Specific gravity of soil grains
$\dot{\varepsilon}$	(axial) strain rate (/sec)
E^{ep}	Elastoplastic tangent modulus (MPa)
ε^p	Plastic strain (in %)
$\Phi(\sigma, A)$	Yield function
$\Psi(\sigma, A)$	Plastic potential function
η, ζ	Material parameters as functions of c and φ
γ	Unit (=specific) weight (kN/m^3)
ξ	Gravity load (scalar) factor
σ_1, σ_3	Maximum and Minimum principal stresses in Mohr-Coulomb criterion (kPa, MPa)
ω	Water content (in %)
γ_d	Dry unit weight (kN/m^3)
ρ_d	Dry density (kg/m^3)
σ_m	Peak compressive strength (kPa, MPa)
LL	Liquid limit (in %)
PL	Plastic limit (in %)

e	Void ratio
n	Porosity
w_i	Volumetric ice content (in %)
$\varphi'_{\text{initial}}$	Effective internal friction angle for unfrozen condition (°)
φ'	Effective internal friction angle (°)
P_a	Atmospheric pressure = 101.325 kPa
$\delta\xi$	Load factor increment
S	Degree of saturation (in %)
$\sigma_1 - \sigma_3$	Deviatoric stress in triaxial compression test (kPa, MPa)
ε_1	Axial strain (in %)

1 Introduction

Geotechnical (and construction) engineering in cold regions can be very different from the common engineering practice in temperate climates where principles of soil mechanics have been well understood and implemented for a very long time. In cold regions, heat flow is very important in terms of freezing and thawing of the ground, and soil moisture experiences a phase change which might take place with the migration of pore water (Barker and Thomas 2013). These processes can cause dramatic changes in physical properties of the soil/ground. The frozen ground in cold regions is divided into three categories: 1- Seasonally frozen ground, 2- Continuous permafrost (is widespread everywhere), and 3- Discontinuous permafrost (exists only in some areas). According to Barker and Thomas (2013), most of Alaska and other cold areas have permafrost (permanently frozen) overlain by the shallow surface (active) layer of seasonally changeable temperature, in subarctic regions there exists sporadic/discontinuous permafrost (covering less than 50% of landscape), and continuous permafrost existing in high arctic areas.

In a recent review by Hjort et al. (2022), it is mentioned that about one-fifth of the exposed land surface in the northern hemisphere is covered by permafrost which is experiencing temperature increase with the rate of $0.3\text{--}1^\circ\text{C}$ per decade. This accordingly increases the depth of active layer on top of permafrost. In addition to environmental effects, permafrost degradation (=warming and thawing) can be a serious threat to infrastructures namely buildings, roads, pipelines, etc. For instance, wet fine-grained soils within the active/top layer, can heave 1–40 cm per year during the freezing process, leading to the possible infrastructure's deformation and failure. On the other hand, during the thawing process, the frozen soils of high ice contents experience a substantial strength and volume change, which results in the possible deformation and damage of infrastructures. Therefore, for design purposes, the frozen ground conditions during the entire lifespan of the structure should be carefully considered. In Figure 1.1, a schematic representation of degrading permafrost and the

resulting natural, environmental, societal hazards/risks is shown. In another figure, more specific hazards and risks related to frozen ground (permafrost) degradation are illustrated, namely thaw-related hazards such as development of taliks (=layer or body of unfrozen permafrost occurring locally), mass wasting on slopes, and thermal erosion along riverbanks (Fig. 1.2). In general, the strength of frozen soil increases as the temperature decreases (=becomes more negative). This is mainly attributed to the higher ice cementation (=adfreeze bond strength) within the frozen soil medium at lower temperatures. As the temperature increases, on the other hand, and surpasses the freezing point, the strength reduces significantly, and the soil is no longer able to satisfy engineering stability. According to Hjort et al. (2022), changes in (or warming of) warm permafrost regions, with temperatures above -3°C , are most critical for infrastructures because the temperature is close to the melting/freezing point. This results in the significant reduction of the freeze bond strength and therefore the frozen ground's bearing capacity.

Instability/failure of slopes on frozen grounds, because of permafrost warming and degradation, can have serious effects on construction projects, esp. with shallow foundations in transportation infrastructures. Slope processes can range from slow mass movements, like permafrost creep, to more rapid ones such as landslides and earthflows (Hjort et al. 2022).

In North America, more than 50% of Canadian and 80% of Alaskan land surfaces are characterized by permafrost, where unlike Russia the population is sparse and large industrial centres are rare. This situation has required horizontal or linear transportation infrastructure including long roads, airstrips, pipeline systems (Hjort et al. 2022). The impacts from the respective construction processes have led to several effects such as surface distortions, slope instabilities, cracks at the edge of embankments, lateral embankment spreading, sinkholes, water ponding along roadsides, etc. (shown in Fig. 1.3). The corresponding estimated value of infrastructure at risk, and prone to damage, owing to climate/permafrost warming has

been more than about 50 million Canadian dollars per year, which is a considerable amount (Hjort et al. 2022).

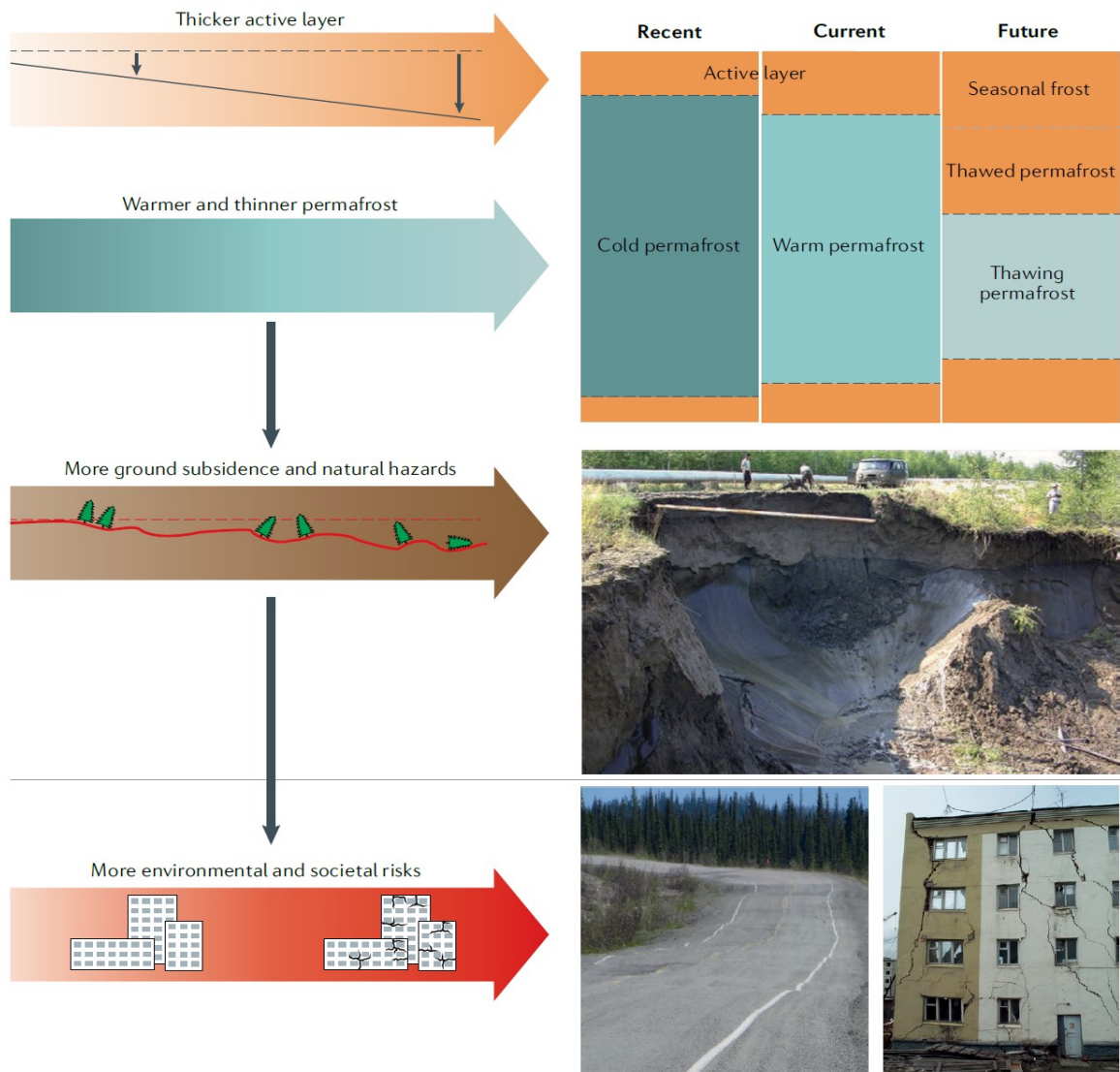


Figure 1.1. Degrading permafrost (warmer permafrost, thicker active layer) is a serious threat to the environment, roads, buildings (Hjort et al. 2022).

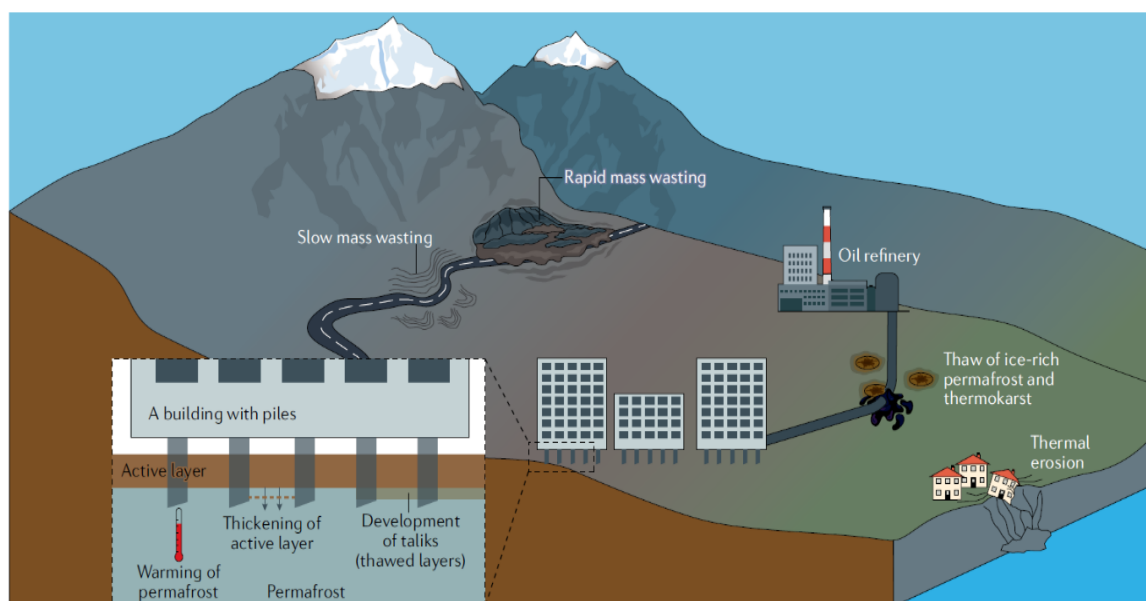


Figure 1.2. Permafrost degradation hazards damaging the infrastructures including the roads, pipelines, buildings, industrial facilities (Hjort et al. 2022).



Figure 1.3. Infrastructure damage in North America due to permafrost degradation: (a) Longitudinal cracking along the Alaska Highway in Yukon, Canada, (b) thermokarst affecting the embankment of the Alaska Highway, Yukon, Canada, and (c) sinkhole in the Iqaluit runway, Nunavut, Canada (Hjort et al. 2022).

Over the years, different aspects of frozen soil strength characteristics have been studied by many researchers (e.g., Andersland and AlNouri 1970, Ting et al. 1983, Arenson et al. 2004, Arenson and Springman 2005a, Arenson and Springman 2005b, Girgis et al. 2020). Some researchers namely Yong (1962), Haynes and Karalius (1977), Parameswaran (1980), Li et al. (2004), and Girgis et al. (2020) have performed unconfined uniaxial compression tests on undisturbed and/or artificially prepared frozen soil samples, at different frozen temperatures, under various axial strain rates. There are other studies having focused on the triaxial compression tests of

frozen soils (e.g., Sayles 1974, Arenson et al. 2004, Yugui Yang et al. 2016, and Wang et al. 2017). Triaxial tests were conducted at different negative temperatures, under different confining pressures and strain rates. The results from the unconfined uniaxial and the triaxial compression tests have been reported/presented in the forms of stress-strain curves (for various temperatures, strain rates, and confining pressures), compressive strength-temperature curves (for different strain rates), Young's modulus vs. temperature curves (for different strain rates or confining pressures), etc. The mechanical properties of frozen soils including the deformation and shear strength parameters can be determined based on these results/curves. For instance, Haynes and Karalius (1977) conducted uniaxial compression tests on frozen Fairbanks silt samples and obtained compressive strength vs. temperature and Young's modulus vs. temperature curves, under two different axial strain rates. Parameswaran (1980) performed uniaxial unconfined compression tests on frozen saturated Ottawa sand (at different temperatures and under a wide range of strain rates) and obtained tangent modulus vs. temperature and compressive strength vs. temperature curves. In another study, by Girgis et al. (2020), the results obtained from a series of uniaxial compressive tests on frozen sandy clays, at different temperatures and under three different strain rates, were presented as compressive strength vs. temperature, Young's modulus vs. temperature, and Poisson's ratio vs. temperature curves. These parameters can be used for investigating the bearing capacity, strength, and stability in geotechnical problems if the respective test conditions are applicable to those specific problems.

The issue of slope stability in cold regions is very critical and has been studied by several researchers over the past decades (e.g., McRoberts and Morgenstern 1974, Nater et al. 2008, Subramanian et al. 2017). In this regard, it is really important how the strength parameters are defined and used for the stability analysis of frozen soil slopes. For example, Nater et al. (2008) proposed an approach for determining the shear strength parameters cohesion c and friction angle φ for the analysis of frozen granular/sandy soil slopes. Their results mostly rely on the published data and results

from laboratory tests on undisturbed samples of (ice-rich Alpine) permafrost soils obtained/reported by Arenson et al. (2004) and Arenson and Springman (2005a, 2005b). They considered the Mohr-Coulomb yield criterion as the strength model for the slope material, and next, they performed a numerical simulation of a profile from the Muragl rock glacier in Switzerland (using the program Slope/W for their limit equilibrium analysis). However, previous studies did not present the shear failure transition processes in slopes at different frozen conditions. A detailed study on the strain localization in slopes at different temperatures requires a comprehensive summary of the temperature-dependent mechanical properties.

1.1 Objectives of the current study

The main objectives of this research study are as follows:

- 1) To completely investigate studies available in the literature to determine how the strength and deformation properties of frozen (clay, silt, sand) soils would change as a function of (below zero) temperature which is considered the main influencing factor in this regard.
- 2) To derive/determine the mechanical parameters cohesion c , friction angle φ , Young's modulus E , and Poisson's ratio ν for several frozen soils at different negative temperatures, and to use them as the main required parameters for the slope stability analysis.
- 3) To use the afore-mentioned mechanical parameters as the input data for the finite element (FE) MATLAB code incorporating the Drucker-Prager (DP) yield criterion with stress-strain behavior at small strains and considering associative plasticity. A slope stability problem will be simulated using the FE MATLAB code with the focus on shear band development by considering (plastic) strain localization at different negative temperatures.

1.2 Organization of the thesis

This thesis is organized into six chapters:

Chapter 1 is the introductory part of the thesis, providing a general overview on the importance of correctly understanding the strength characteristics of frozen soil in cold regions. In this chapter, the background, the objectives, and finally the organization of the research study are presented.

Chapter 2 contains a review of many available numerical, laboratory, and field studies in the literature, focusing on the rheology of frozen soil, strength and deformation characteristics of frozen soil, influencing factors on compressive strength of frozen soil, and stability of frozen soil (or permafrost) slopes. Several case studies, their methodology, assumptions, and results are presented.

Chapter 3 focuses on the theoretical basis and methodology of the research study. In this chapter, initially, four yield criteria (Tresca, von Mises, Mohr-Coulomb, and Drucker-Prager) commonly used in engineering applications are explained. Then, the basics and fundamentals of finite element method (FEM) are presented. Finally, the MATLAB code incorporating FEM, in order to perform numerical simulations of slope stability, is introduced. In this chapter the geometry of the slope problem considered for this study is explained as well.

Chapter 4 covers and discusses several studies from the literature, having reported the results of tests on different frozen (clay, silt, and sand) soils. The variation of strength and deformation parameters namely compressive strength σ_c , cohesion c , friction angle φ , Young's modulus E , and Poisson's ratio ν with temperature are investigated, and the respective plots or formulae are presented.

Chapter 5 explains the analysis procedure in this study. The data presented in Chapter 4 are mostly used in this chapter as the input parameters for the FE MATLAB code. The analysis of slope stability is performed for each set of parameters which corresponds to a specific frozen soil and negative temperature. The plots for the results are presented, and the pattern and value of the obtained data are

discussed in detail. The plots, i.e. the outputs from MATLAB code, are presented with a consistent coloring (in many cases colorbars are used) for the sake of easy comparison.

Chapter 6 presents a summary of thesis findings, the overall conclusions obtained from this study, and a few suggestions/recommendations for future research works.

2 Literature Review

The earliest research studies on the properties of frozen soils go back to the 19th century. These studies were carried out mainly because of two major developments: the industrial revolution expanding more towards the remote northern areas, and the artificial ground freezing (AGF) being introduced as a method of temporary support construction for structures and openings (Arenson et al. 2007).

The first published study on the existence of permafrost within the Shergin Well was conducted by von Baer (1838). Artificial ground freezing (AGF) was employed in Wales (in 1862) and in Germany (in 1883) by Potsch, where there are many examples of AFG being used to improve soil properties, and to date, it is being employed for a wide range of applications in geotechnical engineering (Harris 1995). Publications by Sumgin (1927), Taber (1929, 1930), and Beskow (1935) were the pioneers in presenting the fundamental knowledge of permafrost and frozen soil. Some basic concepts introduced in these early studies have been confirmed years later by others, such as Black and Hardenberg (1991).

In recent years, rapid climate change and global warming have caused new impacts on Arctic infrastructure and coastal zones, and problems such as permafrost degradation, where slope instabilities have been recorded in mountainous areas (Haeberli et al. 1997). These are new challenges demanding a much deeper knowledge and understanding of the behavioural properties of frozen soils. As a result, a large number of field, laboratory and numerical studies on different frozen soils have been conducted, and their results are reported in the literature.

2.1 Frozen soil composition and rheology

The mechanical and deformational behavior of frozen soils depends upon a variety of factors, including stress and temperature histories, and the actual composition of the frozen soil. These aspects need to be considered carefully when analysing the response of a frozen soil medium (Arenson et al. 2007).

2.1.1 Frozen soil vs. Permafrost

A frozen soil is a soil that has been cooled down to a point where the pore water turns into ice, implying that a liquid phase must exist in the porous space of soil and this pore liquid undergoes the phase change (Arenson et al. 2007). On the other hand, permafrost, as defined by Muller (1947) and accepted by others such as van Everdingen (1998, 2005), is the “ground (soil and/or rock with possible ice and organic material) that remains at or below 0°C for at least two consecutive years”. This definition of permafrost, clearly, does not talk about the physical state within the ground, and for example a dry soil or rock which meet the temperature and time requirements of permafrost, can behave similarly to their unfrozen state (Arenson et al. 2007). In addition, with regard to the pore water salinity and the likelihood of the pressure melting to happen, the freezing temperature might become even lower than 0°C, leading to the soil remaining in the unfrozen state at temperatures below zero. Therefore, it’s essential to consider the actual state of water in a soil when it comes to freezing temperatures. Accordingly, not every frozen soil meets the requirements of being known as permafrost, e.g. seasonally or temporally frozen soils which are of high engineering importance.

An early engineering classification for frozen soils introduced by Linell and Kaplar (1966), then modified by Johnston (1981), is shown in the figure below (Fig. 2.1). Sayles et al. (1987) added some guidelines to this classification and the index testing of frozen soils. Such a classification system for frozen soils is very important in engineering applications, and yet it needs to be further developed, so that it will be based on tests performed on adequately large frozen soil samples in order to cover “the more general stratigraphy that may control the mechanical behavior of frozen soil medium” (Arenson et al. 2007).

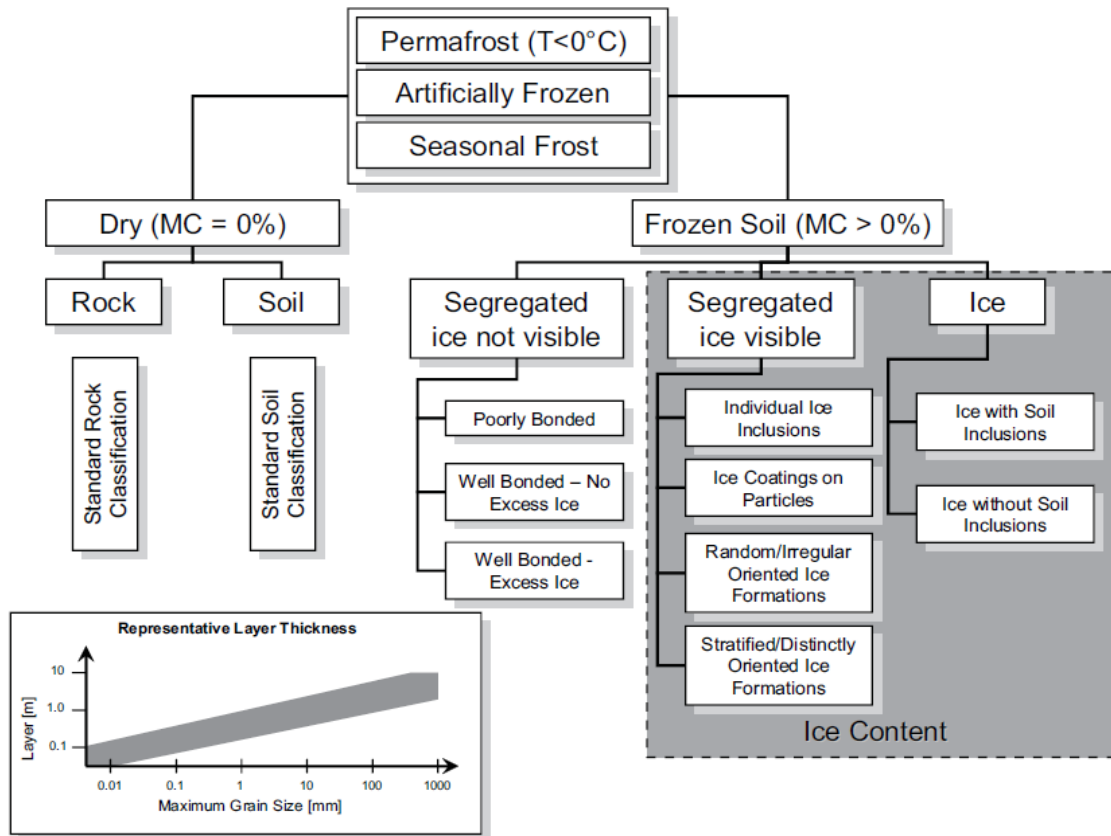
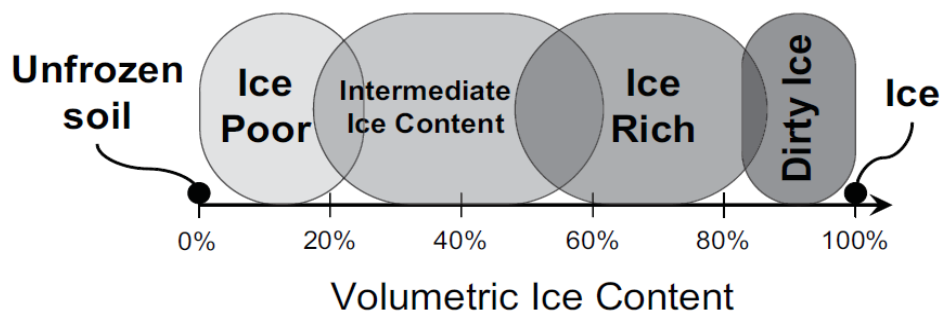
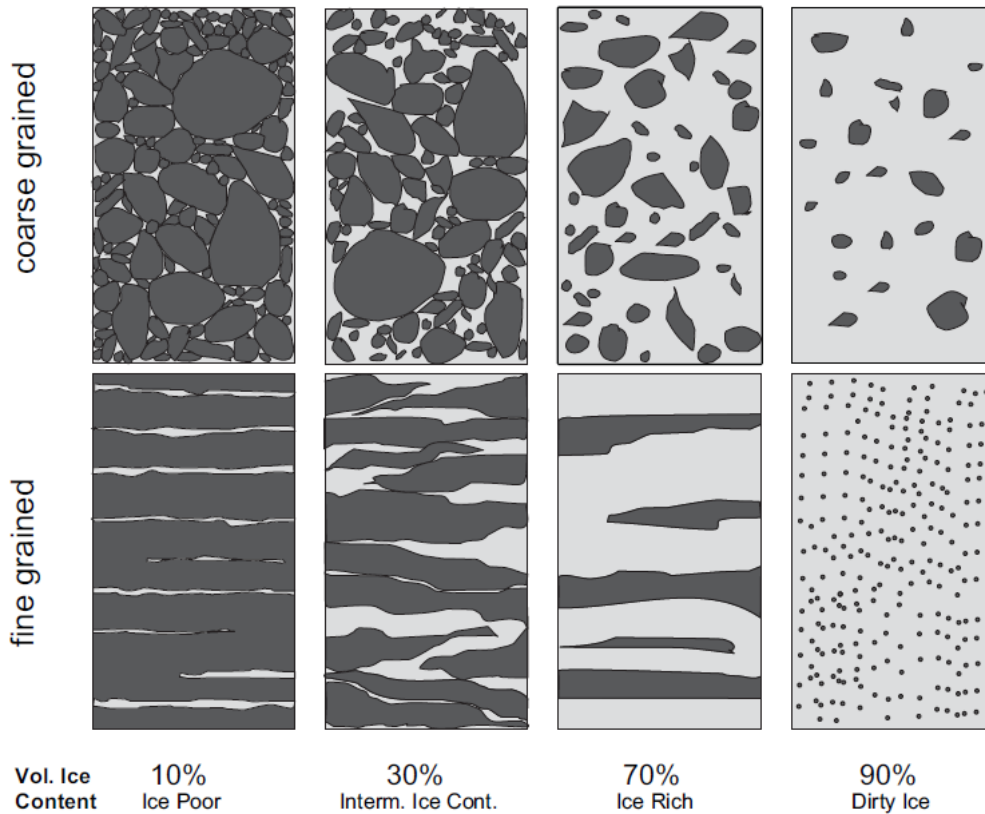


Figure 2.1. Soil classification for frozen soils and permafrost samples (Linell and Kaplar 1966 and Johnston 1981).

In the following figure, a schematic illustration is presented (Fig. 2.2a) as a general classification of frozen soils at different volumetric ice contents. It is obvious that “there is a gradual transition between the regions, which depends on factors such as grain size, form of ice, unfrozen water content, temperature, or other possible solutes in the pore water” (Arenson et al. 2007). In Figure 2.2b, another schematic representation is presented, for two different frozen soil types: coarse-grained (and non-frost susceptible) and fine-grained frost susceptible soils.



(a)



(b)

Figure 2.2. Frozen soil classification: (a) Frozen soil classification according to the total volumetric ice content, (b) Schematic representation of frozen soil samples at different volumetric ice contents (Arenson et al. 2007).

In the freezing process, within the transition from an unfrozen soil to a frozen one, generally, the coarse-grained and the fine-grained soils behave differently. The particle structure of a coarse-grained soil, when experiencing below-zero temperatures, changes very slightly. This is because as the water changes to ice, the volume increases by 9%, and since the hydraulic conductivity of a coarse-grained soil is high, excess water drains and the soil structure remains almost the same (Arenson et al. 2007). In case of a fine-grained soil, on the other hand, because of their lower hydraulic conductivity and higher surface activity, the freezing process affects the soil structure and the ice lens formation significantly. The volume increase of the soil due to freezing results in uplift or frost heave, and the excess pore water developed during the thawing process leads to a strength loss and deformation of the soil. Accordingly,

these soils are classified as frost susceptible and thaw weakening materials (Arenson et al. 2007).

There are many studies available in the literature focusing on frost heave and frost susceptible soils, including the ones based on laboratory and field tests conducted by Hermansson (2004), and Hermansson and Guthrie (2003, 2005).

A concept named the “segregation potential” is widely used in engineering applications related to frost heave and frost action prediction. This concept, initially presented by Konrad and Morgenstern (1980, 1981), is considered as a soil parameter which corresponds to the average size of fines fraction, the specific surface area of fines fraction, and the ratio of water content to liquid limit (Konrad 1999).

2.1.2 Mechanical (=strength and deformation) behavior of frozen soils

The behavioral models initially proposed to depict the mechanical response of frozen soils were not capable of providing a quantitative description of the actual deformation process, because they could not incorporate different aspects of behavior of a frozen soil, particularly its non-linearity (Arenson et al. 2007). Gold (1970) explained about four different stress-strain responses of ice, depending mainly on the applied strain rates. Many more recently published studies on ice-rich permafrost soil samples (Arenson and Springman 2005) and artificially frozen soils (Arenson et al. 2004) confirm this behavior. Also, soil particles influence greatly the stress-strain behavior of a frozen soil medium. Therefore, in addition to the applied strain rate, volumetric ice content plays a significant role within the strength characteristics of a frozen soil.

Besides the applied strain rate and the volumetric ice content, there are a number of other factors which play an important role in the stress-strain behavior of frozen soils. Amongst these factors, ice content is directly related to the unfrozen water content existing within the frozen soil medium. Knowing the ice content and the initial water content of a frozen soil, the amount of the unfrozen water content can be determined almost exactly. The unfrozen water content depends heavily on salinity,

temperature, grain size, and pressure (or stress level) within the frozen soil (Williams 1964; Anderson and Tice 1972; Watanabe and Mizoguchi 2002). According to different studies including the ones conducted by Williams (1967) and Anderson and Tice (1972), the unfrozen water content can be high even at temperatures well below 0°C, the water being present as adsorbed water films around the soil particles or as free water in pores, where the smaller soil particles the higher the unfrozen water content. The chemistry of the pore water itself might cause the freezing point depression to occur, further increasing the unfrozen water content within the frozen soil medium (Arenson et al. 2007). An increase in the unfrozen water content means a reduction of the ice content and ice bonding between particles, which reduces the apparent cohesion and therefore the shear strength of the frozen soil. Since water is known to be incompressible, while existing in the unfrozen state within the frozen soil medium, it can transfer positive and negative stresses between the soil particles and the pore ice. When water drainage from the frozen soil medium is possible, any excess pore water pressure (generated for example because of the freezing process or a modification in the loading condition) can dissipate, which finally leads to a volume change of the frozen soil (Arenson and Springman 2005a). A research study on the strength of frozen soils by Hivon and Segó (1995) confirms that the frozen soil structure and the distribution (and location) of the unfrozen water throughout the frozen soil medium can greatly influence the mechanical behavior. Studies by Stahl and Stadler (1997), Konrad and McCammon (1990), and Arenson et al. (2005) demonstrate that the location of the unfrozen water within the frozen soil medium heavily depends on how the sample initially freezes. Furthermore, regarding the salinity of pore water/ice content, in a study by Arenson and Segó (2006), on the characteristics of saline and non-saline frozen soils, it is shown that the ice structure in saline frozen soils is more fragile compared to non-saline soils.

Arenson et al. (2007) note that due to the great variety of mechanical responses of different frozen soils, generalization of the behavioral characteristics from one site or project to other frozen soil engineering applications is not

recommended. Boundary conditions such as temperature and strain rate need to be carefully evaluated for each specific problem under investigation.

2.1.3 Strength of frozen soils

It is noted by Sayles (1974) that “strength and deformation of frozen soils, as with unfrozen cohesive soils, depend upon both the cohesion and the internal friction of the component materials”. According to Vyalov and Tsytoovich (1955), the cohesion component in frozen soils can be attributed to molecular attraction forces between particles, physical or chemical cementing of particles together, and cementing of particles by the pore ice formation (i.e. ice bonds). The cementation by ice is due to the bonds between the ice crystals and the soil particles (being surrounded by unfrozen water films), implying that the unfrozen water which is under the influence of molecular forces of the soil particles can transmit normal and some shear forces between the solid ice and the solid soil grains. As a result, the cohesion of frozen soils depends heavily on the amount, strength, and area of pore ice content in contact with soil particles. The internal friction, on the other hand, depends upon ice content, soil grain size, shape, arrangement and distribution, and the number of soil grain to grain contacts.

Regarding the several mechanisms governing the strength of frozen soils, there are many studies available in the literature. According to Arenson et al. (2007), at low normal stresses, strain softening controls the behavior of frozen soil, which as the normal stress increases, changes into strain hardening, normally leading to a higher strength level. As normal stress increases to even higher values, the pressure melting of the pore ice occurs, which initially is due to localized stress concentrations on and in the vicinity of the shear planes, and gradually develops throughout the entire (frozen soil) medium. At each stage, the behavior of the frozen soil can be affected by the soil particles within the medium, their percentage by volume, arrangement, etc. In pure ice (shown in Fig. 2.2a) samples, under high normal stresses, the shear stress can be mobilized as the pressure melting begins. Some researchers including Arenson and Springman (2005a), Hooke et al. (1972), and Nickling and

Bennett (1984) suggest that the dirty ice (shown in Fig. 2.2) samples show a decrease in strength probably because the low percentage of soil particles might not allow the fully development of cohesion strength by the pore ice. As the soil particles increase within the frozen soil medium, so that they are in contact with each other (e.g. in ice rich samples or soils with intermediate ice content shown in Fig. 2.2), structural hindrance has the chance to develop at large strain values, resulting in a higher strength of frozen soil, and, when pressure melting occurs at high stress levels, the soil skeleton would take control and contribute to developing the stresses and the strength of the medium (Arenson et al. 2007). In samples of low pore ice content (i.e. ice poor shown in Fig. 2.2), as long as the ice cementation exists between the soil particles, the peak strength of the frozen soil medium can be very high. However, when the ice bonds are broken, for example at high stress levels where pressure melting occurs, the soil skeleton would increasingly dominate the strength characteristics and only a strength equal to the unfrozen state strength would be developed. This situation is very similar to the large strain behavior of frozen soils. Based on different studies and observations, it is concluded that the strength of a frozen soil at (very) large strains is similar to the strength of the unfrozen state, and the mechanism (or mechanisms) governing the strength are almost the same (Arenson et al. 2007). This is mainly because at large strains, the ice bonds and cementation are broken, and ice granules and soil particles act and dilate together, as confirmed by the results of direct shear tests on frozen sands conducted by Yasufuku et al. (2003), where they have also reported an expansion of the shear zone due to crack propagation. Finally, in samples with zero ice content (as in unfrozen soils), obviously there is no ice bonds and cementation between the soil particles, therefore no corresponding cohesion, which significantly influences the peak strength at low normal stresses and leads to a large drop in soil resistance.

Many researchers have worked on strength models for frozen soils. For instance, Fish and Zaretsky (1997) proposed a model based on the Mohr-Coulomb (MC) failure criterion, which all its three parameters (angle of friction, cohesion, and

ice melting pressure) are temperature dependent. However, some researchers (including Ladanyi 1972; Andersland and AlNouri 1970) have proposed that the dependence of the friction angle of frozen soil on temperature, strain rate and time, is negligible. Based on this hypothesis, Arenson and Springman (2005b) employed the MC failure criterion and presented separate formulas for the strength parameters of frozen soil, where the friction angle is determined as a function of volumetric ice content and the friction angle of the unfrozen state, and the cohesion is a function of temperature, strain rate, ice content, and cohesion value at a reference temperature below 0°C.

Arenson et al. (2007) have summarized a few general trends which are commonly observed in the strength characteristics of most frozen soils:

- Under low confining pressures, the strength of the frozen soil is higher than the strength at the unfrozen state, which is related to the cohesion strength of the pore ice matrix.
- When the volumetric ice content is 100% (i.e. pure ice, as shown in Fig. 2.2a), the strength is nearly independent of the confining pressure.
- The shear strength of frozen soil normally increases with a decrease in volumetric ice content. For the ultimate shear strength (i.e. strength at large strain), the increase of strength is noticeably observed at higher confining pressures, while for the peak strength the increase of strength is confirmed to occur under unconfined compression condition (Goughnour and Andersland 1968).
- The maximum value for the ultimate shear strength is reached at low volumetric ice contents, because both the dilatancy of the soil and the cohesion strength due to the pore ice matrix are well developed.

Another important issue is the effect of *time* on mechanical characteristics of frozen soils. Time has a significant influence on frozen soil strength and deformation because the composition of the frozen soil may change with stress, and over time,

consolidation occurs due to water migration. Also, already broken ice bonds might refreeze, leading to strengthening of the frozen soil. It is very important to know about the freezing history of soils. For example, different frozen soils, a permafrost existed for many years, an artificially frozen soil recently frozen using freezing pipes, and a soil frozen through the cold winter, might have the same unfrozen characteristics, but clearly their totally different freezing processes affect their frozen behaviors (Arenson et al. 2007). Similar to the large-strain strength mentioned earlier, the long term (i.e. time dependent) strength of a frozen soil approaches the large-strain strength of the unfrozen state (Arenson et al. 2007). There are many studies available in the literature on the effect of time on the strength of frozen soils. For instance, Vyalov (1963) proposed a formulation for the unconfined compression strength of frozen soil as a function of time, using two temperature- and strain rate-dependent soil parameters. Details about the effect of time on the behavior of frozen soils are normally discussed within the context of creep behavior. Creep is defined as the time dependent deformation of materials (here, frozen soils) under constant stress conditions, which consists of three main stages of primary, secondary (or steady state), and tertiary creep.

Many researchers have performed studies on creep behavior of ice and frozen soils. For example, Glen (1955) proposed a power law for the steady state creep rate of glacier ice. Voytkovskiy (1960) presented an empirical relationship for the creep strain rate with temperature, which others have employed in their studies as well (e.g. Hooke et al. 1980; Segoo and Morgenstern 1983). In addition, Arenson and Springman (2005b), and Arenson et al. (2004) confirmed the validity of the proportionality equation, proposed by Voytkovskiy (1960), for the alpine permafrost. Normally, in order to fairly represent and characterize the mechanical behavior of frozen soils, constant strain rate and constant stress (creep) tests are conducted on frozen soil samples. Ladanyi (1972) and Ladanyi and Johnston (1973) have shown that for frozen soils, similar to unfrozen soils, there is a two-way dependency between the constant strain rate and creep test results. This assumption, which has been also confirmed by

more recent studies (e.g. Arenson and Springman 2005b), mentions that it is possible to estimate the creep data of a frozen soil based on a series of constant strain rate tests.

2.2 Studies on factors affecting the strength of frozen soils

Over the past years, many researchers have focused on experimental and/or numerical study of different factors influencing the strength and deformation characteristics of frozen soils.

Yong (1962) performed two types of strength tests, uniaxial unconfined compression test and ring shear test, on three different types of frozen soils: sand, silt, and clay. Sand samples were prepared in waxed containers, and they were fully saturated in both dense and loose states before freezing. Clay and silt samples were prepared by consolidation or compaction, and only consolidated clay samples were fully saturated before freezing. The measurement of the unfrozen water content for all the samples were implemented by calorimetric method, where the variation of the water content (therefore, the unfrozen water content) was achieved only by varying the initial moulding water content. Accordingly, the variation of the initial moulding water content (or the original water content) results in the variation of the unfrozen water content at different temperatures below zero. Also, unfrozen water content varies at a certain temperature below zero depending upon whether the sample has been frozen directly to the test temperature or first frozen to a lower temperature and then allowed to thaw to the test temperature. The upper limits represent the unfrozen water content measured as the clay or silt samples were frozen directly to the test temperature, while the lower limits represent the measured unfrozen water content as the sample thawed to the test temperature from about 2°C below the test temperature. In addition, the unfrozen water content depends on whether the sample (initially) at unfrozen state was prepared at above optimum, optimum, or below optimum water contents.

For the unconfined compression tests, two different loading rates of 60 psi/min (=6.895 kPa/sec as the slow rate) and 500 psi/min (=57.456 kPa/sec as the fast rate)

were considered. The compressive stress-axial strain curves were obtained from the tests. According to the results, all the frozen soil samples develop higher shear strength at lower temperatures, and (for ring shear tests) under higher axial confining pressures. Yong (1962) also concluded that the developed shear strength comprised of both the cohesion and the friction components, without getting any influence from the shear strength characteristics of the (initial) unfrozen state of the soil under investigation.

Sayles (1974) conducted a series of constant strain rate and constant stress (creep) triaxial compression tests on saturated frozen Ottawa sand in order to study the effect of confining pressure and rate of loading on the strength and deformation characteristics of frozen sand. The frozen soil test samples were cylindrical with 70 mm of diameter and 152.5 mm of length. Ottawa sand specimens, with an average dry unit weight of 1670 kg/m³, a void ratio of about 0.59, and the soil particles specific gravity of 2.65, were all saturated with distilled de-aired water. Samples were frozen from the top down within a period of four days, with access to free water at the bottom. Test temperature for all the samples and loading conditions was $T = -3.85$ °C. Some of the results reported by Sayles (1974) are presented here:

In Figure 2.3, deviator stress-axial strain curves for frozen Ottawa sand and ice, at different confining pressures and under a fixed applied strain rate of 0.03/min (=5E-4/sec) are shown. As clear from the figure, under confining pressures higher than 2.7 MPa, there are two peak stresses on the stress-strain curves. It is suggested that the first peak is the consequence of the strength of the pore ice matrix, while the second peak is mainly the result of the development of friction resistance between soil grains and/or ice crystals as the strain progresses. For lower confining pressures, on the other hand, there is no obvious second peak stress, and the frictional resistance is suggested to be considered as an apparent constant residual strength at each confining pressure. The Mohr circles and Mohr envelopes corresponding to the stress-strain curves of Figure 2.3 are presented in the Figure 2.4, emphasizing the concept that each peak

stress on the stress-strain curves represents one dominant component of strength, i.e. either cohesion or friction.

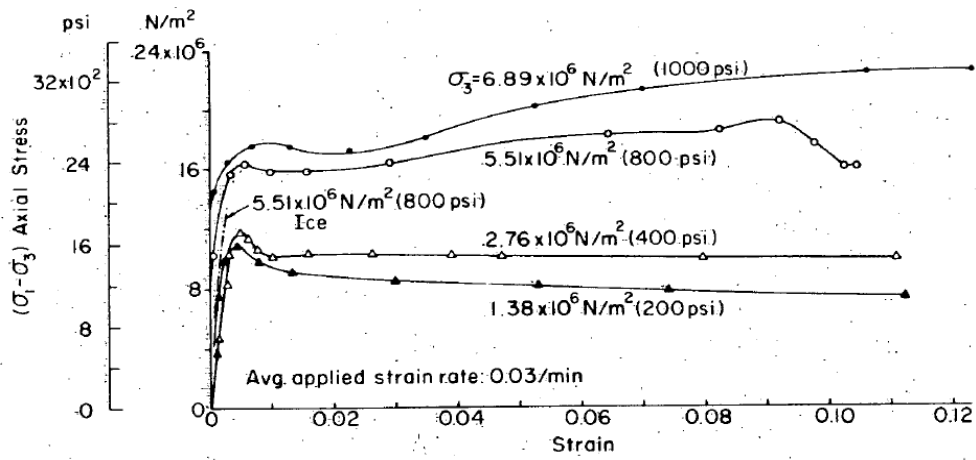


Figure 2.3. Axial stress-strain curves for frozen Ottawa sand and ice at large strains (Sayles 1974).

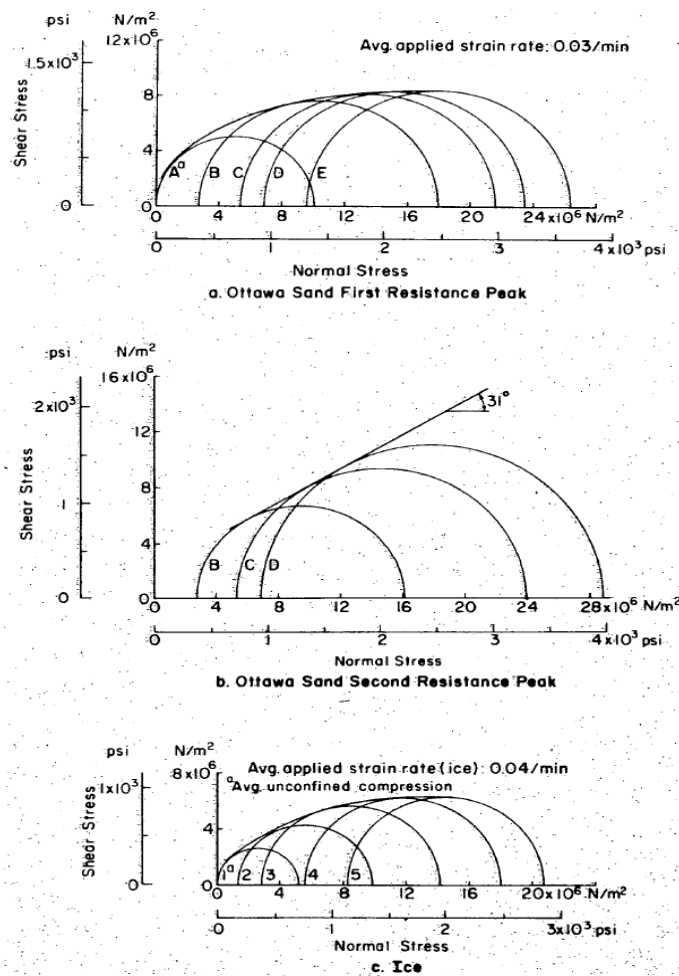


Figure 2.4. Mohr circles and Mohr envelopes for frozen Ottawa sand and ice. A-E and 1-5 on curves indicate different specimens of sands and ice (Sayles 1974).

According to the results by Sayles (1974), the general trend was that the strength increased as the axial strain rate increased.

Haynes and Karalius (1977) conducted a series of uniaxial unconfined compression tests, on frozen Fairbanks silt samples, to investigate the temperature effect (ranging from 0°C to -56.7°C) on the strength. The silt used for this study was classified as ML, i.e. a fine-grained low-plasticity silt, with the specific gravity of $G_s = 2.71$. In order to prepare the frozen samples, initially, the soil was compacted in its air-dried state, with only 1.5% moisture content by weight. The final samples were prepared with 1.43 g/cm³ dry density, void ratio of 0.9, and 29% moisture content after saturation and freezing. When preparing the samples, fast saturation was avoided for a few reasons such as to avoid the incomplete pore air evacuation. Samples were frozen from the top down, and, during freezing, water was supplied at the bottom of the samples. Because temperature was a very important factor in this study, a sufficient time was given to samples to reach an equilibrium with the desired testing temperature (about 1 to 1.5 hours). At a wide range of below zero temperatures, two loading machine speeds of 0.0423 cm/sec (slow rate) and 4.23 cm/sec (fast rate) were used for the uniaxial tests. The machine speeds of 0.0423 cm/sec and 4.23 cm/sec are approximately equivalent to the axial strain rates of 4E-3 /sec and 4E-1 /sec respectively, which are normally classified as high strain rates. According to the results, the compressive strength of frozen Fairbanks silt samples increased about one order of magnitude as the test temperatures decreased from 0°C to -56.7°C. The compressive strength values seemed to be larger than the ones reported by other researchers, which was attributed to the relatively stiff testing machine, i.e. MTS closed-loop electrohydraulic testing machine used by Haynes and Karalius (1977). Furthermore, the initial tangent modulus increased about one order of magnitude with lowering the test temperatures, which was in good agreement with results obtained by others.

In a study by *Parameswaran (1980)*, uniaxial unconfined compression tests were conducted on frozen saturated Ottawa sand samples, at a temperature range of -

2°C to -15°C, and under a wide range of strain rates. The cylindrical samples of frozen sand with a diameter of 50.8 mm and a length of 140 mm were prepared in a split plexiglass mould. Initially, the sand samples were compacted at optimum water content while being connected to a vacuum pump to remove the pore air. Then, the samples were saturated with de-aired distilled water. Next, the specimens were frozen uniaxially from the top down. After freezing, the ends of the samples were trimmed, so the finished cylindrical samples had a length of 127 mm. Also, the total moisture content of the samples was about 20% by weight of soil grains. Uniaxial compression tests under constant strain rates varying between 1E-7 /sec (very low strain rate) and 1E-2 /sec (very high strain rate) were performed at temperatures of -2, -6, -10, and -15 °C. The results illustrated that the compressive strength (maximum stress observed on the stress-strain curve) increased with increasing the strain rate and decreasing the temperature. Also, the initial tangent modulus, E_i , increased with increasing the strain rate. Parameswaran (1980) concluded that lower values of tangent modulus and compressive strength at -2°C, as compared with those at lower temperatures, could be attributed to larger amounts of unfrozen water content existing within the frozen soil sample at -2°C.

In the study by *Bragg and Andersland (1981)*, the effects of various constant strain rates, temperatures, and sample sizes on compressive and tensile properties of frozen silica sand were investigated using uniaxial compression and split cylinder tests. Wedron silica sand with uniform gradation was used for this study. All samples were prepared in split aluminium molds with a sand volume fraction of 64% (“normally encountered in the field” according to the authors) to ensure the development of dilatancy and interparticle friction during sample shearing/deformation. All samples were frozen and stored at -15 °C. The final test specimens had sand fractions in the range of 63.1 to 64.9%, and ice saturation of 96.1 to 99.9%. Focusing more on the compression tests performed, uniaxial compression tests were conducted on cylindrical samples with diameters $D = 287, 357, 493,$ and 611 mm and a 2:1 height-to-diameter ratio (to study the sample size effects), at

temperatures $T = -2, -6, -10, \text{ and } -15 \text{ }^\circ\text{C}$ (to study the temperature effect), under the strain rates of $\dot{\epsilon} = 5.69\text{E-}7$ to $1.78\text{E-}3$ /sec (to study the effect of different strain rates). Based on the results obtained/reported by Bragg and Andersland (1981), the deformation behavior of frozen silica sand changes from plastic brittle failure with increasing strain rates. At low strain rates, i.e. less than $1\text{E-}5$ /sec, the frozen sand deformed elastically in the early stages, followed by an initial yield. Under low strain rates, sufficient time would be available for the pore water to migrate to regions with lower stress levels where refreezing would occur, which is accompanied by the densification of soil particles. Under higher strain rates, i.e. moderate strain rates of $1\text{E-}5$ to $4\text{E-}4$ /sec, the strength of ice matrix increases resulting in a higher initial yield stress. Under high strain rates, i.e. above $4\text{E-}4$ /sec, samples showed multiple slip lines. The yielding of pore ice occurred at the same time of internal friction being developed, without enough time for ice melting, flow, and refreezing to happen. In Figures 2.5 and 2.6, the variation of compressive strength and initial tangent modulus with temperature under different constant strain rates are represented, clearly confirming that both of these mechanical parameters increase with decreasing temperature under each constant strain rate.

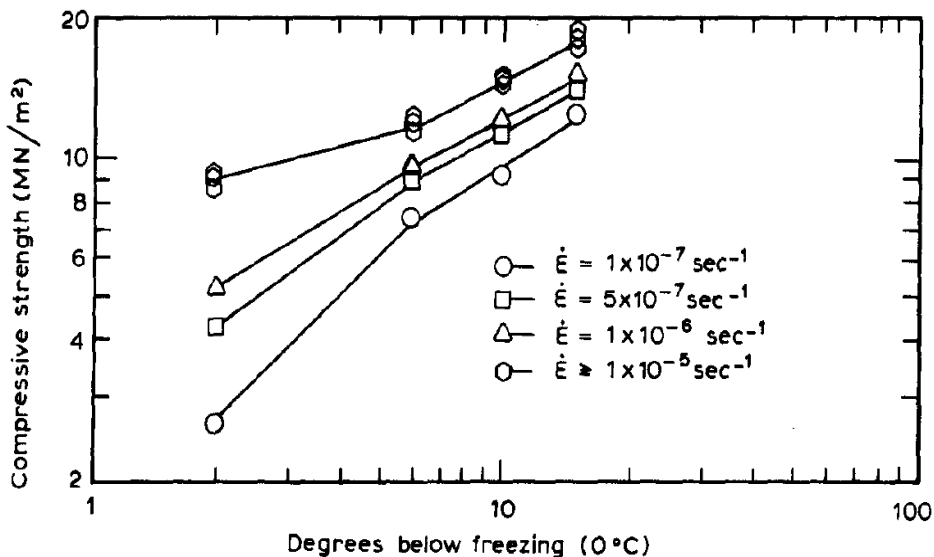


Figure 2.5. Log-log scale plot of compressive strength vs. below zero temperature, under different strain rates (Bragg and Andersland 1981).

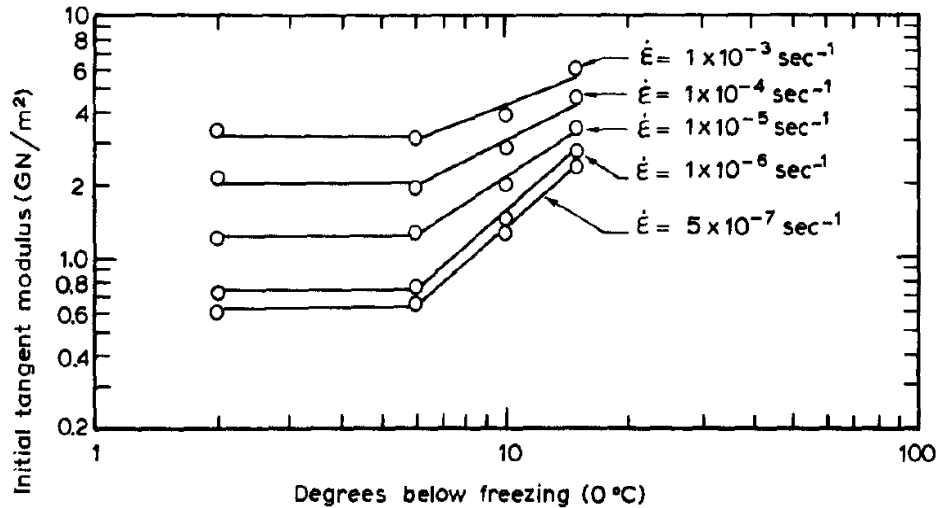


Figure 2.6. Log-log scale plot of initial tangent modulus E_i vs. below zero temperature, under different strain rates (Bragg and Andersland 1981).

In addition, the influence of sample size (diameter) on compressive strength and initial tangent modulus was investigated by Bragg and Andersland (1981). It was proposed that smaller samples were more suitable for the field work, provided sample diameter be 4 or 5 times greater than the maximum particle size within the sample.

In another study, by *Wijeweera and Joshi (1990)*, uniaxial unconfined compression tests were conducted on saturated fine-grained frozen soils, at temperatures between -5 and -17 °C, and under the constant strain rate of $1\text{E-}2/\text{sec}$ (in the high range of strain rates). The purpose of this study was to investigate the effect of dry unit weight, total water content, temperature, and soil type on the compressive strength of frozen fine-grained soils. Six different fine-grained soils Kaolin, Ball clay, Engineering complex, Bentonite-kaolin, Bentonite-silt, and silt-kaolin classified as CL, CH, CL, CH, CH, and CL respectively were used in this study. The saturated soil samples were frozen unidirectionally from top to bottom, with the sample's top being exposed to a temperature of -73 °C and the sides and bottom were insulated. Therefore, the samples were frozen quickly without any access to open water at the bottom, which eliminated the formation of ice lenses within the samples and resulted in massive textured frozen soil specimens. The constant strain rate uniaxial compression tests were performed using a closed loop control material test system (MTS) machine. The rapid loading condition (by applying high axial strain rate) was

considered in order to evaluate the instantaneous settlement and strength of frozen fine-grained soils, minimizing the influence of creep phenomenon on the strength and deformation behavior of frozen soil samples. The specimens were tested under axial compression until an axial strain of 20% was reached. This limited the time duration for each test to about 20 seconds. The average total water content of the tested samples varied between 15% to 105%, and the dry unit weights ranged from 6.5 to 18.5 kN/m³. Usually three samples were prepared and tested under the same conditions (i.e. temperature, water content, etc.). The failure strength or the peak compressive strength was considered to be the maximum stress developed during the test. If the stress was continuously increasing with strain, the peak strength was taken as the stress corresponding to 20% axial strain. The failure strain was taken as the strain at failure stress, and the point where the initial slope of stress-strain curve started to decrease was considered to be the yield point. The yield strains derived from the test results were close to or less than 1%, similar to the failure strains of polycrystalline ice, indicating the fact that yielding of frozen soil would be heavily attributed to the initial failure of pore ice matrix. According to the test results, the peak compressive strength increased with decreasing temperature. Also, at dry unit weights below 11 kN/m³, the peak compressive strength increased rapidly with decreasing the dry unit weight. At dry unit weights between 11 and 17 kN/m³, the variation of peak compressive strength with changes in dry unit weights was small, and finally, at high dry unit weights, i.e. above 17 kN/m³, the peak compressive strength increased sharply with increasing the dry unit weight. Based on the comparison of compressive strengths for all the tested frozen fine-grained soils at similar dry unit weights, the presence of silt and fine-sand particles in the sample increased the compressive strength of frozen clay soils. On the other hand, clay soils with larger specific surface area (=higher plasticity) would have lower ice matrix strength, due to a higher unfrozen water content, and therefore a lower compressive strength. As for the variation of compressive strength with total water content at various temperatures, at very high water contents (above 50%), the peak compressive strength increased with increasing the water content. However, at low water contents

(below 20%), the peak strength increased with decreasing the water content. And finally, at water contents between 20% and 50%, the variation in peak compressive strength with total water content was relatively small. It was also observed that the yield stress increased with increasing the total water content and decreasing temperature, which further provided evidence that the yield stress of a frozen soil would be directly related to ice-matrix strength.

2.3 Studies on frozen soil/rock slope stability

There are a number of studies, available in the literature, focusing on the field and/or numerical investigation of frozen soils and rocks.

Washburn (1947) reported a landslide at De Salis Bay, Victoria Island in the Canadian Arctic, which occurred through the frozen ground adjacent to a lake. It is possible that the reported landslide was because of thermal erosion.

In a study by *McRoberts and Morgenstern (1974)*, a field investigation of the landslides in the Mackenzie Valley N.W.T. is conducted. These landslides, being classified as block and multiple retrogressive (MR) slides, are associated with the shear failure of the frozen soil. The landslides are seated in frozen gravel, sand, and silt overlying partially frozen or unfrozen silty clay. The shear displacement is known to have occurred through the frozen ground while the base of the slide is within the unfrozen clay layer. The frozen condition of the sliding blocks and the MR slides is discussed based on the vegetation patterns on or close to the sliding areas. In Figure 2.7, a schematic representation of permafrost next to the Mackenzie River is shown. MASST, in the figure, is the mean annual soil surface temperature, which is determined by the extrapolation of in situ temperatures below the level of zero annual change. Values of -2.3 to -2.5 °C are reported for MASST. The sliding block and MR slides extend backwards to 150 – 210 m behind the tree line in Figure 2.7. Therefore, any slip surface extending back beyond the tree line would most likely pass through the frozen and into the unfrozen soil.

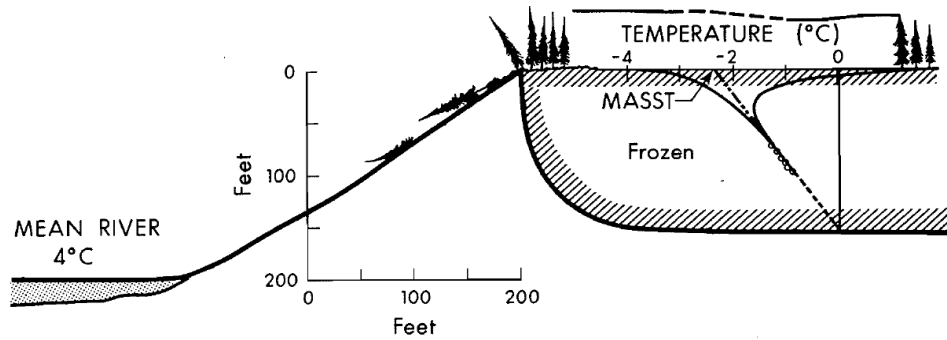


Figure 2.7. Schematic representation of permafrost distribution in a high river bank adjacent to the Mackenzie River (McRoberts and Morgenstern 1974).

In addition, an analysis of the slides in the Mountain River site was performed. These landslides were characterized as block and multiple retrogressive (MR) slides, where shear failure occurred through the frozen soil with the base of slide being seated in the unfrozen clay. The high pore pressure existing in the unfrozen clay played a very significant role in the corresponding shear strength. Several samples were obtained at different depths for performing shear tests on frozen soils representative of the site under consideration (i.e. Mountain River). Uniaxial unconfined constant strain rate tests were conducted on undisturbed frozen samples, at $-1.0\text{ }^{\circ}\text{C}$. For the stability analysis of the frozen soil slope at the Mountain River site, according to aerial photographs and topographic maps, a cross section was considered (shown in Fig. 2.8), where the pre-failure profile was determined based on different field and on-map measurements. For the slope stability analysis the non-circular method was employed. As the first approach, cohesive strength was assigned to the frozen soil. Different levels of pore pressure in the thawed soil underneath the frozen ground were considered. Another approach for the frozen slope stability analysis was based on the assumption that the long-term strength of an ice poor (also called structured) frozen soil, such as most of the permafrost at the Mountain River site, is frictional. For the analysis, the circular arc shown in Figure 2.8 was considered as the average failure surface. For different levels of pore pressure, the mobilized friction angle in the frozen soil was determined so that the factor of safety $F_s = 1$. The second approach was favored.

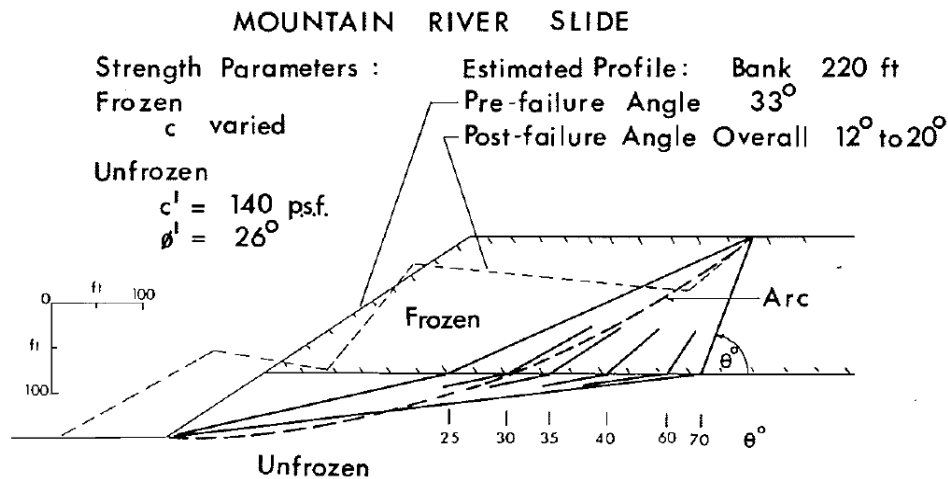


Figure 2.8. The cross section at the Mountain River slide used in stability calculation (McRoberts and Morgenstern 1974).

In another study, by *Mageau and Rooney (1984)*, a field investigation was undertaken to evaluate the effect of different surface treatments on the performance of ice rich frozen cut slopes. Their test site was located near Hess Creek, Alaska. In Figure 2.9, an idealized ice rich frozen cut slope and its stability conditions after the first thaw season (also known as the short-term stability) and the fifth or sixth thaw season (or the long-term stability) are depicted. They mention that different types of frozen cut slope instability/failure differ primarily from one another in the volume of frozen soil displaced, the physical form of failure, and the rate of frozen soil movement. Also, frozen slope failures such as Sloughing and Flow generally occur during the thawing process, while for the Planar slide and Rotational slide to occur, thaw penetration needs to reach to a depth where the shear strength of the supporting soil cannot take the weight of the above thawed mass anymore.

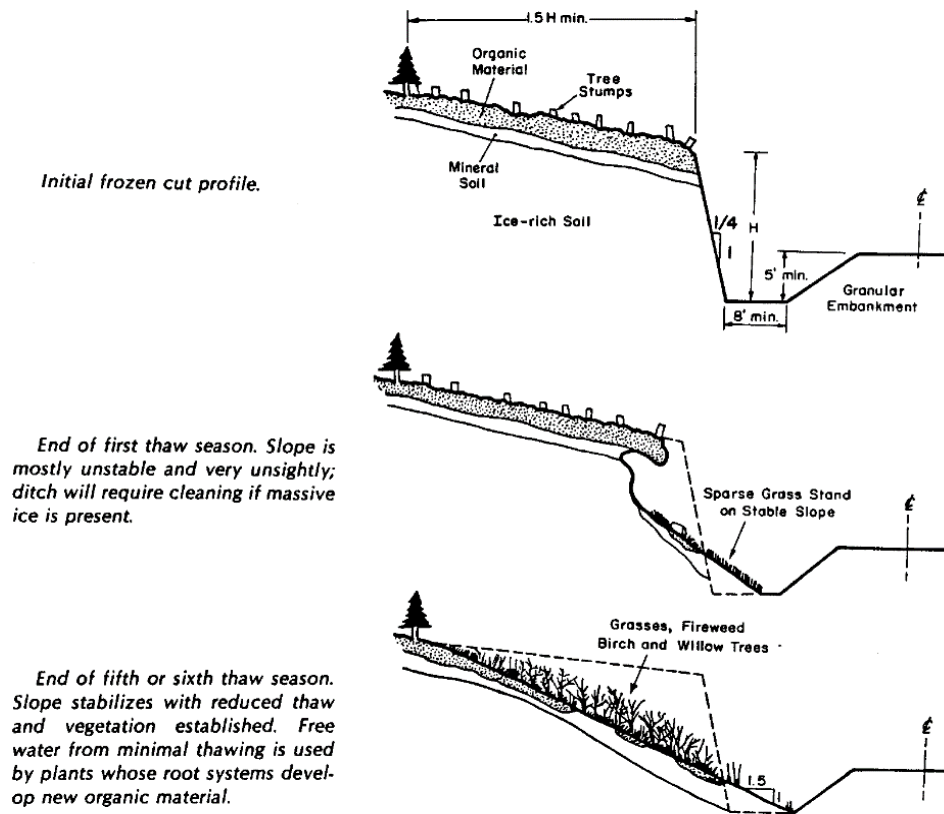


Figure 2.9. Idealized stability development in ice rich frozen cut slopes (Mageau and Rooney 1984).

According to their results, surface treatments with higher insulation properties (e.g. foam insulation) were more successful in reducing the thermal erosion in frozen cut slopes. Low thaw penetration depths resulted in less sloughing towards downslope. In addition, the long-term stability of frozen cut slopes was related to both the initial ice content of the frozen soil and the shear strength of the thawing soil.

Niu et al. (2005) conducted a study of thaw slumping which occurred on two permafrost slopes in Qinghai-Tibet Plateau. Thaw slumping mostly occurs on very gentle (i.e. low gradient) slopes. This type of failure was not a one-time event, and it developed year after year, through cycles of freezing, thawing, collapse and slide. The results obtained by *Niu et al. (2005)* confirmed that the failure modes involved were mainly collapse and slide of the active layer along the ground ice surface, known to be a type of slope failure related to the ice-rich frozen soil slopes. Also, in their stability analysis and estimating method, they considered the seepage of water from ice-melting of the frozen ground.

In a study by *Su et al. (2006)*, a field investigation of a newly developed small landslide next to an existing large one, located in the Travaillant Lake area near the Mackenzie valley in Northwest Territories of Canada, was conducted in the late summer of 2005. Slope stability studies were done with the aim of performing a back analysis of the already occurred slope failures. In this regard, test pits were excavated in the area, and geotechnical tests were conducted on soil samples. Also, field vane shear tests were carried out on the permafrost active layer in order to characterize the shear strength of permafrost slope materials. It was noted that permafrost in this region extended to a depth of more than 100m, where landslides were commonly observed especially in areas burned by wild fire. Many of these landslides were located around lakes and on the side slopes along creeks, and they had a circular plan view with usually one hundred to several hundreds of meters in diameter. The investigations started from smaller scale failures, where the initial failures exposed ice-rich permafrost in the head scarps, leading to continued retrogressive failures along the scarps (Su et al. 2006). Most landslides of this type remain active for years, and it would take decades before the slope stabilizes. In Figure 2.10, the location of study area and a photograph of the specific landslide under investigation are shown. The region of the observed landslide was covered with ground moraine (till) underlying other surficial sediments. In this area, the till consisted mostly of silt and clay, and the fine-grained sediments had 10 to 25% of segregated ice. According to the test pits near both new and existing landslides and the laboratory results of soil samples, the mineral soils at the site were mostly grey clayey silts and the volumetric ice content of the permafrost layer could reach 90%. As a result of the heavy burning incident in 1998, an almost complete loss of vegetation cover occurred in the study area. The depth of the permafrost active layer was measured in both unburned and burned areas, indicating that the depth was thicker in the burned area (about 1.2–1.5m). This was attributed to the reduction or elimination of the shielding vegetation cover and the organic mat.

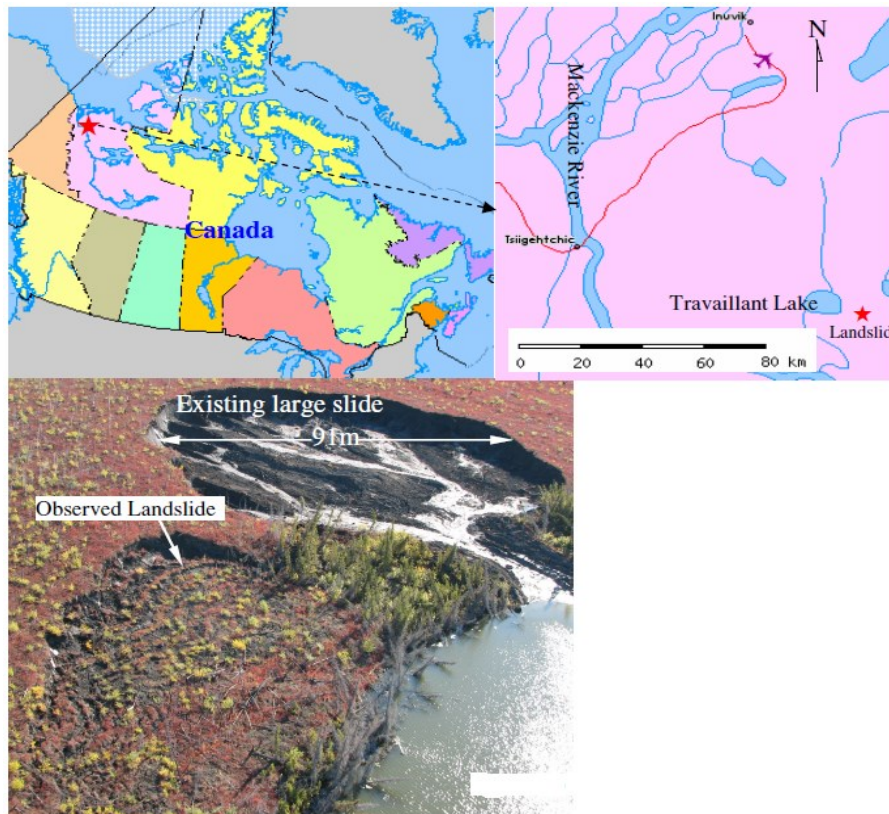


Figure 2.10. Location of study area and the observed landslide under investigation (Su et al. 2006).

Based on the results from laboratory tests on soil samples collected from the test pits near the new and existing landslides, the moisture content in the active layer increased with depth and the ice (water) content in the permafrost layer was very high, reaching about 200%. In addition, from the wet sieving and particle size analysis, the grain size distribution of the active layer material was determined, indicating that the material was clayey silt. Vane shear tests were conducted on the active layer soil using a handheld portable vane shear device to measure the in situ shear strength. The results illustrated that the undrained shear strength of the active layer decreased with depth, which was attributed to the increased moisture content. In Figure 2.11, the variation of the normalized shear strength (both peak and residual) with depth of the active layer is presented.

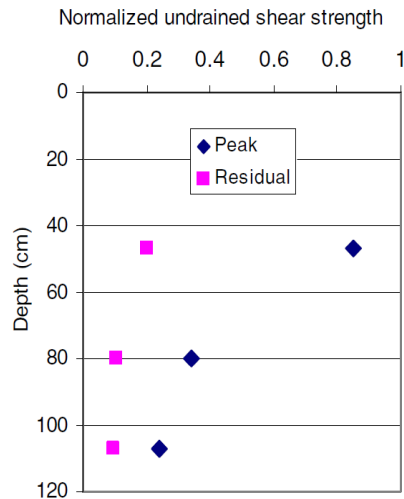


Figure 2.11. Undrained shear strength of the active layer normalized by the overburden pressure (Su et al. 2006).

Furthermore, slope stability back analysis was performed for the above-mentioned newly developed landslide considering the field observations and laboratory measurements. Su et al. (2006) used the Slope/W software (Geo-Slope International, 2005) to define a limit equilibrium model and implement the stability analysis regarding the initial failure of the slope. The model is shown in the figure below.

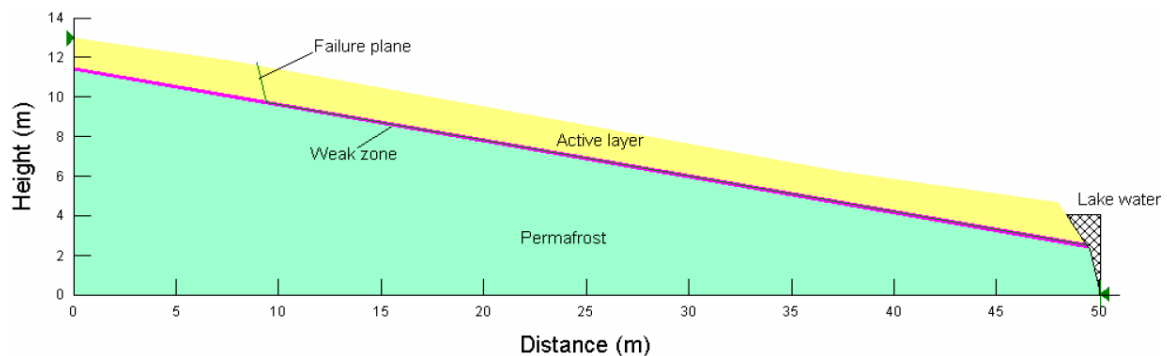


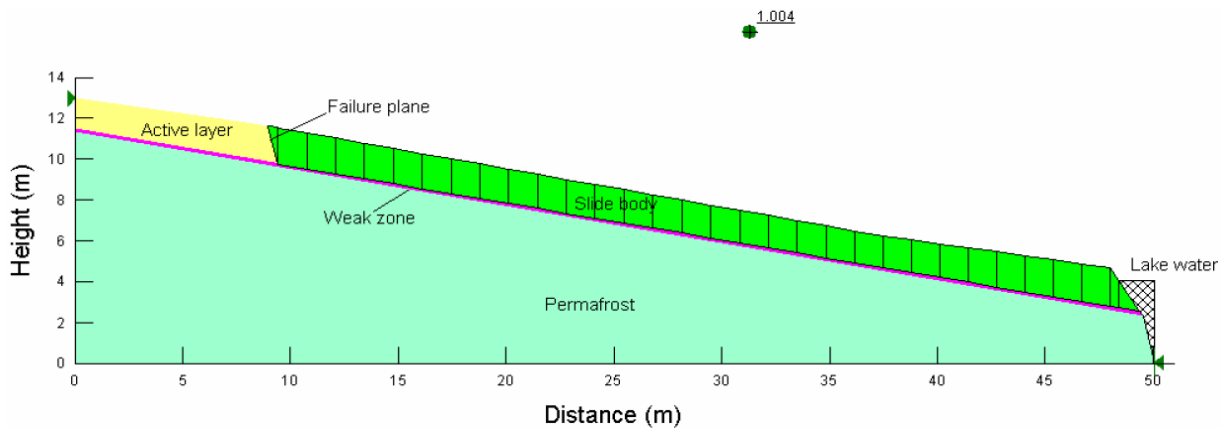
Figure 2.12. Slope/W analysis model for the initial slope instability of the observed landslide (Su et al. 2006).

The thickness of the active layer shown in Figure 2.12 is set to be 1.5m, which is underlain by a thin weak layer being defined as the slip surface for the model. Underneath the weak zone, there exists a thick layer of ice-rich permafrost. It was argued by Su et al. (2006) that thawing of the fine-grained ice-rich permafrost could result in an increase of moisture content throughout the overlying active layer, leading

to the reduction of shear strength. Sliding (=initial slope failure) would occur under undrained conditions through the weak layer (at the bottom of the active layer). The undrained shear strength parameters (obtained from the field vane shear tests) defined in the model, and the stability analysis results based on those parameters are presented in Figure 2.13. In addition to the strength parameters for the active layer and the weak zone (Fig. 2.13a), significantly high strength values were considered for the permafrost layer. According to Figure 2.13b, sliding occurs on the weak layer and the slope is in a critical condition (factor of safety against sliding = 1.004, really close to 1.0).

Material	Unit weight (kN/m ³)	Undrained shear strength C_u (kPa)
Active layer	19	6.4
Weak zone	17	4.9

(a)



(b)

Figure 2.13. Stability analysis parameters and results: (a) Undrained shear strength parameters, (b) Slope stability results (Su et al. 2006).

A few important notes were pointed out by Su et al. (2006):

- Where the thawing rate of the permafrost soil is rapid compared to the consolidation rate of the thawed soil, and the shear strength of the soil is low, translational sliding occurs under approximately undrained conditions. The already started sliding failure continues to expand with further retrogressive failure.

- Release of pore water from the thawed permafrost layer, results in an increase of moisture content in overlying active layer, leading to the decrease of shear strength.
- The portable field vane shear test can be useful for the undrained shear strength testing of fine-grained materials.

In the study by *Nater et al. (2008)*, which is also referred to in other sections of this thesis, a guidance was provided in dealing with limit equilibrium analysis of permafrost slope stability, especially for selecting appropriate geotechnical parameters. Their proposed approach was based on the published data and interpretation of laboratory tests on undisturbed samples of alpine permafrost soils presented by Arenson et al. (2004) and Arenson and Springman (2005a, 2005b). It is worth mentioning that these studies focused mostly on ice-rich permafrost/frozen soils. Nater et al. (2008) employed the Mohr-Coulomb (MC) failure criterion to describe the shear resistance of frozen soil material, where the two main parameters obviously included the effective angle of internal friction ϕ' and the cohesion c . They considered the unfrozen water content, hence the volumetric ice content parameter w_i , as a key factor in describing the variation of shear strength parameters with temperature for warm permafrost soils. Also, two reference values were defined, the internal friction angle corresponding to unfrozen condition ($T > 0$ °C) and the cohesion at $T = -2.1$ °C as a function of volumetric ice content at this temperature. Using these reference values, the friction angle and cohesion at negative temperatures and different ice contents would be calculated. This model will be explained and discussed more in depth in the following Chapters 4 and 5. Here, an example application of the model, implemented by Nater et al. (2008), is briefly presented:

A profile from the Muragl rock glacier in Switzerland was modeled using the software Slope/W (from GeoStudio2004). The modeled slope had a length and height of about 500m and 235m respectively. The overall inclination of slope was about 25°, and bedrock could be found at an average depth of 33m. Two measured temperature profiles were applied in this analysis, one for the summer and the other one for the winter seasons (shown in the figure below).

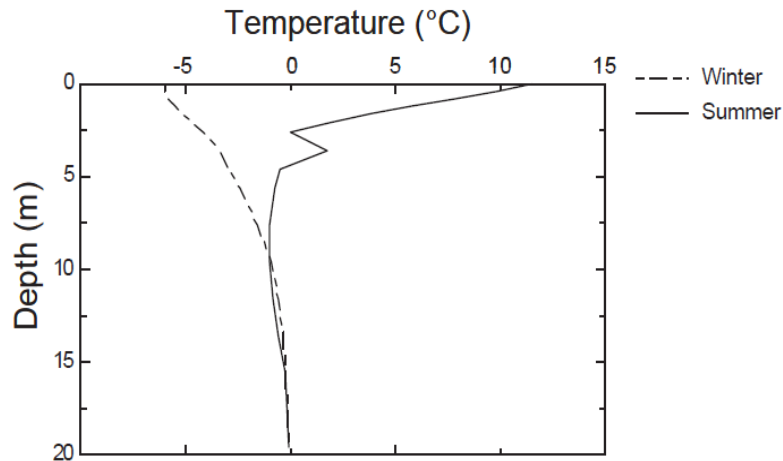


Figure 2.14. Temperature profiles from borehole measurement on the Muragl rock glacier (Nater et al. 2008).

The geotechnical parameters were determined according to the above-mentioned proposed approach, considering the temperature profiles shown in Figure 2.14. The initial effective internal friction angle was assumed to be $\phi' = 33^\circ$ (for the unfrozen condition). The limit equilibrium method of Morgenstern-Price was employed, with no water flow or unsaturated strength being accounted for in the unfrozen active layer. The results for the failure mechanisms are presented in Figure 2.15. According to the results, factor of safety increased from summer to winter by 21% (i.e. from 1.22 to 1.48). The critical mechanisms showed significant differences in size and depth (Fig. 2.15a and 2.15b). It was explained that an increase in the frictional component of shear strength (during the summer) would cause the failure mechanism to shift towards the surface. On the other hand, an increase in cohesion (during the winter, because of the higher volumetric ice content and ice cementation) would result in a deeper lying failure surface. Moreover, creep mechanism was not directly considered in the stability analyses, but it was argued by Nater et al. (2008) that “since the shear strength parameters were chosen as large strain parameters, large creep deformations were included to a certain extent”. It was also pointed out that the major problem with their proposed approach for warm frozen slopes was the lack of test data (only a few data were available for temperate coarse-grained permafrost soils). Therefore, proper geotechnical (lab) tests should be conducted for accurate frozen soil characterizations.

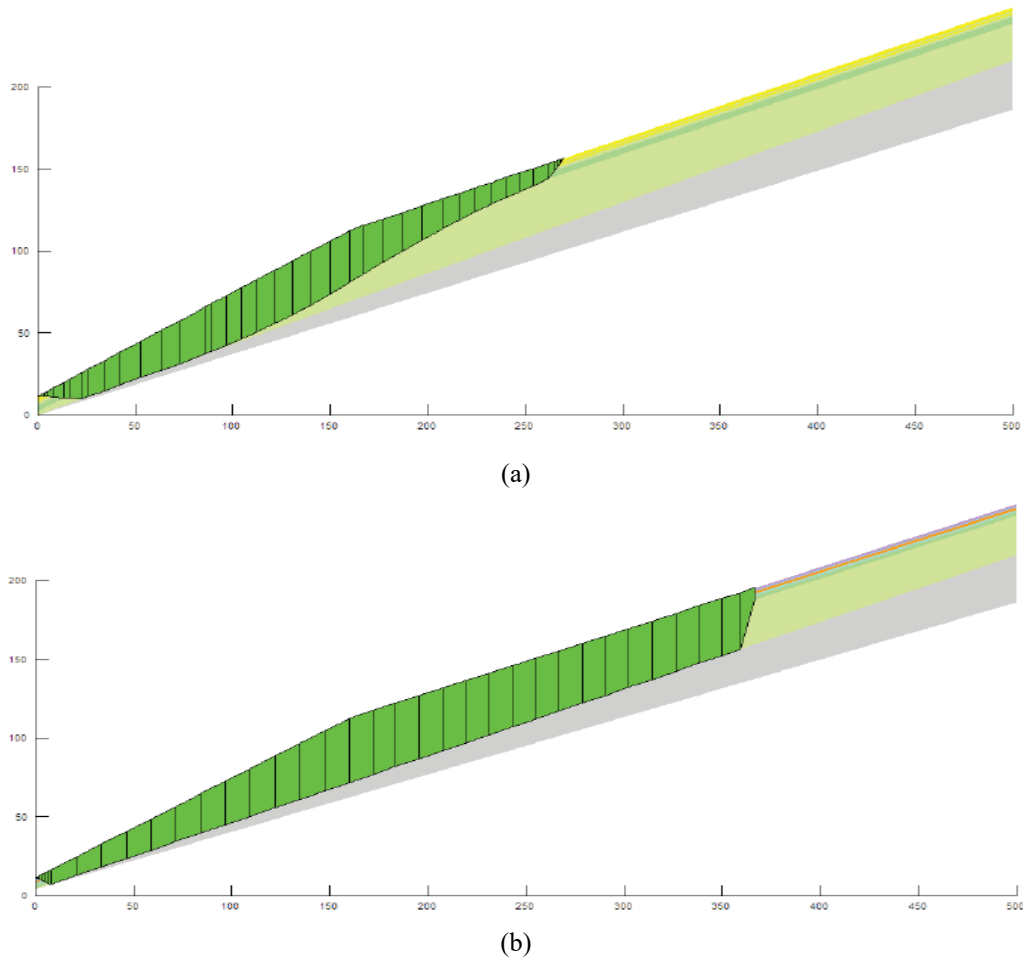


Figure 2.15. Failure mechanisms for the (a) summer temperature profile with a global factor of safety $FOS = 1.22$ and (b) winter temperature profile with a global factor of safety $FOS = 1.48$. Numbers on the x and y axes are in meters (Nater et al. 2008).

In a study by *Li et al. (2015a)*, the seismic characteristics of a railway embankment on a sloping ground in permafrost regions of Qinghai-Tibet Plateau (QTP) were monitored and simulated. For this purpose, a coupled water-heat-dynamics model was developed based on the theories of heat transfer, soil moisture dynamics, frozen soil mechanics, soil dynamics, etc. The numerical results showed that seismic acceleration, velocity, and displacement responses were significantly different in four typical seasons. From the top down, the sloping ground consisted of different layers/materials namely ballast, fill, sandy soil, and weathered mudstone. It was pointed out that in a freezing-thawing soil, ice aggregation might actually block the water migration paths, therefore, the respective hydraulic conductivity and diffusivity would become smaller than those in unfrozen soil medium. Seismic

responses were analyzed on four different dates throughout the year, January 15, April 15, July 15, and October 15, representing four different temperature modes. Because of the difference in ambient air temperature, the unfrozen water content and ice distribution of the embankment varied greatly from one analysis time to the other. As a result, the mechanical properties were very different from one season to the other. According to the obtained results, the residual horizontal displacement responses of the embankment after the earthquake were obvious when thaw penetration reached its maximum in the active layer on October 15, and the maximum horizontal displacement was obtained to be -10.9 cm. The peak of excess pore water pressure was the largest when the thaw depth had its maximum on October 15, however, it was far less than the initial effective vertical stress. Therefore, the embankment did not experience liquefaction under the applied seismic loading. It was argued that the numerical model needed a more complete field monitoring of the unfrozen water and ice content variations to further support the theoretical approach. Also, the classic definition of effective stress, i.e. the effective stress being defined as the total stress minus the pore pressure in an unfrozen soil, was extended to the frozen soil medium. More tests on pore pressure measurement were needed in order to verify whether the effective stress definition could be applied to the frozen or partially frozen soils. In addition, the Mohr-Coulomb criterion incorporated in their modeling, could not appropriately describe the complex dynamic behavior of frozen soil medium. As a result, the dynamic stress-strain modeling required further study.

Siva Subramanian et al. (2017) developed a stability assessment approach for the soil slopes in seasonal cold regions. Their method was capable of considering the water content changes of soil due to the seasonal climatic effects such as freeze-thaw action, snowmelt water infiltration, etc. and incorporate them into the respective slope stability analysis. The proposed approach for simulating the soil water content distribution subjected to freeze-thaw action and snowmelt water infiltration was based on “the two-dimensional plane strain numerical modeling, considering the non-isothermal seepage simulation followed by a slope stability assessment” (Siva Subramanian et al. 2017). The first part of their proposed stability assessment

approach was to configure the initial equilibrium of the soil slope in terms of soil water content distribution and temperature. The second part was to use the above-mentioned method to estimate the water content distribution of the soil slope subjected to freeze-thaw action and snowmelt water infiltration. The outcome of the soil water content simulation would be the water content distribution inside the soil slope on a day-to-day basis. Then, in the third part, for the slope stability analysis, a traditional limit equilibrium technique based on the method by Morgenstern and Price (1965) was used to determine the factor of safety (FOS), where the unsaturated shear strength of soil was also considered in the calculation process. The whole procedure of numerical analysis was performed using the Vadose/W and Slope/W (from the GeoStudio softwares). Two case studies of slope failure in Hokkaido, Japan, were performed using the proposed approach, accompanied by parametric studies to obtain comprehensive results in view of the slope stability analyses. The first case study was the failure of a trial embankment slope constructed using volcanic soil, and the second one was a slope failure occurred in a man-made embankment along the national highway in Hokkaido, Japan. Back analyses were implemented to investigate the factors causing failure. Using the limit equilibrium method, slope stability assessments were made using the soil water content distribution data obtained from a coupled simulation. Furthermore, to visualize the influencing parameters on slope stability, parametric studies were conducted by considering and neglecting the effects of ground freezing, snowfall, and rainfall.

The numerical model and geometry of the first case study, i.e. the embankment slope constructed by a volcanic soil at an angle of 45° with 5m elevation and 7.7m length at the base is shown in Figure 2.16. Different instruments such as thermometers, tensiometers, moisture content sensors, rainfall and snowfall gauges were installed within the slope to monitor various parameters including the ground temperatures, pore water pressure, soil water content, as well as the rainfall and snowfall. The monitoring continued for about 343 days, until the slope failure occurred.

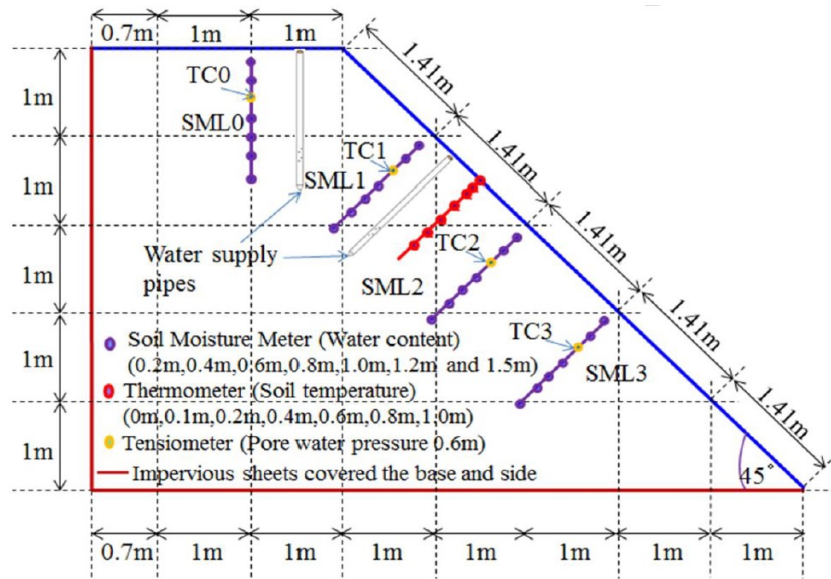


Figure 2.16. Two-dimensional cross section of embankment slope showing installed monitoring instruments (Siva Subramanian et al. 2017).

For the numerical simulation, the results from laboratory element tests (e.g., dry density, hydraulic conductivity, effective cohesion, effective friction angle, etc.) and the data from monitoring the volcanic soil embankment slope (e.g., initial distribution of volumetric water content, temperature, average daily rainfall, average daily wind speed, etc.) were utilized. From the numerical stability analysis, FOS was determined, and the results were compared with measured/monitored data. The analysis results and the measured data were very close.

As for the second case study, i.e. national highway slope failure, the size of the failure was about 44m along the road and 19m in depth. As a result, a large amount of sediments (embankment fill material and accumulated snow) flowed downward to the toe of slope, shown in Figure 2.17. In this case, the cumulative daily rainfall and snowmelt water caused the slope failure. For the numerical simulation, a two-dimensional model was defined using the already collected geological data (shown in Fig. 2.18). The stratigraphy of slope consisted of three different soil/rock types (embankment filling, talus slope material, and the bedrock), and the ground water table was at an average depth of 8m. The properties for the slope material, such as dry density, hydraulic conductivity, and undrained shear strength were obtained from laboratory measurements. For the embankment filling and talus layer, the available

undrained and saturated shear strength data were considered respectively, and the bedrock was modelled as a low permeability material.

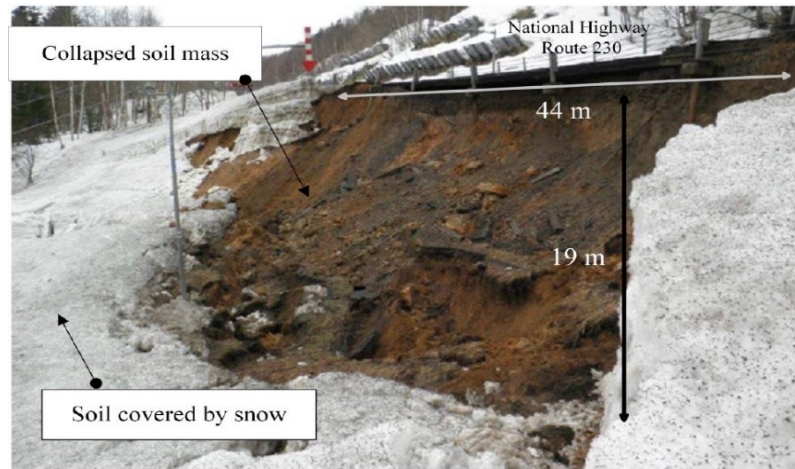


Figure 2.17. Photo of the national highway slope failure (Siva Subramanian et al. 2017).

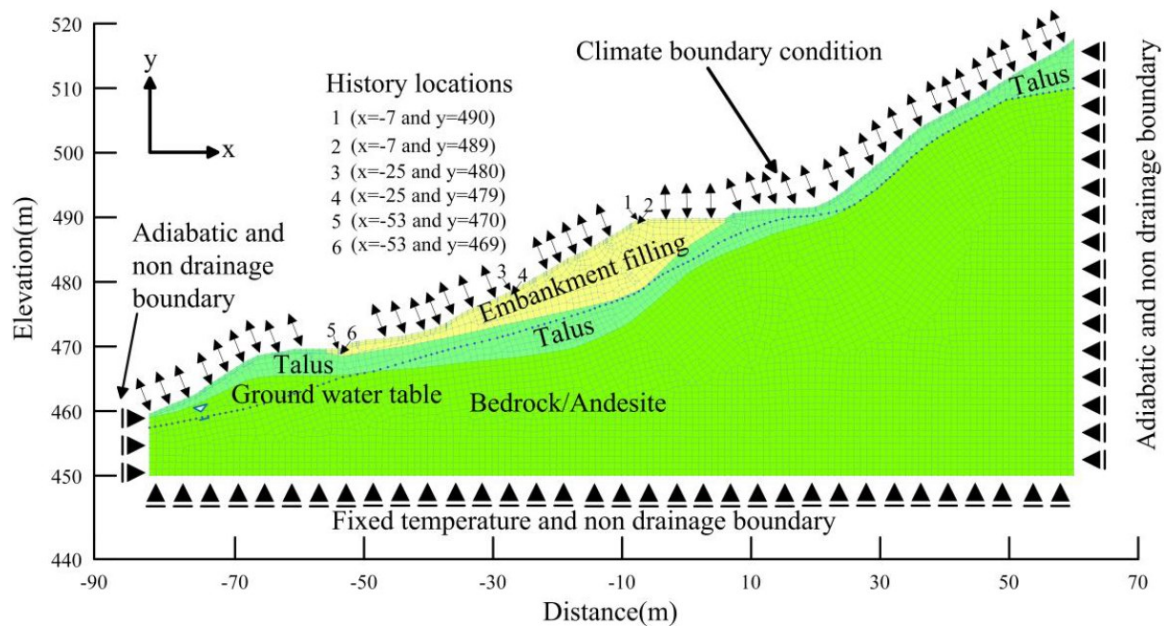


Figure 2.18. Two-dimensional numerical model for highway slope with boundary conditions (Siva Subramanian et al. 2017).

In addition, since for the long-term stability analysis drained shear strength parameters were needed, the effective cohesion and effective friction angle for the embankment filling material were derived using a back calculation method. The ground water table was obtained from the available geological survey, and the climate

data used in the simulation was from the meteorological telemetry located close to the site under investigation. According to the analysis results, on the day of slope failure, the volumetric water content reached the saturated water content and the respective pore pressure reached 0 kPa. A complete comparison of the simulation results with the measured data from the site indicated a close similarity between them.

Furthermore, for the parametric study, some specific factors were magnified or neglected in both above-mentioned numerical analyses to investigate their influences on slope stability more in depth. For example, the amounts of rainfall and snowfall were increased to twice and three-times of the measured data already considered in the numerical simulations. This reduced the stability of slope significantly. In this regard, the increase in accumulated snow depth resulted in an excess amount of snowmelt water, which eventually reduced the slope stability. Moreover, the effect of freeze-thaw action was investigated by performing the simulations with and without this factor. The results demonstrated that, by considering the freeze-thaw action the factor of safety against failure decreases. Therefore, when assessing the slope stability in seasonal cold regions, the effects of freeze-thaw action must be considered in estimating the soil water content distribution. In another effort, the effect of shear strength of frozen soil was studied. The approach proposed by Arenson and Springman (2005a, 2005b) was employed to determine the shear strength parameters. It was concluded that if a large portion of the slope slip surface was occupied by frozen soil, then the frozen shear strength of slope material should be properly considered in the stability assessment of slope. Finally, it was concluded that factors such as freeze-thaw action and snowmelt water infiltration should be properly considered in assessment of slope stability in cold regions.

3 Theoretical basis and methodology

The mechanical behavior of materials such as concrete, rocks, soils, etc. can be described by the theory of plasticity, under a wide range of circumstances in practical applications. According to de Souza Neto et al. (2008), these materials are classified as plastic (or even rate-independent plastic), with principal phenomenological characteristics such as:

- “1- The existence of an elastic domain, i.e. a range of stresses within which the behavior of material is considered as purely elastic, without the evolution of permanent (plastic) strains. The elastic domain is delimited by the yield stress.
- 2- If the material is further loaded at the yield stress, then plastic yielding (or plastic flow), i.e. evolution of plastic strains, occurs.
- 3- Accompanying the evolution of plastic strain, the evolution of the yield stress is also observed. This phenomenon is known as hardening.”

In materials such as soils, experiments including the triaxial shear tests where the soil sample is subject to a confining all-around pressure, before the application of the axial compression, result in stress-strain curves which represent the above-mentioned properties (see Fig. 3.1). In Figure 3.1, the line segments O_0Y_0 and O_1Y_1 define the elastic domain at two different states, with their corresponding yield stresses at Y_0 and Y_1 . The transition between the elastic region and the elastoplastic regime occurs with a non-smooth change of slope (at points Y_0 and Y_1). The path for the plastic yielding is defined by $O_0Y_0Y_1Z_1$, also known as the virgin curve. After the (soil) sample is loaded from the initial state O_0 to the stress level σ_0 , then unloading on the path Y_1O_1 (the linear elastic segment), results in a constant permanent (plastic) strain ε^p , corresponding to the yield stress σ_0 . The slope E of the linear elastic segments denotes the Elastic or Young's modulus of the material, and E^{ep} is called the elastoplastic tangent modulus. It is also worth mentioning that the difference between the total strain and the current plastic strain, $\varepsilon^e = \varepsilon - \varepsilon^p$, is completely reversible because it is inside the linear elastic region (known as the elastic strain).

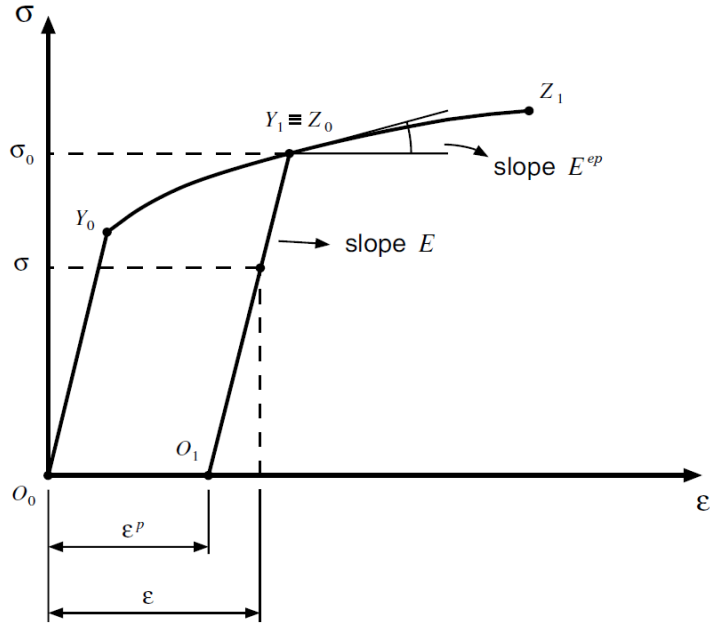


Figure 3.1. Idealized axial stress-strain curve, showing strain hardening (de Souza Neto et al. 2008).

In order to completely define a constitutive behavioral model for the material under consideration, e.g. soil, the aforementioned items 1 and 2 are associated with the formulation of a *yield criterion* and a *plastic flow rule*, and item 3 with the formulation of a *hardening law* (de Souza Neto et al. 2008). To define the yield criterion, a yield function Φ needs to be introduced, which simply considers the current and the yield stress states, $\Phi(\sigma, \sigma_y)$. de Souza Neto et al. (2008) note that at any stage, no stress level is allowed above the current yield stress condition σ_y , meaning that any combination of plastically admissible stresses, σ , lies either within the elastic domain or on its boundary (i.e. the yield limit or the yield surface): $\Phi(\sigma, \sigma_y) \leq 0$. For stress conditions staying within the elastic domain, $\Phi(\sigma, \sigma_y) < 0$, only elastic strains might develop, i.e. plastic strain rate $\dot{\epsilon}^p = 0$, while at yield condition, $\Phi(\sigma, \sigma_y) = 0$, either elastic unloading (i.e. plastic strain rate $\dot{\epsilon}^p = 0$) or plastic yielding/loading (i.e. plastic strain rate $\dot{\epsilon}^p \neq 0$) occurs.

Under plastic loading, plastic straining occurs, i.e. $\dot{\epsilon}^p \neq 0$, where the plastic flow rule is defined in order to determine the plastic strain rate ($\dot{\epsilon}^p$). Within the formulation of plastic flow rule, a parameter called the plastic multiplier, $\dot{\gamma}$, is introduced, which is non-negative ($\dot{\gamma} \geq 0$) and satisfies the complementary condition

$\Phi \dot{\gamma} = 0$ (de Souza Neto et al. 2008). Based on its definition, plastic multiplier vanishes during elastic straining, while it might develop non-negative values during plastic flow/straining.

Finally, to incorporate the hardening law into the constitutive model, within the formulation of the yield function Φ , the yield stress state needs to be defined as a function of the plastic strain, i.e. $\sigma_y = \sigma_y(\varepsilon^p)$. The hardening curve for a one-dimensional model is shown in the Figure below.

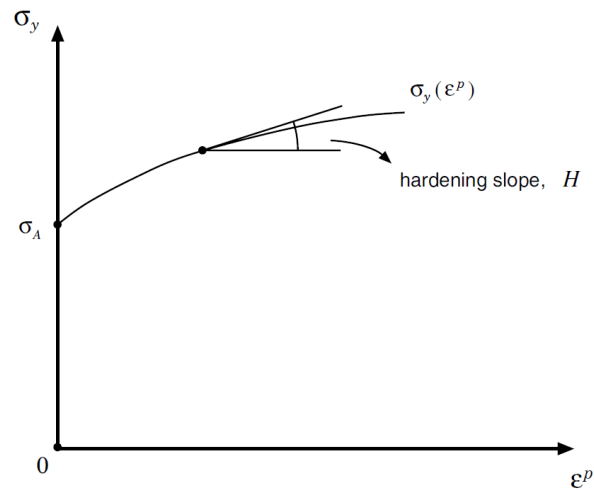


Figure 3.2. Hardening function, also called hardening curve for a one-dimensional model (de Souza Neto et al. 2008).

In multidimensional constitutive models of plasticity, the yield function, $\Phi(\boldsymbol{\sigma}, \mathbf{A})$, considers the stress tensor and a set of \mathbf{A} hardening thermodynamical forces, where the plastic flow may occur only when $\Phi(\boldsymbol{\sigma}, \mathbf{A}) = 0$ (de Souza Neto et al. 2008). In addition, the flow rule, and also the hardening law, might be defined in terms of a flow (or plastic) potential. A general form for the flow potential is $\psi = \psi(\boldsymbol{\sigma}, \mathbf{A})$, from which the flow vector is obtained as $\mathbf{N} = \partial\psi / \partial\boldsymbol{\sigma}$. When the hardening law is derived from the same flow potential function, it would result in $\mathbf{H} = -\partial\psi / \partial\mathbf{A}$. With regard to the material and the problem under consideration, sometimes it is reasonable to assume that the yield and the flow potential functions are the same, i.e. $\Phi = \psi$, which results in an associative (also called associated) plasticity model. Otherwise, in the general case of $\Phi \neq \psi$, it would be referred to as a non-associative model.

So far, the rate-independent plasticity models and their principal aspects are briefly explained. These models are fairly capable of describing the behavioral

characteristics of elastoplastic materials, such as soils and rocks, under many circumstances. However, it should be emphasized that these models are known to be a limit case of a more general and sophisticated constitutive theory named as rate-dependent plasticity (or viscoplasticity). Some advanced mathematical concepts, including the subgradients and subdifferential, are widely incorporated in developing the rate-independent and obviously the more general, i.e. the rate-dependent, constitutive theory of plasticity. Learning these concepts are essential in understanding, in depth, the above-mentioned plasticity theories.

3.1 Classical yield criteria

In this section, some of the most commonly used yield criteria in engineering applications (namely the Tresca, von Mises, Mohr-Coulomb, and Drucker-Prager yield criteria) are presented and briefly explained.

3.1.1 The Tresca yield criterion

This criterion, originally proposed by Tresca (in 1868) for describing plastic yielding in metals, assumes that plastic yielding begins when the maximum shear stress reaches a critical value. The yield function is defined as

$$\Phi(\boldsymbol{\sigma}) = 1/2 (\sigma_{\max} - \sigma_{\min}) - \tau_y(\alpha) \quad (3.1)$$

where, $\boldsymbol{\sigma}$ is the stress tensor. The maximum shear stress is given by $\tau_{\max} = 1/2 (\sigma_{\max} - \sigma_{\min})$, and the τ_y is the shear yield stress, assumed to be a function of a hardening internal variable α . As explained before, the onset of yielding is characterised by $\Phi = 0$. The Tresca yield function can also be presented as

$$\Phi(\boldsymbol{\sigma}) = (\sigma_{\max} - \sigma_{\min}) - \sigma_y(\alpha) \quad (3.2)$$

with σ_y being the uniaxial yield stress, $\sigma_y = 2 \tau_y$. As a matter of fact, when plastic yielding occurs under the uniaxial stress condition, then $\sigma_{\max} = \sigma_y$ and $\sigma_{\min} = 0$.

Because the Tresca yield criterion is basically defined in terms of the shear stress, it is pressure insensitive, i.e. the hydrostatic component of pressure (of the

stress tensor) does not have any effects on the yielding characteristics. This is probably more appropriate when modeling the behavior of materials such as metals, where the effect of hydrostatic stress on yielding is mostly negligible (de Souza Neto et al. 2008). Another important characteristic of the Tresca yield criterion is isotropy. This is because its yield function $\Phi(\boldsymbol{\sigma})$ is defined based on principal stresses, which results in the Tresca yield function being an isotropic function of the stress tensor (de Souza Neto et al. 2008). In the space of principal stresses, the yield surfaces of the (isotropic) Tresca yield criterion are presented in the figure below.

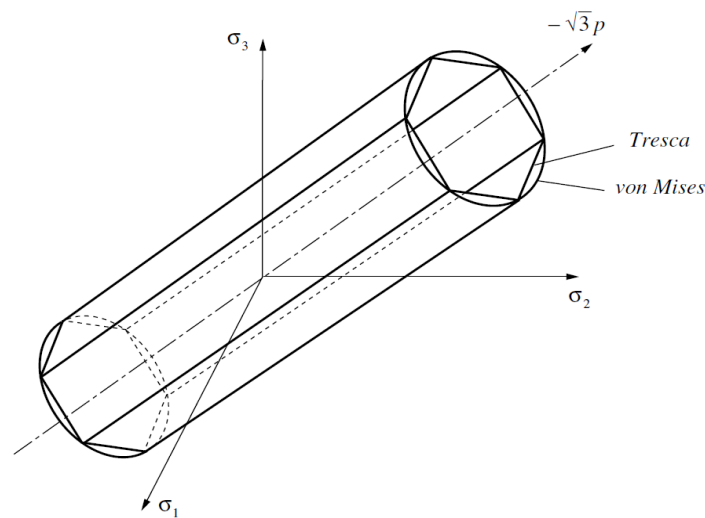


Figure 3.3. The Tresca and von Mises yield surfaces in principal stress space (de Souza Neto et al. 2008).

As clear from Figure 3.3, the Tresca yield surface, i.e. the set of stresses for which $\Phi = 0$, is represented by the surface of an infinite hexagonal prism with its axis coinciding with the hydrostatic line defined by $\sigma_1 = \sigma_2 = \sigma_3$. Clearly, the elastic domain, where $\Phi < 0$, corresponds to the interior space of the prism. As mentioned before, the Tresca criterion is pressure insensitive. As a result, the yield surface can also be represented by its projection on the subspace of stresses with zero hydrostatic pressure component, i.e. $\sigma_1 + \sigma_2 + \sigma_3 = 0$, which is also called the deviatoric plane or the π -plane (de Souza Neto et al. 2008). Both the π -plane itself and the projection of the Tresca yield surface on the π -plane are shown in Figure 3.4.

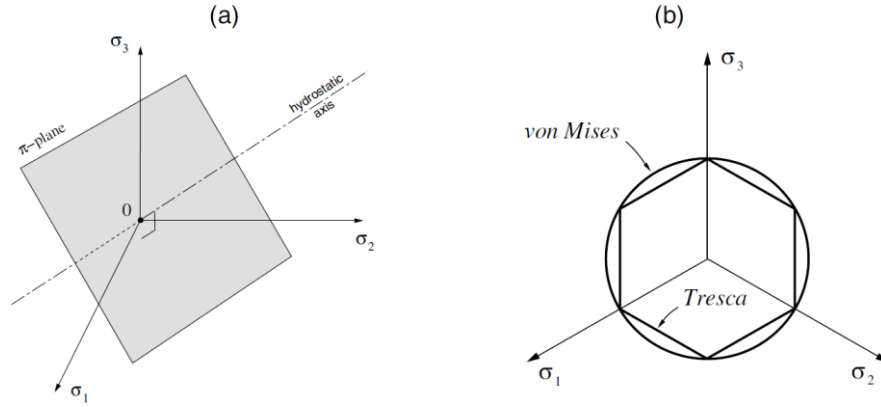


Figure 3.4. (a) The π -plane in principal stress space, and (b) The projection of the Tresca and von Mises yield surfaces on the π -plane (de Souza Neto et al. 2008).

3.1.2 The von Mises yield criterion

This criterion was proposed by von Mises in 1913. The von Mises yield criterion, similar to the Tresca criterion, is appropriate for describing the plastic yielding in metals. Accordingly, plastic yielding occurs when the J_2 stress deviator invariant reaches a critical value, which is

$$J_2 = R(\alpha) \quad (3.3)$$

Where R is the critical value and is assumed to be a function of a hardening internal value, α (de Souza Neto et al. 2008). In terms of stored elastic strain energy and its components, i.e. distortional and volumetric strain energy, the von Mises criterion states that plastic yielding begins when the distortional elastic strain energy reaches the critical value of R / G , where G is the shear modulus of the material under consideration (de Souza Neto et al. 2008).

As mentioned before, pressure-insensitivity is one of the characteristics of the Tresca criterion. Similarly, the von Mises yield criterion is pressure-insensitive, and only the deviatoric stress affects the plastic yielding. In this regard, a yield function is defined for the von Mises criterion:

$$\Phi(\boldsymbol{\sigma}) = [J_2(s(\boldsymbol{\sigma}))]^{0.5} - \tau_y \quad (3.4)$$

Where $\tau_y \equiv (R)^{0.5}$ is the shear yield stress (de Souza Neto et al. 2008). Another equivalent definition for the yield function is

$$\Phi(\boldsymbol{\sigma}) = q(\boldsymbol{\sigma}) - \sigma_y \quad (3.5)$$

Where $\sigma_y \equiv (3R)^{0.5}$ is the uniaxial yield stress and

$$q(\boldsymbol{\sigma}) = [3 J_2(s(\boldsymbol{\sigma}))]^{0.5} \quad (3.6)$$

is known as the von Mises effective or equivalent stress.

Because the von Mises yield function is defined based on an invariant of the stress tensor, similar to the Tresca yield function, it is an isotropic function of the stress tensor. The yield surface, where $\Phi = 0$, corresponding to the von Mises yield criterion, in the principal stress space, is shown in Figure 3.3. As clear from the figure, the yield surface is represented by the surface of an infinite cylinder, with its axis coinciding with the hydrostatic axis $\sigma_1 = \sigma_2 = \sigma_3$. In addition, the π -plane representation of the von Mises criterion is shown in Figure 3.4. In Figures 3.3 and 3.4, the yield surfaces of the von Mises and the Tresca criteria are set to match under the uniaxial stress state, where the von Mises circle intersects the vertices of the Tresca hexagon. In pure shear, on the other hand, the von Mises circle (interior) becomes tangent to the sides of the Tresca hexagon (exterior).

3.1.3 The Mohr-Coulomb (MC) yield criterion

The Mohr-Coulomb (MC) yield criterion is more complete than the aforementioned two criteria, i.e. the Tresca and von Mises criteria, since it considers the pressure sensitivity of the material under consideration. As a result, it can be employed in modeling the behavioral characteristics of materials such as rocks, soils, concrete, etc. for which there is a strong dependence between the yield limit and applied hydrostatic pressure. The Mohr-Coulomb criterion states that plastic yielding begins when on a plane in the body (e.g. a soil sample) the shearing stress τ and the normal stress σ reach the following critical combination

$$\tau = c + \sigma_n \tan \phi \quad (3.7)$$

where c is the cohesion and ϕ is the angle of internal friction or frictional angle, and the normal stress σ_n is assumed to be positive for compression/compressive stress (de Souza Neto et al. 2008). Accordingly, the yield locus of the Mohr-Coulomb criterion is the set of all the stress states corresponding to a plane on which equation 3.7 holds. In $\tau - \sigma_n$ 2-D space, the yield locus for the Mohr-Coulomb criterion is presented in Figure 3.5, which is the set of all the stress states whose largest Mohr circle (associated with their maximum and minimum principal stresses, σ_{max} and σ_{min}) is tangent to the critical line defined by equation 3.7. Therefore, the elastic domain for the Mohr-Coulomb criterion corresponds to all the stress states whose all three Mohr circles are below the critical line (eq. 3.7). According to de Souza Neto et al. (2008), a yield function for the Mohr-Coulomb criterion, in terms of principal stresses, is defined as

$$\Phi(\boldsymbol{\sigma}, c) = (\sigma_{max} - \sigma_{min}) - (\sigma_{max} + \sigma_{min}) \sin \phi - 2 c \cos \phi \quad (3.8)$$

which due to its definition is an isotropic function of the stress tensor $\boldsymbol{\sigma}$.

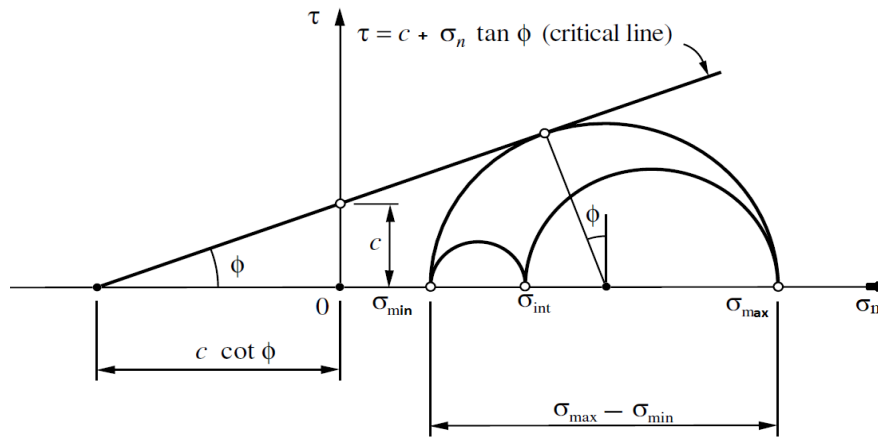


Figure 3.5. Mohr-Coulomb criterion in $\tau - \sigma$ space (de Souza Neto et al. 2008).

The corresponding yield surface ($\Phi = 0$) for the MC criterion, in the principal stress space, is a hexagonal pyramid with its central axis passing through the apex being the hydrostatic axis ($\sigma_1 = \sigma_2 = \sigma_3$). The yield surface is shown in the figure

below. The apex of the hexagonal pyramid (point A in Fig. 3.6) is located at $p = c \cot \phi$ on the tensile side of the hydrostatic axis, defining the resistance limit of the material under tensile stresses, which is a typical characteristic for materials such as soils, rocks, concrete, etc. In addition, it's worth mentioning that the pyramidal shape of the MC yield surface, as opposed to the prismatic and cylindrical shapes of the Tresca and von Mises criteria, is because of its pressure sensitivity.

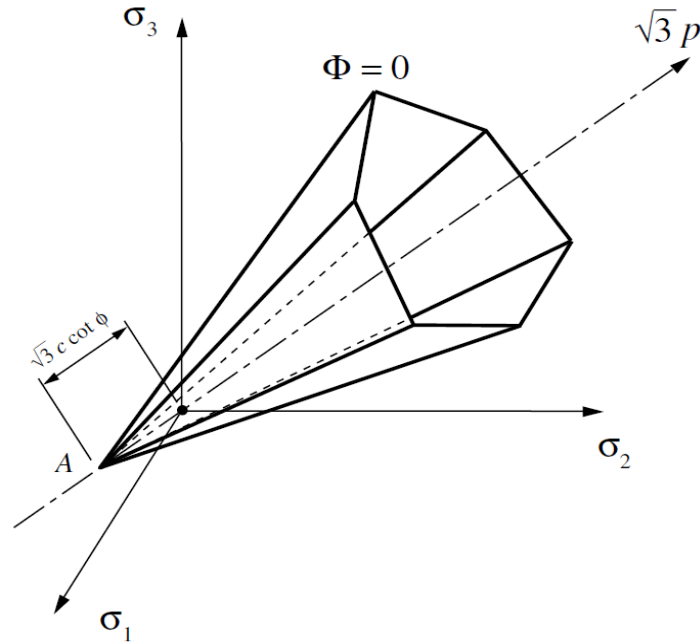


Figure 3.6. Mohr-Coulomb yield surface in principal stress space (de Souza Neto et al. 2008).

Similar to the multi-surface representation of the Tresca yield criterion, the Mohr-Coulomb criterion can be defined by six yield functions, $\Phi_i(\boldsymbol{\sigma}, c) = 0$ for $i = 1 : 6$, corresponding to six faces of the MC pyramid represented in Figure 3.6. Also, the Mohr-Coulomb criterion can be expressed by the invariant representation, which again, similar to the Tresca criterion, can result in more complex numerical algorithms compared to the multi-surface representation.

3.1.4 The Drucker-Prager (DP) yield criterion

According to de Souza Neto et al. (2008) “this criterion was proposed by Drucker and Prager in 1952 as a generalization and a smooth approximation to the Mohr-Coulomb criterion. It consists of a modification of the von Mises criterion in which an extra term is included to incorporate the pressure-sensitivity into the model. The Drucker-Prager (DP) criterion states that plastic yielding occurs when the J_2 invariant of the deviatoric stress, s , and the hydrostatic stress, p , reach the following critical combination:

$$[J_2 (s)]^{0.5} + \eta p = \acute{c} \quad (3.9)$$

where η and \acute{c} are the material parameters.”

In principal stress space, the yield locus of the DP criterion is a circular cone with its axis being the hydrostatic axis ($\sigma_1 = \sigma_2 = \sigma_3$). The DP yield surface, i.e. the corresponding circular cone, is shown in Figure 3.7.

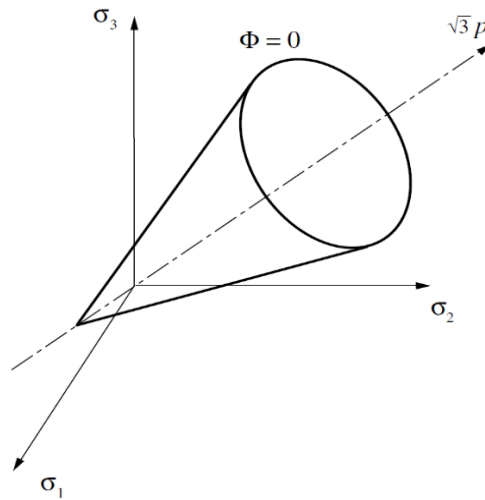


Figure 3.7. The Drucker-Prager yield surface in principal stress space (de Souza Neto et al. 2008).

The yield function for the Drucker-Prager criterion is defined as:

$$\Phi (\boldsymbol{\sigma}, c) = [J_2 (s(\boldsymbol{\sigma}))]^{0.5} + \eta p(\boldsymbol{\sigma}) - \acute{c} \quad (3.10)$$

where c is the cohesion, and the material parameters η and ζ are determined according to the approximation of the DP criterion to the MC criterion (de Souza Neto et al. 2008). Similar to the MC criterion, the isotropy of the DP yield function comes from the fact that the invariants of the stress tensor ($J_2 (s)$ and p) are considered in its definition. In Figure 3.8, the π -plane section of the two common approximations between the MC and DP yield criteria is depicted, where the yield surfaces of the DP model coincide with the outer and the inner edges of the MC yield surface. The outer and the inner DP cones are also known as the compression and the tension cones respectively (de Souza Neto et al. 2008).

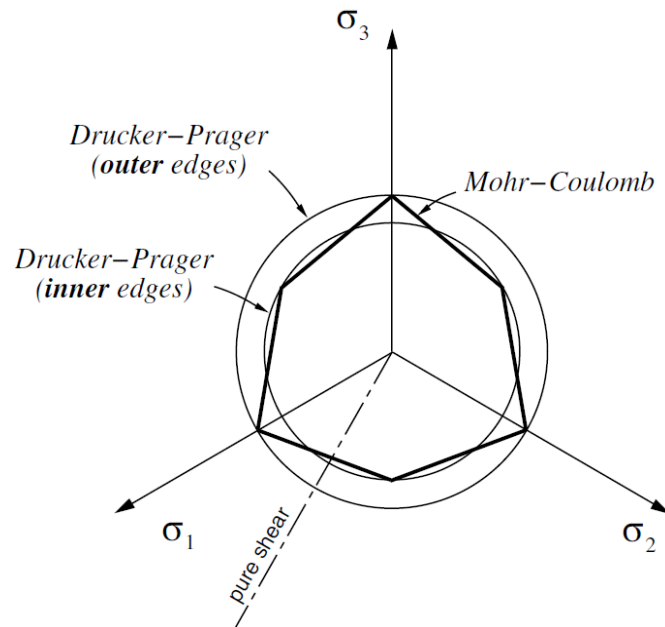


Figure 3.8. The π -plane section of two approximations between the Drucker-Prager and the Mohr-Coulomb yield surfaces (de Souza Neto et al. 2008).

Another important approximation of the DP model to the MC criterion corresponds to forcing both criteria to obtain identical collapse loads under plane strain condition, for which the material parameters η and ζ are defined as

$$\eta = 3 \tan \varphi / (9 + 12 \tan^2 \varphi)^{0.5}, \quad \zeta = 3 / (9 + 12 \tan^2 \varphi)^{0.5} \quad (3.11)$$

where φ is the angle of internal friction introduced in the formulation of the Mohr-Coulomb yield criterion (de Souza Neto et al. 2008).

For all the above-mentioned approximations, between the Drucker-Prager and Mohr-Coulomb criteria, the apex of the DP cone coincides with the apex of the MC hexagonal pyramid (shown in Figs. 3.6 and 3.7). There are other approximations of the DP to the MC criterion as well, explained and discussed in studies by researchers such as Chen (1982), and Chen and Mizuno (1990). However, it should be emphasized that in each case, depending on the dominant stress and strain states of the specific problem under consideration, the most appropriate approximation should be employed, otherwise, the corresponding analysis might lead to poor description of the material behavior and unrealistic results.

3.2 Finite Element Method (FEM)

Many physical phenomena in engineering and science can be described in terms of partial differential equations (defined over a body subject to initial and boundary conditions) which, in general, in most cases, cannot be solved by classical analytical methods for arbitrary and complex shapes. The finite element method (FEM) is a numerical approach for solving these partial differential equations approximately (Fish and Belytschko 2007). The basic idea of the FEM is to divide the body (which can be one dimensional, a line, or two or three dimensional, a surface or a volume, depending on the problem at hand) into finite elements connected by nodes, and obtain an approximate solution. In Figure 3.9, a two-dimensional (2D) body (e.g. a thin plate with a hole) is shown, where the loading is applied on the side walls of the plate and the entire body is mesh-generated with triangular finite elements.

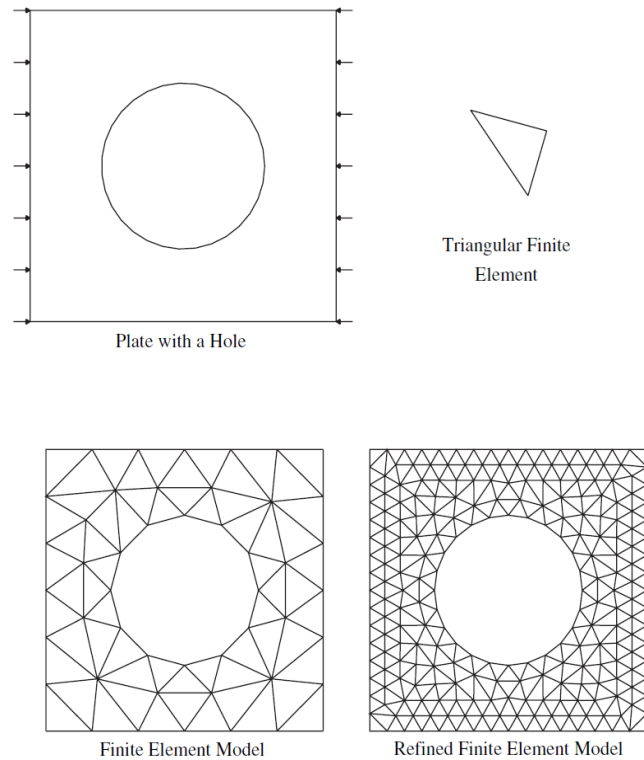


Figure 3.9. The finite element model of a 2D body, a thin plate with a hole: The loading on the side walls, the triangular finite element, and two types of mesh generated for the body (Fish and Belytschko 2007).

When dealing with linear conditions, for instance, the solution to the problem is determined through solving a system of linear equations, where the number of unknowns is determined based on the number of nodes of the finite element model (= the mesh-generated body). Generally, the accuracy of the results improves by increasing the number of elements (and therefore the nodes of the model). An example of a refined finite element model is presented in Figure 3.9. However, by increasing the number of elements of the model, the computational cost (i.e. the analysis time) would also increase, even if we are using high speed computers. Finally the results are presented as computer visualisations, such as diagrams and contour plots, etc., which will be later employed for design purposes in engineering applications.

According to Fish and Belytschko (2007), FEM consists of five main steps:

- “1- Preprocessing: subdividing the problem domain into finite elements. In today’s computer aided engineering (CAE) environment, this step is implemented by automatic mesh generators.
- 2- Element formulation: development of equations for elements. This requires the determination of the partial differential equations for the problem under consideration and its weak form.
- 3- Assembly: obtaining the equations of the entire system from combining the equations governing individual elements. The element, and thus the system, equations are expressed in matrix form.
- 4- Solving the equations.
- 5- Postprocessing: determining and obtaining different quantities, such as stresses and strains, and corresponding plots and diagrams.”

With regard to the above-mentioned steps, some key and basic concepts need to be introduced and explained briefly, without going into too much detail. Normally, in the beginning, it is assumed that displacements and rotations are small so the difference between the deformed and undeformed configurations (a term used in continuum mechanics to depict the time and space coordination of the body under consideration) would be negligible. Needless to say, generalizing the method to incorporate large displacements and rotations can be done with no major difficulty. The finite element method (FEM) is a displacement method since it involves the determination of the unknown displacement field $u(x)$. In the figure below, a body, V , with boundary $\Gamma \equiv \Gamma_u + \Gamma_t$ is shown, where displacements, u_i^b , and tractions, f_i^s , are specified on the displacement boundary, Γ_u , and on the traction boundary, Γ_t , respectively.

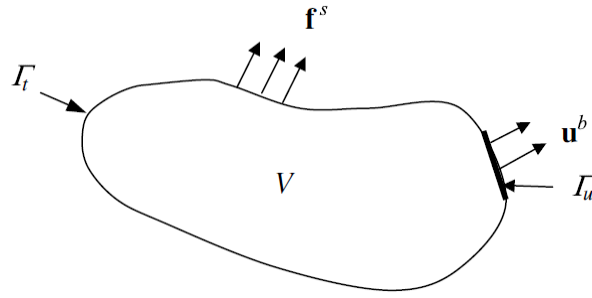


Figure 3.10. Body V subject to applied displacements and tractions.

The key equations, when solving a solid mechanics problem, are the equations of conservation of linear momentum and traction boundary conditions, sometimes known as the “strong form” of the momentum balance. The strong form can be converted to the “weak (=global or integral) form”, also known as the principle of virtual work. By employing the FEM, the goal is to determine a displacement field, \mathbf{u} , which satisfies the momentum balance equations (here the weak form) as well as the displacement boundary conditions, $\mathbf{u} = \mathbf{u}^b$ on Γ_u , shown in Figure 3.10 (Zienkiewicz and Taylor 2000a&b). To solve the weak form equation, first, the body V is discretized, i.e. divided into reasonably small-sized elements, as shown before in Figure 3.9. Along the sides of each element, nodes are designated defining the element’s shape. This is represented in the figure below, where the specific element shown is a square, while there are elements on the surface of the body in the shape of triangle or quadrilateral (see Fig. 3.11). It is worth mentioning that, in general, elements can take any shape, although, for most finite element formulations the highest accuracy is achieved when the elements are rectangles, and more specifically squares (Zienkiewicz and Taylor 2000a&b). The entire collection of nodes and elements, representing the body V , is referred to as the finite element mesh. The number of nodes, N_n , and the number of elements, N_e , are not equal in general ($N_n \neq N_e$). The unknown displacement field, $u_i(\mathbf{x})$, within the domain (=body) V , is defined using the (known) interpolation functions (also referred to as shape functions), $N_a(\mathbf{x})$, and the discrete (unknown) nodal displacements, U_i^a . After doing all the required rearrangements and parametrizations within the weak form (or virtual work) equation, the finite element equation simply becomes:

$$\text{internal nodal forces} = \text{external nodal forces} \quad (3.12)$$

which is a vector equation with NDF (number of spatial degrees of freedom) $\times N_n$ (number of nodes) terms. This equation is further simplified by using the constitutive law to write the stresses in terms of the unknown nodal displacements, U_i^a . The special case of linear elasticity, considering small strains/displacements, can be formulated quite straightforward, leading to the final form of:

$$\mathbf{K} \mathbf{U} = \mathbf{f} \quad (3.13)$$

where \mathbf{U} is the vector of unknown nodal displacements (e.g. U_2^1 is the displacement at node 1 in the 2 or y direction), \mathbf{f} is the nodal force vector, and \mathbf{K} is the stiffness matrix for the finite element model (Zienkiewicz and Taylor 2000a&b). The solution to Eq. 3.13, for unknown displacements, involves the inversion of the stiffness matrix: $\mathbf{U} = \mathbf{K}^{-1} \mathbf{f}$. When dealing with more general conditions, with non-linear material behavior, the formulation is similar to Eq. 3.13. However, the stiffness matrix, \mathbf{K} , is not constant anymore, instead, it will depend on the applied load or displacement. As a result, the finite element equations become nonlinear and cannot be solved in one single step, i.e. an iteration procedure needs to be incorporated into the solution process (Zienkiewicz and Taylor 2000a&b).

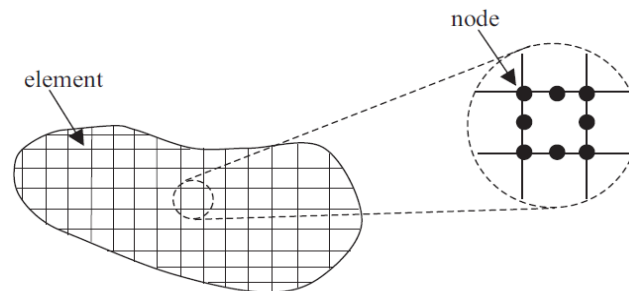


Figure 3.11. Body V divided into finite elements. Nodes along the sides of the element define its shape to be a square.

A major task in any finite element analysis is the calculation and inversion of the stiffness matrix \mathbf{K} , introduced earlier, which is often referred to as the “global” stiffness matrix. In a nonlinear finite element analysis, because of the iterative nature of the solution process, the calculation of the global stiffness matrix \mathbf{K} might be

implemented many hundreds to thousands of times. The number of members of this matrix (or simply the size of stiffness matrix \mathbf{K}) depends on the number of nodes and the number of degrees of freedom of the finite element model (= mesh generated body in the problem at hand). For instance, the term K_{iakk} can be interpreted as the stiffness at node a ($a = 1 : N_n$) in the degree of freedom i ($i = 1 : 2$ or 3 in general) due to the movement of node b ($b = 1 : N_n$) in the degree of freedom k ($k = 1 : 2$ or 3) (Zienkiewicz and Taylor 2000a&b). In order to determine the global stiffness matrix, first, some calculations need to be performed at the element level. As a basic principle of the FEM, all the calculations conducted at the element level only require information from the element itself, therefore, each element can be treated independently (Zienkiewicz and Taylor 2000a&b). To each element, in the finite element model, a “local” stiffness matrix is assigned, then, all the local stiffness matrices contribute to the global stiffness matrix \mathbf{K} through the “assembly” procedure.

At the element level, as mentioned before, calculations for a specific variable within an element are performed by using just the local (= element) shape functions $N_a^e(\mathbf{x})$, also known as the local interpolation functions, and the nodal values of the variable in that element (Zienkiewicz and Taylor 2000a&b). For example, the displacement, \mathbf{u} , within an element is given by:

$$u_i(\mathbf{x}) = \sum_{a=1}^{NEL} N_a^e(\mathbf{x}) U_i^a \quad (3.14)$$

where NEL is the number of nodes per element, and U_i^a represents the nodal displacements of the element. The global shape (or interpolation) functions $N_a(\mathbf{x})$, on the other hand, are used for the interpolation of variables, such as the displacement field, over the entire domain (=body), and they are constructed by adding/assembling the element shape functions $N_a^e(\mathbf{x})$.

$$N_a(\mathbf{x}) = \sum_{e=1}^{N_e} N_a^e(\mathbf{x}) \quad (3.15)$$

N_e in the above equation is the total number of elements in the finite element model. Also, the local shape functions are set to be zero outside their respective elements, i.e.

$N_a^e(\mathbf{x}) = 0$ outside element e , which ensures that the displacements are continuous throughout the entire domain, and the displacement within an element only depends on the nodal displacements of that element (Zienkiewicz and Taylor 2000a&b).

There are of course more details and notes regarding the finite element analysis, but here, the goal was to present an overview of the topic. The references mentioned so far throughout this section are very good for more in-depth explanations and details on FEM.

3.3 The current MATLAB code incorporating FEM for slope stability analysis

In this study, a MATLAB code, incorporating the finite element method (FEM), is employed to perform stability analysis on frozen soil slopes. Here, within the finite element method (FEM), an improved form of the implicit return-mapping scheme for non-smooth yield surfaces (such as the Drucker-Prager yield surface) is defined, which is based on a subdifferential formulation of the potential flow rule (Sysala et al. 2016). This improved scheme, according to Sysala et al. (2016), is significantly helpful in dealing with singular points, i.e. the apices or edges on the yield surface, where the flow direction is multivalued. Accordingly, only a uniquely defined set of nonlinear equations is introduced, similarly to smooth yield surfaces (such as the von Mises yield surface), which makes the computational procedure less cumbersome and costly (Sysala et al. 2016). The problem at hand is categorized as a small-strain quasi-static elastoplastic problem, consisting of the constitutive initial value problem (CIVP) and the balance equation of the principle of virtual work. Sysala et al. (2016) note that the computational process for solving such problems consists of the following main steps:

“1- Time discretization of CIVP leading to an incremental constitutive problem.

2- Derivation of the constitutive and consistent tangent operators.

- 3- Substitution of the constitutive stress-strain operator into the balance equation, resulting in the development of the incremental boundary value problem in terms of displacements.
- 4- Finite element discretization and derivation of a system of nonlinear equations.
- 5- Solving the system of nonlinear equations using a (nonsmooth) variant of the Newton method.”

A few approaches are proposed for the numerical solution of CIVP, amongst which the implicit or trapezoidal Euler approach uses the elastic predictor/plastic corrector (return-mapping algorithm) method (Sysala et al. 2016; de Souza Neto et al. 2008). As mentioned before, if the plastic potential function g , which is closely related to the prescribed yield function f , is equal to the yield function, i.e. $g = f$, it is called associative plasticity. When g is nonsmooth, i.e. the yield surface contains singular points such as apices or edges, then the potential flow function g is rather called the pseudo-potential function, and its derivative does not exist everywhere (Sysala et al. 2016). In associative plasticity, the alternative formulation of CIVP, obtained by considering the principle of maximum plastic dissipation within the constitutive model, can be solved by employing mathematical programming techniques, without the need to consider the smoothness (i.e. being smooth or nonsmooth) of the (pseudo-) potential function g . The reformulations of CIVP correspond to a generalized plastic flow rule:

$$\dot{\boldsymbol{\varepsilon}}^P \in \dot{\lambda} \partial_{\boldsymbol{\sigma}} g(\boldsymbol{\sigma}, A) \quad (3.16)$$

where $\dot{\boldsymbol{\varepsilon}}^P$, $\dot{\lambda}$, $\boldsymbol{\sigma}$, and A are the plastic strain rate, plastic multiplier rate, stress tensor and hardening thermodynamical forces respectively, and $\partial_{\boldsymbol{\sigma}} g(\boldsymbol{\sigma}, A)$ itself is the subdifferential of g at $(\boldsymbol{\sigma}, A)$ with respect to the stress variable (Sysala et al. 2016). An implicit return-mapping algorithm leads to the solution of a system of nonlinear equations for any position of stress $\boldsymbol{\sigma}$ on the yield surface. This approach eliminates the blind guessing of the correct location of the stress tensor $\boldsymbol{\sigma}$ on the yield surface, which significantly simplifies the solution process.

Incorporating the Drucker-Prager (DP) criterion, as the main focus of our study, into the above-mentioned numerical framework, for the elastoplastic problem, is explained in detail by Sysala et al. (2016). The resulting elastoplastic constitutive initial value problem (CIVP) is discretized by the implicit Euler method into N partitions (pseudo time-steps), $0 = t_0 < t_1 < \dots < t_k < \dots < t_N = t_{\max}$. In addition, a finite element discretization of the problem's space (=domain or body) is implemented, similar to what was explained in section 3.2. With both time and space discretization being complete for the problem at hand, the original boundary value problem is reduced to a set of incremental (generally nonlinear) algebraic finite element equations which are solved at each time station of the considered time interval (de Souza Neto et al. 2008). In Figure 3.12, the main steps through which the initial boundary value problem is transformed into a set of incremental finite element equations are depicted. The discrete elastoplastic CIVP is then solved for the k^{th} step, i.e. the pseudo time interval of $t_{k-1} - t_k$, using the elastic predictor/plastic corrector (return-mapping algorithm) method, which is shown schematically in Figure 3.13. The elastic predictor applies when $f(\boldsymbol{\sigma}^{\text{tr}}, H(\boldsymbol{\varepsilon}^{\text{p, tr}})) \leq 0$, i.e. the stress condition remains within the elastic domain. In this relation, f is the yield function of the DP criterion, and H is the strain hardening function. When the relation does not hold, the plastic corrector applies instead. In this regard, the improved return-mapping scheme, introduced by Sysala et al. (2016), leads to the formulation of the plastic corrector problem as a unique system of nonlinear equations. Also, the return of the trial stress condition to either the smooth or nonsmooth (the apex) portions of the yield surface is a priori determined without the need to implement a trial-and-error procedure (Sysala et al. 2016). Next, the unique set of nonlinear equations, obtained for the return to the smooth portion or the apex of the DP yield surface, is solved using the Newton method. A variant of the Newton method, which is called the semismooth Newton method, is employed in the current MATLAB code. The semismooth Newton method is defined by Sysala et al. (2016) through the following algorithm:

- 1: initialization: $\mathbf{u}_k^0 = \mathbf{u}_{k-1}$
- 2: **For** $i = 0, 1, 2, \dots$ **do**
- 3: **find** $\delta \mathbf{u}^i \in \mathbf{V}$: $\mathbf{K}_k(\mathbf{u}_k^i) \delta \mathbf{u}^i = \mathbf{l}_k - \mathbf{F}_k(\mathbf{u}_k^i)$
- 4: **compute** $\mathbf{u}_k^{i+1} = \mathbf{u}_k^i + \delta \mathbf{u}^i$
- 5: **if** $\|\delta \mathbf{u}^i\| / (\|\mathbf{u}_k^{i+1}\| + \|\mathbf{u}_k^i\|) \leq \epsilon_{Newton}$ **then stop**
- 6: **end for**
- 7: **set** $\mathbf{u}_k = \mathbf{u}_k^{i+1}$.

where \mathbf{u}_k^0 is the first try ($i = 0$) for the displacement value at the beginning of the k^{th} time interval. Sysala et al. (2016) point out that the value for the tolerance, i.e. ϵ_{Newton} , should be sufficiently small, and here is set $\epsilon_{Newton} = 10^{-12}$.

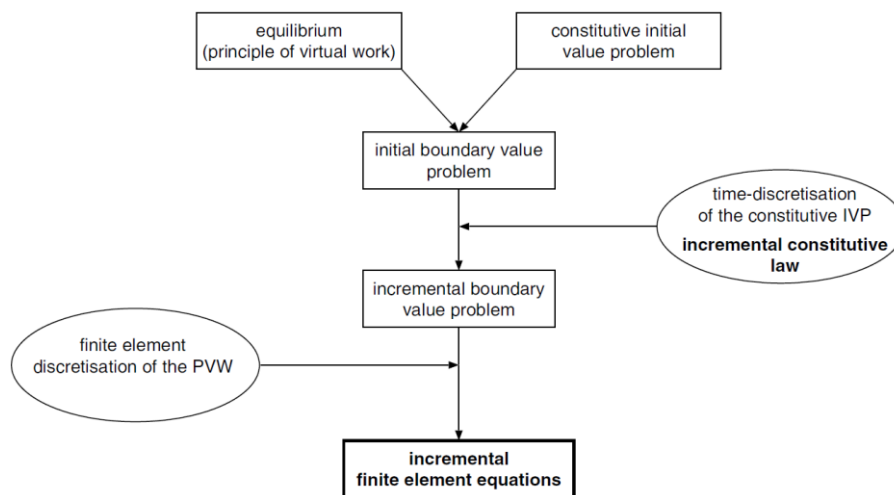


Figure 3.12. Reducing the initial boundary value problem (IBVP) to a set of incremental finite element equations (de Souza Neto et al. 2008).

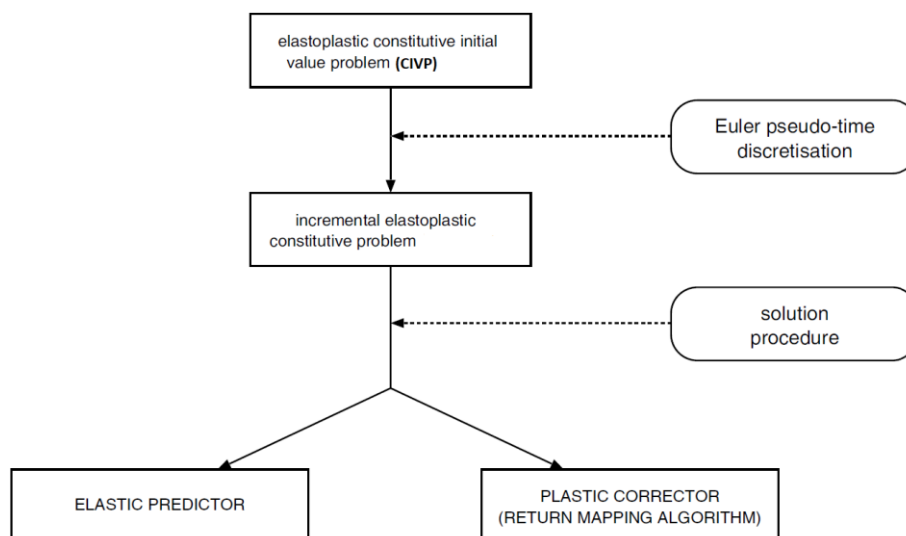


Figure 3.13. From the elastoplastic initial value problem (IVP) to the elastic predictor/return-mapping integration algorithm (de Souza Neto et al. 2008).

As mentioned earlier, in this study, the constitutive behavioral model is the Drucker-Prager (DP) criterion. Here, the associative plasticity, i.e. the pseudo-potential function and the yield function are the same, and the elastic-perfectly plastic behavior are considered for the problem at hand which is the stability analysis of frozen soil slopes. Also, for this type of problem, plane strain assumptions seem to be quite reasonable. The related parameters for the finite element analysis (FEA) of the elastoplastic problem, with the associative DP model (under plane strain conditions), and also the geometry of the model are defined within the MATLAB code. The geometry of the slope stability analysis problem and its finite element mesh-generated model (with quadrilateral elements) are presented in Figure 3.14.

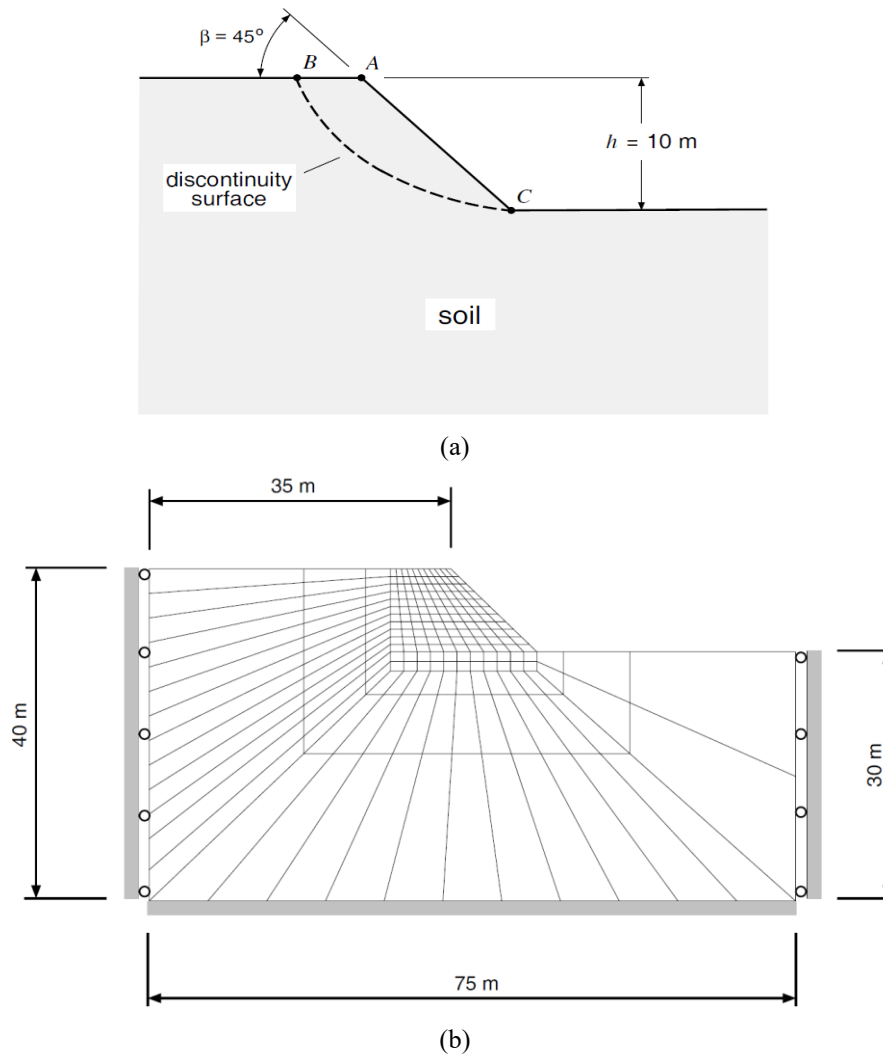


Figure 3.14. (a) Geometry of the slope stability analysis problem, (b) Finite element mesh-generated model with quadrilateral elements refined close to and within the slope's body (de Souza Neto et al. 2008).

As clear from Figure 3.14, the slope height is 10 m with the inclination of 45° . At the bottom, it is assumed that the model (=body or domain) is fixed. Also, the boundaries of the domain to the left, the right, and the bottom are set far enough from the slope body so that no interference of the collapse mechanism with the model boundaries would occur. The plane strain analysis of the slope stability is carried out considering just the self weight of the slope material (here, the frozen soil). The mechanical (strength and deformation) properties of the slope material including specific weight, γ , Young's modulus, E , Poisson's ratio, ν , internal friction angle, φ , and cohesion, c , are defined as the input data for the MATLAB FEA code. As explained by Sysala et al. (2016), the gravity load which is a volume force is multiplied by a scalar factor ζ , and the loading process starts at $\zeta = 0$. The gravity load factor is increased incrementally, e.g. $\delta\zeta = 0.1$. For each increment, the total (or cumulative) settlement at corner point A on top of the slope (shown in Fig. 3.14a) is calculated. When the total settlement at point A reaches a pre-defined value, e.g. 3 m, the slope "collapses", the incremental increase of the load factor ζ stops, and the numerical analysis ends. The final gravity load factor is considered as the "limit load factor" which is equivalent to the factor of safety (FOS) for the slope. Next, the results are represented as the plots of gravity load factor vs. settlement at point A , incremental accumulated plastic strain, incremental nodal displacements, etc., which will be explained and discussed in the following chapter for "Results".

4 Temperature-dependent mechanical properties of frozen soils

In this chapter, a number of studies are reviewed, focusing on the variation of mechanical properties of frozen soils with temperature. Here, three different types of soil (i.e. clay, silt, and sand) are addressed. It should be noted that the parameters presented here are reported by the respective authors, and not necessarily appropriate for the frozen slope stability analysis (which is the main focus of Chapter 5), and in some cases, modifications are required.

4.1 Clay soils

●●● *Akhtar and Li (2020)*

They also mentioned a study by *Hu et al. (2013)* where uniaxial compressive tests were conducted on three different types of artificially frozen soils marine deposit (MD), alluvium, and extremely weak granite (EWG). Hu et al. (2013) considered a wide range of negative temperatures, under a constant strain rate of $1.67E-4$ /sec (in the moderate range of strain rates).

- **Cohesion (c) vs. Temperature (T):** Uniaxial compressive strength for the frozen Hong Kong marine clay deposit (mixture of clay, silt, and fine sand) is defined as C_0 (MPa) = $0.125 (-T)^{1.065}$. From Mohr-Coulomb strength criterion, we have $\sigma_1 = \sigma_3 \cdot \tan^2(45 + \varphi/2) + 2 \cdot c \cdot \tan(45 + \varphi/2)$. For uniaxial compression, $\sigma_1 = C_0$ and $\sigma_3 = 0$. Then, cohesion becomes $c = C_0 / (2 \cdot \tan(45 + \varphi/2))$. A reasonable value for φ is needed. For $\varphi = \varphi_{\max} = 28^\circ$, c (MPa) = $0.037554 (-T)^{1.065}$.

- **Friction angle (φ) vs. Temperature (T):** It is assumed by Akhtar and Li (2020) that temperature has little impact on the frictional angle of frozen clay soils. In their study, for the Hong Kong marine clay deposit, φ_{\max} (peak friction angle) and φ_{cri} (residual friction angle) are reported as 28° and 21.9° respectively.

- **Young's Modulus (E) vs. Temperature (T):** Modulus of elasticity for different negative temperatures is obtained from the ratio of half the compressive strength

$\sigma_{\max}/2$ to its corresponding strain ($E_{50\%}$, also called the Secant modulus). Young's modulus for the frozen Hong Kong marine clay deposit is defined as E (MPa) = $2.676 (-T)^{1.324}$.

- **Poisson's ratio (ν) vs. Temperature (T):** Poisson's ratio for different temperatures is obtained from the ratio of horizontal to vertical strain. Poisson's ratio for the frozen Hong Kong marine clay deposit is defined as $\mu = 0.413 (-T)^{-0.177}$.

In the following table, the abovementioned parameters are presented.

Table 4.1. Mechanical parameters according to the study by Akhtar and Li (2020).

Mechanical parameters as functions of temperature T	Definition/Formulation
Cohesion c (MPa)	$0.125 (-T)^{1.065} / (2.\tan(45+\varphi/2))$
Friction angle φ	φ_{\max} (peak friction angle) = 28°
Young's modulus E (MPa)	$2.676 (-T)^{1.324}$
Poisson's ratio μ	$0.413 (-T)^{-0.177}$

●●● **Bai et al. (2020)**

In their study, isotropic freezing and one-side freezing tests were carried out on a silty soil, then finally, an innovative universal frost heave model for saturated-unsaturated soils was proposed. They also presented different formulae for Cohesion c , friction angle φ , Young's modulus E , and Poisson's ratio ν of **frozen clay** at different temperatures. Similar relationships were proposed by *Li et al. (2015b)*.

- **Cohesion (c) vs. Temperature (T):**

$$c \text{ (kPa)} = \begin{cases} 20 + 6 (T_0 - T)^{1.24} & T \leq T_0 \\ 20 & T > T_0 \end{cases}, \text{ where } T_0 = 0 \text{ }^\circ\text{C}$$

- **Friction angle (φ) vs. Temperature (T):**

$$\varphi \text{ (}^\circ\text{)} = \begin{cases} 20 + 3.4 (T_0 - T)^{0.38} & T \leq T_0 \\ 20 & T > T_0 \end{cases}, \text{ where } T_0 = 0 \text{ }^\circ\text{C}$$

- **Young's modulus (E) vs. Temperature (T):**

$$E_T \text{ (MPa)} = \begin{cases} 20 + 11.3 (T_0 - T)^{0.6} & T \leq T_0 \\ 20 & T > T_0 \end{cases}, \text{ where } T_0 = 0 \text{ }^\circ\text{C}$$

- **Poisson's ratio (ν) vs. Temperature (T):**

$$\nu_T = \begin{cases} 0.28 - 0.007 (T_0 - T) & T \leq T_0 \\ 0.28 & T > T_0 \end{cases}, \text{ where } T_0 = 0 \text{ }^\circ\text{C}$$

●●● ***Girgis et al. (2020)***

A series of uniaxial compressive tests on artificial frozen sandy clay soils (Kaolinite-Sand and Bentonite-Sand mixtures), at temperatures ranging from -15 to 0 °C, under three deformation rates of 1mm/min (=1.64E-4/sec, medium range), 3mm/min (=4.92E-4/sec, medium to high range), and 9mm/min (=1.48E-3/sec, high range).

- **Cohesion (c) vs. Temperature (T):** Uniaxial compression strength (USC) σ_c is given by the equation $\sigma_c = M (T / T_0)^N + Q$, where $T_0 = -1$ °C. From Mohr-Coulomb strength criterion, $\sigma_1 = \sigma_3 \cdot \tan^2(45 + \varphi/2) + 2 \cdot c \cdot \tan(45 + \varphi/2)$. For uniaxial compression, $\sigma_1 = \sigma_c$ and $\sigma_3 = 0$. Then, cohesion becomes $c = \sigma_c / (2 \cdot \tan(45 + \varphi/2))$. Proper values of φ are required in order to determine cohesion c at different temperatures.

- **Young's modulus (E) vs. Temperature (T):** Young's Modulus, E , was calculated using the tangent method at the point with half the peak strength ($E_{50\%}$).

- **Poisson's ratio (ν) vs. Temperature (T):** Poisson's ratio for each test was calculated at the same stress as the Young's Modulus was determined (i.e. at 50% peak strength).

In Tables 4.2 and 4.3, the formulae for cohesion, Young's modulus, and Poisson's ratio as functions of temperature are presented.

Table 4.2. Mechanical parameters of frozen Kaolinite-Sand mixtures according to Girgis et al. (2020).

Mechanical parameters as functions of temperature T	Definition/Formulae for 3 axial strain rates		
	9 mm/min	3 mm/min	1 mm/min
Cohesion c (MPa)	$[0.355(T/T_0)^{0.998}+0.473] / (2.\tan(45 + \varphi/2))$	$[0.258(T/T_0)^{1.062}+0.348] / (2.\tan(45 + \varphi/2))$	$[0.197(T/T_0)^{1.093}+0.192] / (2.\tan(45 + \varphi/2))$
Young's modulus $E_{50\%}$ (MPa)	$11(T/T_0)^{1.116}+14.98$	$5.40(T/T_0)^{1.29}+12.38$	$3.154(T/T_0)^{1.422}+8.77$
Poisson's ratio ν	$-0.069(T/T_0)^{0.3}+0.350$	$-0.066(T/T_0)^{0.3}+0.373$	$-0.061(T/T_0)^{0.3}+0.409$

Table 4.3. Mechanical parameters of frozen Bentonite-Sand mixtures according to Girgis et al. (2020).

Mechanical parameters as functions of temperature T	Definition/Formulae for 3 axial strain rates		
	9 mm/min	3 mm/min	1 mm/min
Cohesion c (MPa)	$[0.41(T/T_0)^{0.996}+0.547] / (2.\tan(45 + \varphi/2))$	$[0.281(T/T_0)^{1.082}+0.389] / (2.\tan(45 + \varphi/2))$	$[0.206(T/T_0)^{1.11}+0.307] / (2.\tan(45 + \varphi/2))$
Young's modulus $E_{50\%}$ (MPa)	$12.85(T/T_0)^{1.082}+16.592$	$7.235(T/T_0)^{1.261}+12.621$	$4.468(T/T_0)^{1.31}+9.594$
Poisson's ratio ν	$-0.069(T/T_0)^{0.3}+0.340$	$-0.065(T/T_0)^{0.3}+0.361$	$-0.069(T/T_0)^{0.3}+0.399$

●●● *Li et al. (2019)*

Numerous researchers have performed uniaxial and triaxial tests on frozen soils. According to their results, cohesion c , friction angle φ , Young's modulus E , and Poisson's ratio ν of the frozen clay at different temperatures can be approximated as follows:

1- Cohesion (c) vs. Temperature (T):

$$c \text{ (kPa)} = \begin{cases} 10 * [1 + 1.2 * (T / -0.2)] & T < -0.2 \text{ }^\circ\text{C} \\ 10 * [0.104 * (0.155 * [T / -0.2]^{-0.243})^2 - 2.84 * (0.155 * [T / -0.2]^{-0.243}) + 1.72] & T \geq -0.2 \text{ }^\circ\text{C} \end{cases}$$

2- Friction angle (φ) vs. Temperature (T):

$$\varphi \text{ (}^\circ\text{)} = \begin{cases} 20 * [1 + 6.41\text{E-}2 * (T / -0.2)^{1.39}] & T < -0.2 \text{ }^\circ\text{C} \\ 20 * [0.327 * (0.155 * [T / -0.2]^{-0.243})^2 - 1.41 * (0.155 * [T / -0.2]^{-0.243}) + 1.34] & T \geq -0.2 \text{ }^\circ\text{C} \end{cases}$$

3- Young's Modulus (E) vs. Temperature (T):

$$E \text{ (MPa)} = \begin{cases} 75 * [1 + 0.345 * (T / -0.2)^{0.6}] & T < -0.2 \text{ }^\circ\text{C} \\ 75 * [0.446 * (0.155 * [T / -0.2]^{-0.243})^2 - 2.65 * (0.155 * [T / -0.2]^{-0.243}) + 1.67] & T \geq -0.2 \text{ }^\circ\text{C} \end{cases}$$

4- Poisson's ratio (ν) vs. Temperature (T):

$$\nu = \begin{cases} 0.28 * [1 - 5\text{E-}3 * (T / -0.2)] & T < -0.2 \text{ }^\circ\text{C} \\ 0.28 & T \geq -0.2 \text{ }^\circ\text{C} \end{cases}$$

●●● Wang et al. (2017)

Triaxial compression tests, with low-to-medium confining pressures (100 – 400 kPa), were performed on frozen samples of re-constituted high plasticity Kasaoka clay, at temperatures $T = -2, -5, -10 \text{ }^\circ\text{C}$, under the strain rates of $1.67\text{E-}7/\text{sec}$ (slow), $1.67\text{E-}6/\text{sec}$ (slow), and $1.67\text{E-}5/\text{sec}$ (moderate). According to the results, strength and deformation parameters are determined as follows:

- Cohesion (c) vs. Temperature (T): According to deviatoric stress vs. axial strain curves ($\sigma_1 - \sigma_3$ vs. ε_1 curves), considering axial strains of $\varepsilon_1 = 15\text{-}20\%$ as failure strains, and also the linear Mohr-Coulomb strength criterion, $\sigma_1 - \sigma_3 = (\sigma_1 + \sigma_3) \cdot \sin\varphi + 2 \cdot c \cdot \cos\varphi$, cohesion values at $T = -2, -5$ and $-10 \text{ }^\circ\text{C}$ are calculated to be $c = 0.10, 0.28$, and 0.2 MPa respectively.

- **Friction angle (φ) vs. Temperature (T):** Considering the deviatoric stress vs. axial strain curves ($\sigma_1 - \sigma_3$ vs. ε_1 curves), similar to the process of calculating cohesion values, the friction angles at $T = -2, -5$ and -10°C are calculated to be $\varphi = 17^\circ, 18^\circ$ and 36° respectively.

- **Young's Modulus (E) vs. Temperature (T):** According to deviatoric stress vs. axial strain curves ($\sigma_1 - \sigma_3$ vs. ε_1 curves), secant modulus (at 50% peak strength) for each temperature is determined: $T = -2^\circ\text{C} \rightarrow E_{50\%} = 45$ MPa, $T = -5^\circ\text{C} \rightarrow E_{50\%} = 184.5$ MPa, $T = -10^\circ\text{C} \rightarrow E_{50\%} = 100$ MPa.

The abovementioned values for c , φ , and E parameters are also presented in the table below:

Table 4.4. Mechanical parameters of frozen Kasaoka clay according to Wang et al. (2017).

Mechanical parameters as functions of temperature T	Parameter values at 3 different temperatures		
	-2°C	-5°C	-10°C
Cohesion c (MPa)	0.1	0.28	0.2
Friction angle φ ($^\circ$)	17	18	36
Young's modulus $E_{50\%}$ (MPa)	45	184.5	100

4.2 Silt soils

●●● *Haynes and Karalius (1977)*

Uniaxial unconfined compression tests were performed on frozen Fairbanks silt, at a temperature range of 0 to -56.7°C , under two constant deformation/strain rates of 4.23 cm/sec ($\approx 0.4/\text{sec}$) and 0.0423 cm/sec ($\approx 4\text{E-}3/\text{sec}$). Both strain rates are within the high range for strain rates. Because the strain rate of 0.4/sec is very high, compared to common strain rates considered in different studies, only the results corresponding to the strain rate of 4E-3/sec are focused on here.

- **Cohesion (*c*) vs. Temperature (*T*):** The average compression strength at negative temperatures is determined for the two applied deformation/strain rates:

$\sigma_{4.23} = 7.64 - 1.362 * T$ is the compressive strength corresponding to the higher deformation rate, i.e. 4.23 cm/sec, and

$\sigma_{0.0423} = 2.15 - 0.33 * T + 0.01 * T^2$ is the compressive strength for the lower deformation rate 0.0423 cm/sec. Considering the Mohr-Coulomb strength criterion:

$\sigma_1 = \sigma_3 \cdot \tan^2(45 + \varphi/2) + 2 \cdot c \cdot \tan(45 + \varphi/2)$, for the uniaxial compression, $\sigma_3 = 0$ and σ_1 is the unconfined compressive strength (given as $\sigma_{4.23}$ and $\sigma_{0.0423}$). Then cohesion becomes $c = \sigma_1 / (2 \cdot \tan(45 + \varphi/2))$. Proper values of φ at below zero temperatures are needed to determine cohesion c at different temperatures.

- **Young's Modulus (*E*) vs. Temperature (*T*):** The results by Haynes and Karalius (1977) also included the correlations between initial tangent modulus and temperature (Fig. 4.1a), and modulus at 50% strength and temperature (Fig. 4.1b). Here, our focus is on the compression test results, i.e. (C) and (D) curves. As clear from the plots, the modulus (either initial or 50% strength) increases with decreasing temperature.

The formulae for cohesion as a function of temperature and friction angle are presented in the table below.

Table 4.5. Mechanical parameters of frozen Fairbanks silt according to Haynes and Karalius (1977).

Mechanical parameters	Definition/Formulae for 2 axial strain rates	
	4.23 cm/sec	0.0423 cm/sec
Cohesion <i>c</i> (MPa)	$[7.64 - 1.362 * T] / (2 * \tan(45 + \varphi/2))$	$[2.15 - 0.33 * T + 0.01 * T^2] / (2 * \tan(45 + \varphi/2))$

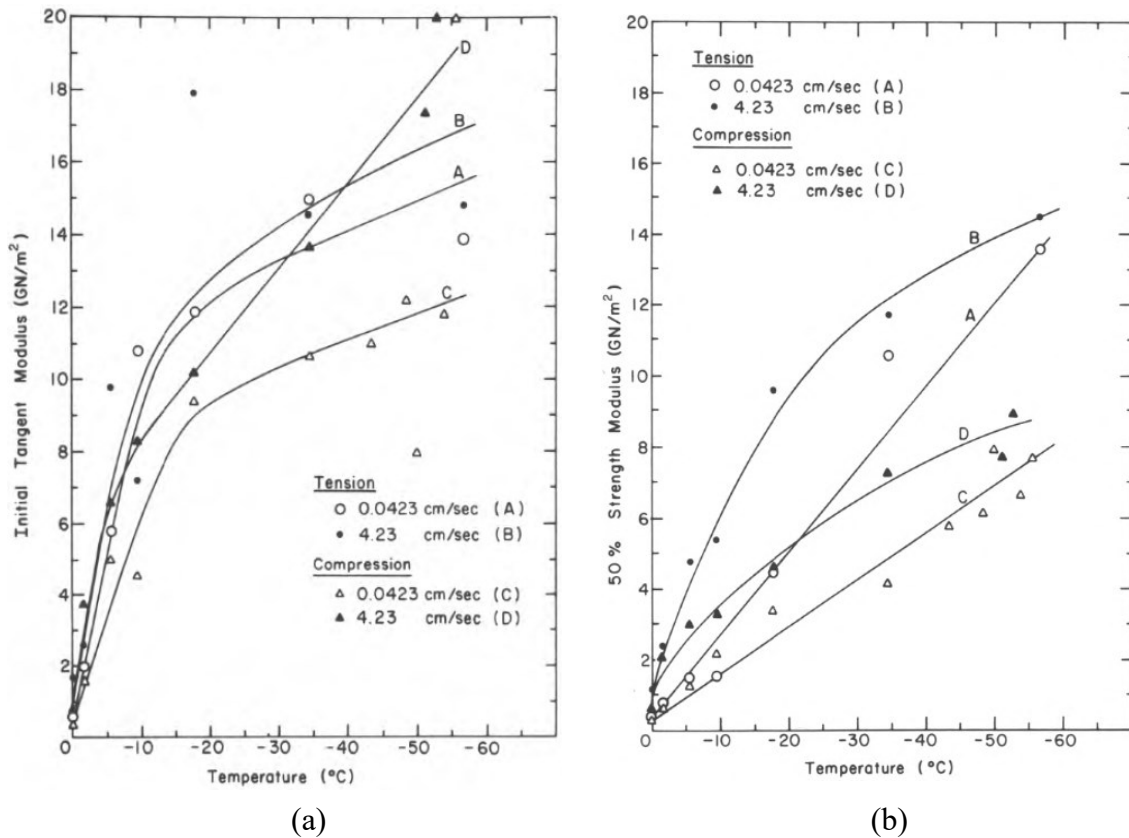


Figure 4.1. (a) initial tangent modulus vs. temperature and (b) modulus at 50% strength vs. temperature (Haynes and Karalius 1977).

●●● *Sayles and Carbee (1981)*

A series of uniaxial unconfined compression tests were conducted on frozen samples of remolded saturated Fairbanks silt (also called remolded wind-laid silt) at dry unit weights γ_d ranging from 9.75 to 14.62 kN/m³, with total water contents $w\%$ ranging from 28% to 58%. The soil was non-plastic, with traces of decayed vegetation. The test temperature was fixed at $T = -1.67$ °C, and the constant axial strain rate was $\dot{\epsilon} = 5E-3/\text{sec}$ (within the high range of strain rates). In the following figure, typical compressive stress-strain curves for different water content groups (written on each curve) are shown. It is pointed out by Sayles and Carbee (1981) that, in general, ice fractures at low strain levels (below 0.05=5%), but most frozen soils do not reach maximum strength until much larger strains, sometimes as high as 30% (=0.30). The fracture of ice normally does not occur at the same strain level as the one where the frictional resistance is fully developed, specifically when the applied axial strain rate

is within the high range. Therefore, in characterising the frozen soil strength, the fracture of ice content should be considered as the initial onset of failure. In addition, at dry unit weights higher than the medium level, the frictional resistance dominates the strength of frozen soils even at small strains. As a result, the strength would increase with increasing the dry unit weight. Under low-to-medium strain rates, for the soils with medium-to-high dry unit weights, the two different sources of frozen soil strength, i.e. cohesion of the ice matrix and frictional resistance of the soil grains in combination with that of the fractured ice crystals, presumably get activated in a narrow strain range (almost at the same time).

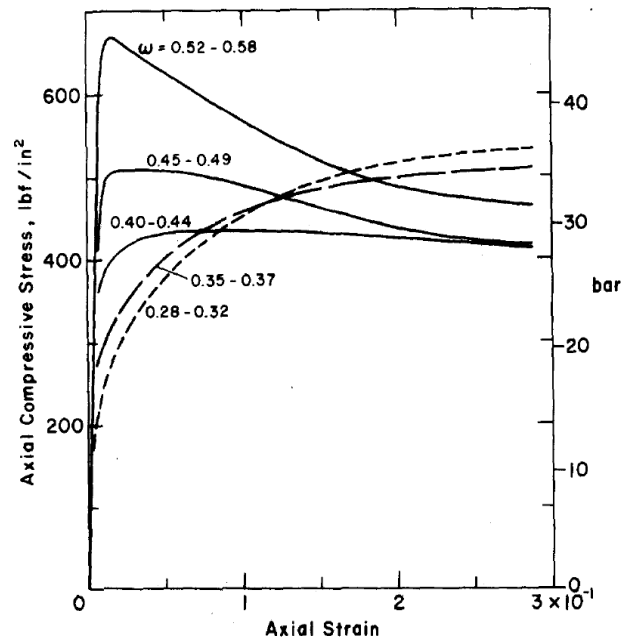


Figure 4.2. Average compressive stress-strain curves for different total water content ranges at $T = -1.67\text{ }^{\circ}\text{C}$ (Sayles and Carbee 1981).

- **Cohesion (c) vs. Temperature (T):** According to Figure 4.2, and other results reported by Sayles and Carbee (1981), the axial compressive strength for a specific (range of) water content can be defined. For instance, for $\omega = 35\%$ and $\gamma_d = 13\text{ kN/m}^3$, uniaxial compressive strength is $\sigma_1 \approx 35\text{ bar} = 3.5\text{ MPa}$. Considering the Mohr-Coulomb strength criterion: $\sigma_1 = \sigma_3 \cdot \tan^2(45 + \varphi/2) + 2 \cdot c \cdot \tan(45 + \varphi/2)$, for uniaxial compression, $\sigma_3 = 0$ and σ_1 is the axial compressive strength determined from Figure

4.2. Then, cohesion becomes $c = \sigma_1 / (2.\tan(45+\varphi/2))$. Proper value of φ , at $T = -1.67$ °C, is required in order to determine cohesion c .

- **Young's Modulus (E) vs. Temperature (T):** Considering the curve for $\omega = 35\%$ and $\gamma_d = 13$ kN/m³ (in Figure 4.2) as already the uniaxial compressive strength was obtained to be $\sigma_1 = 35$ bar = 3.5 MPa, the 50% peak strength modulus (the Secant modulus) is determined to be $E_{50\%} \approx 311.92$ MPa.

The values of cohesion and Young's modulus are presented also in the table below.

Table 4.6. Mechanical parameters of frozen Fairbanks silt according to Sayles and Carbee (1981).

Mechanical parameters	Definition/Formulae
	$T = -1.67$ °C
Cohesion c (MPa)	$3.5 / (2.\tan(45+\varphi/2))$
Young's modulus $E_{50\%}$ (MPa)	311.92

●●● **Zhu and Carbee (1984)**

Uniaxial unconfined compressive strength tests were performed on the remolded, saturated, frozen Fairbanks silt under various constant axial strain rates (1.1E-6 to 6.2E-2 /sec), temperatures (-0.5 to -10 °C), and dry densities ($\rho_d = 1080$ to 1430 kg/m³). The soil was classified as a fine-grained low-plasticity silt (ML in the plasticity chart).

- **Cohesion (c) vs. Temperature (T):** In Figure 4.3, peak compressive strength, σ_m , is presented for different temperature values and axial strain rates. In this plot, the range of dry densities is 1180–1230 kg/m³. Considering the Mohr-Coulomb strength criterion: $\sigma_m = \sigma_1 = \sigma_3.\tan^2(45 + \varphi/2) + 2.c.\tan(45 + \varphi/2)$, for uniaxial compression, $\sigma_3 = 0$. Then, cohesion becomes $c = \sigma_m / (2.\tan(45+\varphi/2))$. Appropriate values of φ at negative temperatures are needed in order to determine cohesion c at different temperatures.

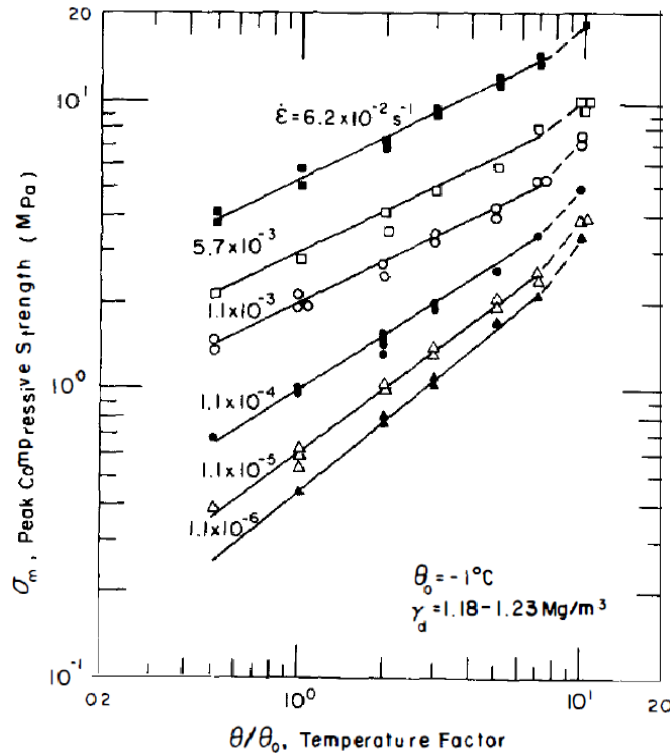
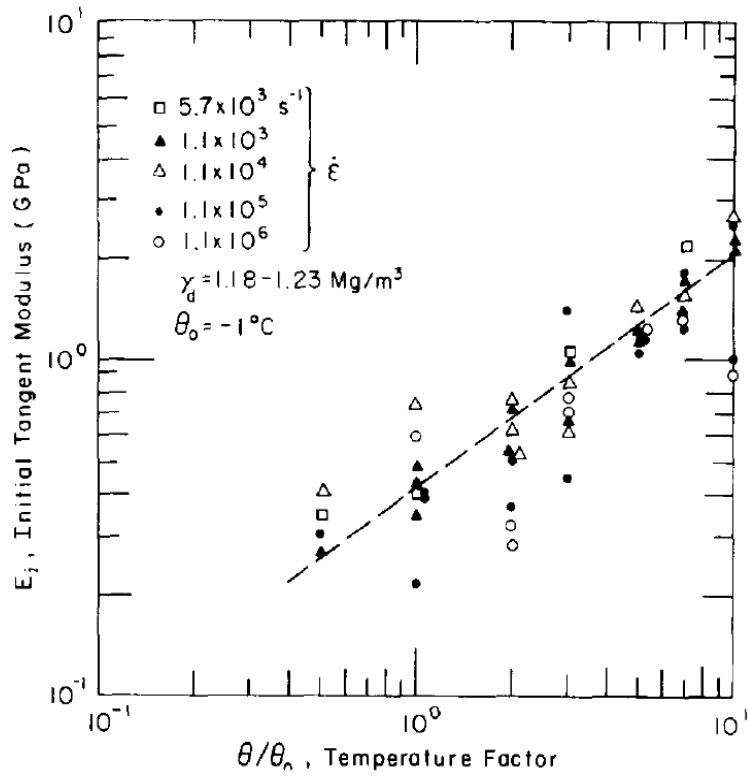


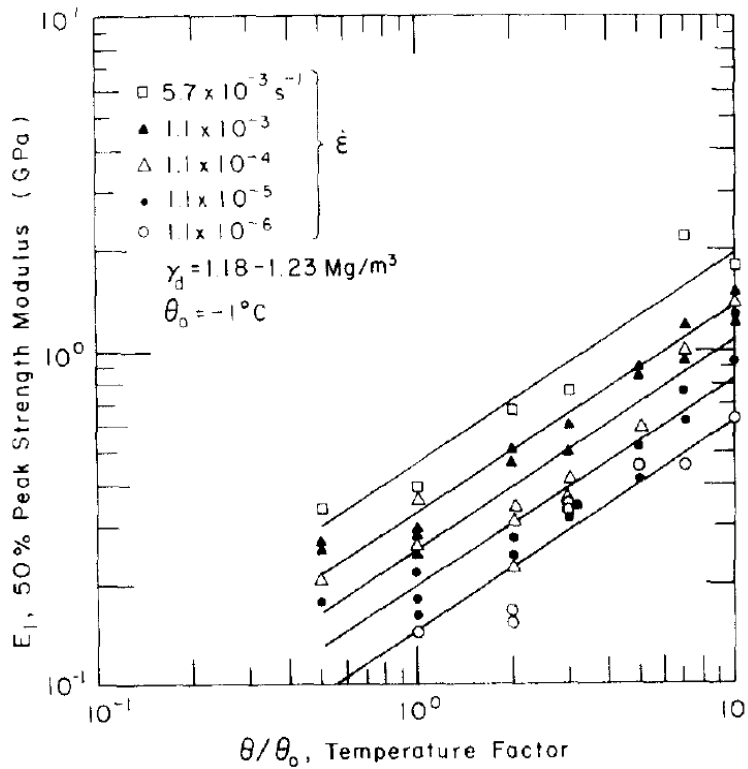
Figure 4.3. Plot of $\log \sigma_m$ vs. $\log (\theta / \theta_0)$ for different strain rates (Zhu and Carbee 1984).

- **Young's Modulus (E) vs. Temperature (T):** The results for the initial tangent modulus and tangent modulus at 50% peak strength vs. temperature, under various strain rates, are depicted in Figure 4.4. According to Figure 4.4(a), initial tangent modulus is only dependent on temperature, while the 50% strength modulus (Fig. 4.4b) varies with both temperature and strain rate. Zhu and Carbee (1984) concluded that a strain rate of about $1.1\text{E-}3/\text{sec}$ could be considered as a critical strain rate characterising the moderate transition between the brittle and ductile failure modes for the frozen silt. In addition, for high dry densities, the frictional resistance between soil particles normally at large strains account for a major part of the peak strength. On the other hand, at lower dry densities (i.e. moving towards the ice-rich condition), the strength is mainly controlled by the ice matrix experiencing failure at small strains about 1% soon after plastic yielding has occurred.

The values of mechanical parameters are later (in Chapter 5) presented in a table and used for the slope stability analysis.



(a)



(b)

Figure 4.4. (a) Initial tangent modulus vs. temperature and (b) tangent modulus at 50% strength vs. temperature (Zhu and Carbee 1984).

●●● *Yugui et al. (2016)*

Triaxial compressive tests were conducted on frozen silt, applying different confining pressures ($\sigma_3 = 1, 3, 5$ MPa) and temperatures ($T = -2, -4, -6, -8$ °C), under the shear strain rate of $1.67E-4$ /sec (in the moderate range). The silt soil was of low plasticity (plastic limit = 15% and liquid limit = 23.2%) and high dry density ($\rho_d = 1850$ kg/m³). The deviatoric stress vs. axial strain curves were obtained.

- **Cohesion (c) vs. Temperature (T):** According to the deviatoric stress vs. axial strain curves ($\sigma_1 - \sigma_3$ vs. ε_1 curves), considering large axial strains of about $\varepsilon_1 \approx 15\%$ as the failure strains, and also the linear Mohr-Coulomb (MC) strength criterion: $\sigma_1 - \sigma_3 = (\sigma_1 + \sigma_3) \cdot \sin\phi + 2.c.\cos\phi$, after solving the MC equation for different confining pressures applied to the samples, the cohesion values at $T = -2, -4, -6$ and -8 °C are calculated to be $c = 0.825$ MPa, 1.18 MPa, 1.73 MPa and 1.43 MPa respectively.

- **Friction angle (ϕ) vs. Temperature (T):** As a result of solving the MC equation, the friction angles at $T = -2, -4, -6$ and -8 °C are determined to be $\phi = 25.9^\circ, 25.56^\circ, 25.75^\circ$ and 31.16° respectively.

- **Young's Modulus (E) vs. Temperature (T):** Amongst the deviatoric stress vs. axial strain curves ($\sigma_1 - \sigma_3$ vs. ε_1 curves), the ones corresponding to the lowest confining pressure ($\sigma_3 = 1$ MPa) are used to determine the secant modulus (at 50% peak strength). At $T = -2, -4, -6$ and -8 °C, the secant moduli at 50% peak strength are $E_{50\%} = 181.8, 310.4, 373.44,$ and 471.1 MPa respectively.

The values of the abovementioned parameters are presented in the table below.

Table 4.7. Mechanical parameters of frozen silt according to Yugui et al. (2016).

Mechanical parameters	Parameter values at different temperatures			
	-2°C	-4°C	-6°C	-8°C
Cohesion c (MPa)	0.825	1.18	1.73	1.43
Friction angle ϕ (°)	25.9	25.56	25.75	31.16
Young's modulus $E_{50\%}$ (MPa)	181.8	310.4	373.44	471.1

4.3 Sand soils

●●● *Sayles (1974)*

Triaxial compression tests were conducted on saturated frozen Ottawa sand, at the temperature of $T = -3.89$ °C, under different strain rates such as $6.67E-5$ /sec and $3.33E-4$ /sec (in the moderate range), and $5E-4$ /sec (in the moderate-to-high range). The applied hydrostatic confining pressures were in the range of $\sigma_3 = 0.34 - 8.2$ MPa. The Ottawa sand samples had an average dry unit weight of $\gamma_d = 16.4$ kN/m³, a void ratio of $e = 0.59$, and a specific gravity of $G_s = 2.65$. Samples were saturated with distilled, de-aired water, and then frozen from the top down. No expansion was observed during the freezing process, which was attributed to the fact that the volume increase because of the water-to-ice phase change was absorbed in the free water supply connected to the bottom of specimen. The results included axial stress-strain curves at different confining pressures, their respective Mohr circles and envelopes, and also the plots representing the combined effect of applied strain rate and confining pressure on the first (or cohesion) peak strength.

- **Cohesion (c) vs. Temperature (T):** Considering the Mohr envelopes at different strain rates, for low confining pressures, cohesion (the intercept of the Mohr envelope) becomes $c = 1.8 - 2$ MPa. Using another approach, based on the Mohr-Coulomb strength criterion: $\sigma_1 = \sigma_3 \cdot \tan^2(45 + \phi/2) + 2 \cdot c \cdot \tan(45 + \phi/2)$, with friction angle approximated to be $\phi = 31^\circ$, cohesion is calculated to be

$c = [\sigma_1 - \sigma_3 \cdot \tan^2(45+31/2)] / (2 \cdot \tan(45+31/2))$. Here, the σ_1 and σ_3 parameters are the compressive strength at failure strain and the confining pressure respectively.

- **Friction angle (ϕ) vs. Temperature (T):** According to the results at $T = -3.89$ °C, under the medium range of strain rates and low-to-medium confining pressures, the friction angle is determined/approximated as $\phi \approx 31^\circ$.

- **Young's Modulus (E) vs. Temperature (T):** At $T = -3.89$ °C, under low-to-medium applied confining pressures and moderate strain rates, tangent modulus at 50% peak strength is determined to be $E_{50\%} \approx 1.5$ GPa.

The abovementioned parameters are presented in the table below as well.

Table 4.8. Mechanical parameters of frozen Ottawa sand according to Sayles (1974).

Mechanical parameters	Definition/Formulae/Value
	$T = -3.89 \text{ } ^\circ\text{C}$
Cohesion c (MPa)	$1.8 - 2 ; (\sigma_1 - 3.124.\sigma_3) / 3.535$
Friction angle φ ($^\circ$)	31
Young's modulus $E_{50\%}$ (MPa)	1500

●●● **Parameswaran (1980)**

A series of uniaxial unconfined compression tests were performed on frozen saturated Ottawa sand, at temperatures between -2 and -15 $^\circ\text{C}$, under constant axial strain rates varying between 10^{-7} and 10^{-2} /sec. Ottawa sand specimens, when compacted, had an optimum dry density of $\rho_d = 1700 \text{ kg/m}^3$. Each sample was connected to a vacuum pump to remove the air, and then it was saturated with de-aired distilled water. Next, the cylindrical specimens were frozen in a cold room at -6 $^\circ\text{C}$, where the water expelled during freezing was removed from the bottom of the sample. The final test samples had a total moisture content of about $w\% = 20\%$.

- **Cohesion (c) vs. Temperature (T):** The plots for the variation of compressive strength (i.e. maximum stress) with temperature and different strain rates are presented in Figure 4.5. Using the Mohr-Coulomb strength criterion, cohesion becomes $c = \sigma_1 / (2.\tan(45+\varphi/2))$, where σ_1 is the compressive strength shown in Figure 4.5. Appropriate values for φ at negative temperatures are needed in order to calculate c values at different negative temperatures.

- **Young's Modulus (E) vs. Temperature (T):** Values of initial tangent modulus E_i as a function of temperature and different strain rates can be obtained from the respective plots shown in Figure 4.6. $E_{50\%}$ (neither the Secant nor the Tangent moduli at 50% strength) was not measured by Parameswaran (1980). Normally, $E_{50\%}$ has smaller values than E_i .

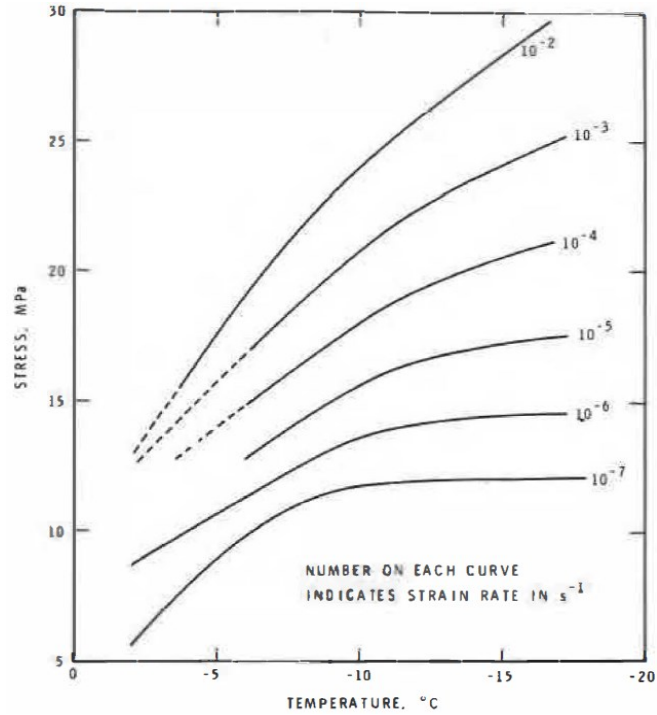


Figure 4.5. Variation of compressive strength σ_1 as a function of temperature (Parameswaran 1980).

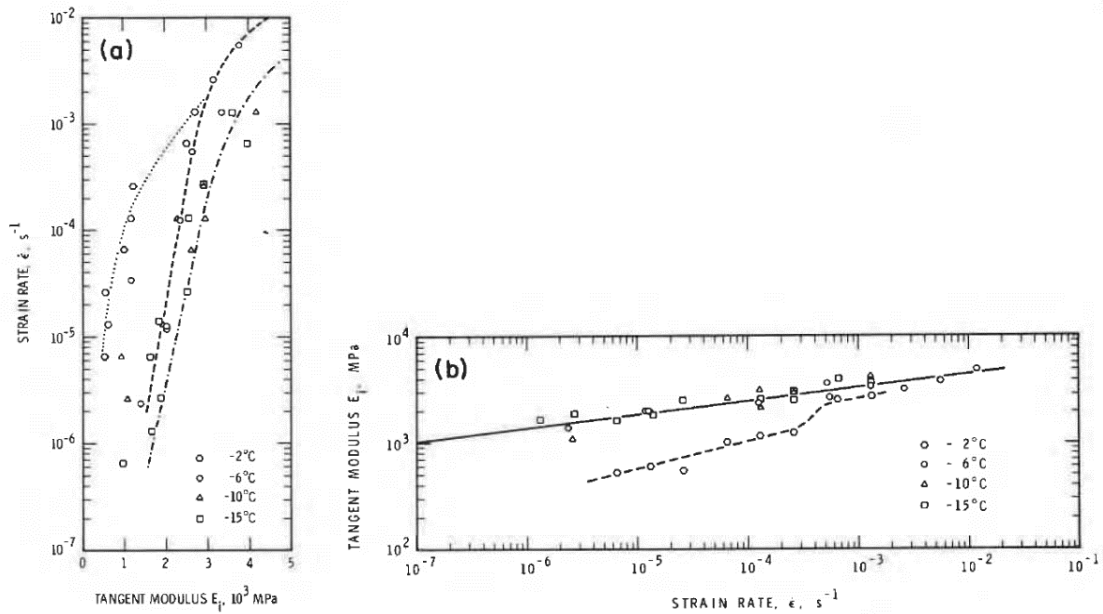


Figure 4.6. Variation of initial tangent modulus E_t : (a) with \log (strain rate); and (b) with strain rate (log-log scale) (Parameswaran 1980).

Slightly modified values of mechanical parameters (based on the study by Parameswaran (1980)) are determined and presented in Chapter 5 for the slope stability analysis.

●●● *Nater et al. (2008)*

In their study, other related publications were mentioned and referred to as well, such as *Arenson (2002)*, *Arenson et al. (2004)*, *Arenson and Springman (2005a, 2005b)*. In these studies, the main focus was on ice-rich permafrost, i.e. ice-rich frozen soils from rock glaciers in the Swiss Alps, at negative temperatures near 0 °C. A series of triaxial compression tests were performed on undisturbed permafrost soil samples, with controlled temperature and volumetric ice content. The authors pointed out that the stress-strain curve of a frozen soil would be generally characterized by an initial yield due to pore ice failure at approximately 1% axial strain, and then strain hardening up to a second peak, followed by strain softening. In addition, the two main components of a frozen soil which influence the shear strength of the whole material include the pore ice (influencing the cohesive part) and the density of solid particles which controls the frictional resistance. Furthermore, the shear strength of alpine permafrost soils is expressed in terms of internal friction angle and cohesion utilizing a Mohr-Coulomb (MC) failure criterion as for many other soils. It is pointed out that large strains have significant influence on the strength of frozen geo-materials and therefore efforts should be made to establish in situ strain states when analysing the stability of frozen slopes. Accordingly, different formulae were proposed for the cohesion and friction angle of frozen soil.

- **Cohesion (c) vs. Temperature (T):** The value of cohesion c rises with increasing the volumetric ice content w_i and decreasing the temperature T . The volumetric ice content is defined as the volume of pore ice (V_i) divided by the total volume of frozen soil (V_{total}), i.e. $w_i = V_i / V_{\text{total}}$. The proposed relationship by Nater et al. (2008) is as follows:

$$C_{(T=-2.1^\circ\text{C})} = 534.93\text{kPa} \bullet w_i^{1.91} \quad (\text{Eq. 4.1})$$

$$C = - C_{(T=-2.1^\circ\text{C})} / 2.1 \bullet T \quad (\text{Eq. 4.2})$$

where $C_{(T=-2.1^\circ\text{C})}$ is cohesion at the reference temperature.

- **Friction angle (ϕ) vs. Temperature (T):** With increasing the volumetric ice content w_i the effective angle of internal friction ϕ' decreases from $\phi' = \phi'_{\text{initial}}$ to $\phi' = 0$. The proposed formula by Nater et al. (2008) is as follows:

$$\phi' = \phi'_{\text{initial}} - \phi'_{\text{initial}} \bullet w_i^{2.6} \quad (\text{Eq. 4.3})$$

where ϕ'_{initial} is considered to be the effective angle of friction at above 0°C, i.e. for the unfrozen condition.

The proposed approach by Nater et al. (2008) will be further used in Chapter 5 to modify the values of strength parameters, from different studies on frozen sand soils, to reach/obtain more appropriate parameters for frozen slope analyses.

●●● **Yang et al. (2010a)**

A series of triaxial compression tests on frozen sand was conducted, at $T = -6$ °C, under the strain rate of 1.67E-4/sec (in the moderate range) and confining pressures varying from 0 to 14 MPa. It is pointed out that the strength of frozen sand was affected by water content and confining pressure. The dry density and water content of test samples were $\rho_d = 1810$ kg/m³ and $w\% = 15\%$ respectively. The linear Mohr-Coulomb (MC) strength envelope is practicable and effective when confining pressures are of low-to-medium values and/or within a small range. However, when dealing with a wide range of confining pressures, from small to large values, linear MC criterion is not suitable. A non-linear Mohr-Coulomb criterion was proposed by Yang et al. (2010a) in order to describe the strength characteristics of frozen sand under high confining pressures.

- **Cohesion (c) vs. Temperature (T):** Based on the proposed non-linear MC criterion, the generalized cohesion c for the frozen sand at $T = -6$ °C, as a function of confining pressure σ_3 , is expressed as follows (where atmospheric pressure is $P_a = 101.325$ kPa):

$$c = [2.822 \cdot 10^{-5} (\sigma_3 / P_a)^3 - 8.45 \cdot 10^{-3} (\sigma_3 / P_a)^2 + 0.969 (\sigma_3 / P_a) + 6.604] \cdot P_a \quad (\text{Eq. 4.4})$$

- **Friction angle (φ) vs. Temperature (T):** Based on the proposed non-linear MC criterion, the generalized internal friction angle φ for the frozen sand at $T = -6$ °C, as a function of confining pressure σ_3 , is expressed as follows (with $P_a = 101.325$ kPa):

$$\varphi = [-1.085*10^{-7}(\sigma_3 / P_a)^4 + 4.8826*10^{-6}(\sigma_3 / P_a)^3 + 5.26*10^{-3}(\sigma_3 / P_a)^2 - 0.7744 (\sigma_3 / P_a) + 28.784] \quad (\text{Eq. 4.5})$$

- **Young's Modulus (E) vs. Temperature (T):** A hyperbolic stress-strain model was proposed to describe the shear deformation of frozen sand, both the strain softening behavior during shearing under low confining pressures and strain hardening behavior under high confining pressure. The model parameters were determined from the triaxial test results. Based on the hyperbolic model, two strength moduli were defined: E_0 the strength modulus at the initial axial strain of the non-linear stage of the stress-strain curve (ε_0) and its corresponding shear stress (σ_0), and E_i the initial tangent modulus at the minor strain of the non-linear stage of the stress-strain curve. The formulae for E_0 and E_i , for the frozen sand at $T = -6$ °C, as functions of confining pressure σ_3 , are expressed as follows (with $P_a = 101.325$ kPa):

$$E_0 = [1.704*10^{-4}(\sigma_3 / P_a)^3 + 0.113 (\sigma_3 / P_a)^2 - 14.411 (\sigma_3 / P_a) + 3462.538] * P_a \quad (\text{Eq. 4.6})$$

$$E_i = [1.14*10^{-3}(\sigma_3 / P_a)^3 - 0.253 (\sigma_3 / P_a)^2 + 16.098 (\sigma_3 / P_a) + 594.758] * P_a \quad (\text{Eq. 4.7})$$

●●● **Yang et al. (2010b)**

Triaxial compression tests were conducted on frozen sand from Qinghai-Tibet railway construction site at $T = -4$ °C, under the constant strain rate of $1.67E-4$ /sec (in the moderate range) and a wide range of confining pressures σ_3 from 0 to 18 MPa. The dry density and water content of test samples were about $\rho_d = 1850$ kg/m³ and $w\% = 15\%$. It is noted by the authors that the frozen sand showed strain softening behavior under low confining pressures. But with increasing the confining pressure, the strain softening phenomenon decreased and even a strain hardening behavior was developed under high confining pressures. A new strength criterion was proposed for the failure mechanism of frozen sand under general stress state, also considering the pressure melting and crushing phenomena under high confining pressures. All the

parameters of the failure criterion were determined using the results from triaxial compression tests.

- **Cohesion (c) vs. Temperature (T):** Considering the stress-strain curves and the linear Mohr-Coulomb (MC) strength criterion: $\sigma_1 - \sigma_3 = (\sigma_1 + \sigma_3) \cdot \sin\varphi + 2 \cdot c \cdot \cos\varphi$, for the two lowest confining pressures (in the low-to-medium range), i.e. $\sigma_3 = 0.5$ and 1.0 MPa, and large axial strains $\varepsilon = 15 - 20\%$ as failure strains, cohesion is calculated to be $c = 0.77$ MPa.

- **Friction angle (φ) vs. Temperature (T):** Similar to the above-mentioned procedure, considering the linear MC criterion: $\sigma_1 - \sigma_3 = (\sigma_1 + \sigma_3) \cdot \sin\varphi + 2 \cdot c \cdot \cos\varphi$, with the two lowest confining pressures $\sigma_3 = 0.5$ and 1.0 MPa, and large axial strains $\varepsilon = 15 - 20\%$ as failure strains, friction angle is calculated to be $\varphi \approx 32^\circ$.

- **Young's Modulus (E) vs. Temperature (T):** Considering the stress-strain curve, for the lowest confining pressure $\sigma_3 = 0.5$ MPa, secant modulus (at 50% peak strength) is determined to be $E_{50\%} = 129$ MPa.

Table 4.9. Mechanical parameters of frozen sand from Qinghai-Tibet according to Yang et al. (2010b).

Mechanical parameters	Calculated values
	$T = -4^\circ\text{C}$
Cohesion c (MPa)	0.77
Friction angle φ ($^\circ$)	32
Young's modulus $E_{50\%}$ (MPa)	129

5 Results of slope stability analysis based on finite element modeling

In this chapter, results of the finite element stability analysis on frozen soil slopes are presented and discussed. As explained in section 3.3, the mechanical parameters required for the current MATLAB code incorporating the FEM include the specific weight γ , the Young's modulus E , the Poisson's ratio ν , the internal friction angle ϕ , and the cohesion c . As a benchmark for the results of our study, first, the slope analysis is performed for an unfrozen soil slope, with the following material properties:

Table 5.1. Mechanical parameters for the unfrozen soil slope material.

Mechanical Parameters	Specific weight γ (kN/m ³)	Young's modulus E (MPa)	Poisson's ratio ν	Cohesion c (kPa)	Friction angle ϕ (°)
	20	20	0.49	50	20

The geometry of the slope under investigation is represented in Fig. 3.14a, and the respective mesh-generated domain for the finite element problem is shown in the figure below (numbers are in meters).

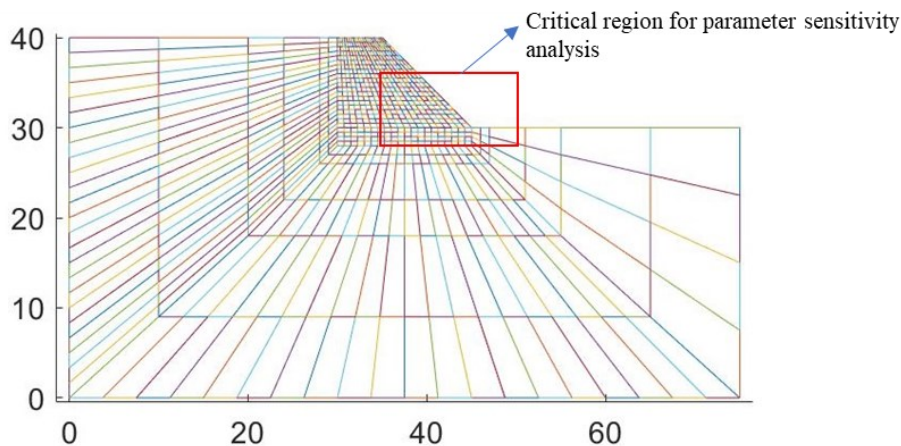
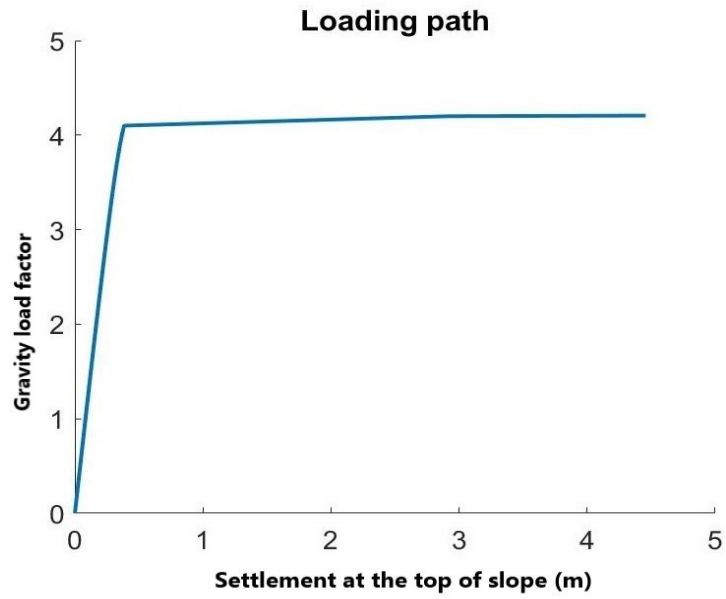
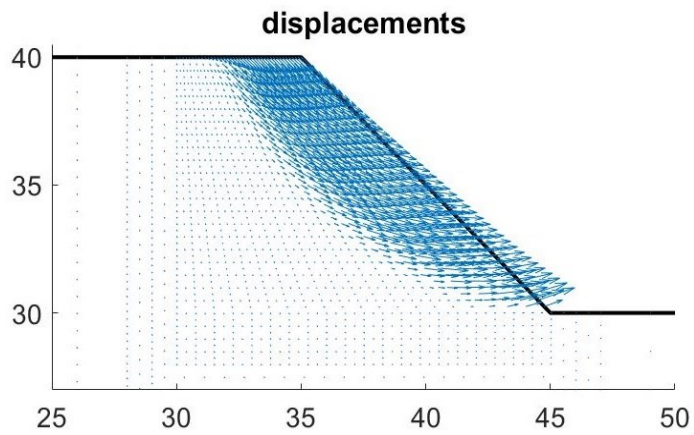


Fig. 5.1. Finite element mesh-generated model with quadrilateral elements refined close to and within the slope's body, comprising 768 eight-pointed quadrilateral elements with 2405 nodal points.

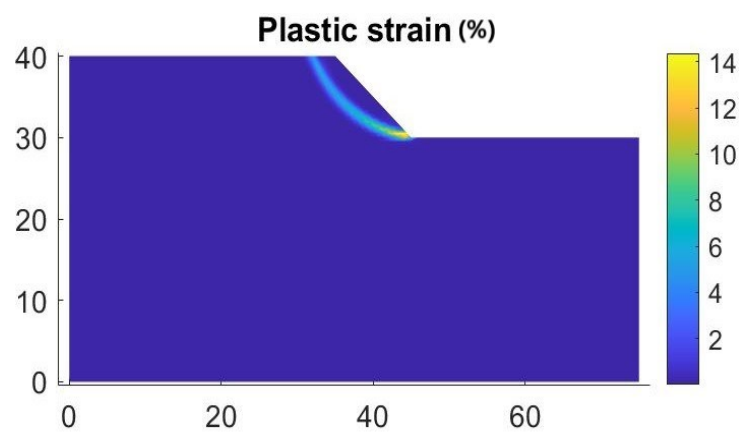
As explained in Chapter 3, the current MATLAB code incorporates FEM in which the associative (elastic-perfectly plastic at small strains) Drucker-Prager (DP) criterion employs the above-mentioned mechanical parameters. The stability analysis considers the self weight of the body. The self weight is increased incrementally (from zero to a critical value) until the total settlement on top of slope (point *A* in Fig. 3.14a) reaches a pre-defined value, here 3m, which corresponds to the “collapse” of the slope. At the end of analysis, the accumulated gravity load factor ζ (introduced in Section 3.3 of Chapter 3) defines the slope’s factor of safety (FOS) against failure. In Figure 5.2, the results of the stability analysis for the unfrozen soil slope are presented. According to Figure 5.2(a) and numerical results from the MATLAB code, the factor of safety (FOS) of slope against failure is ≈ 4.2 . This is also verified by Sysala et al. (2016) and (Chapter 8 of the book by de Souza Neto et al. (2008)). As the load factor ζ increases from 4 to 4.1 and 4.2 ($\delta\zeta = 0.1$), the settlement on top of slope increases from 0.367 m to 0.385 to 2.918 m, and finally to 4.45 m (which is past the pre-defined maximum settlement), indicating the occurrence of collapse of the slope. In Figure 5.2(b), the displacement pattern of slope material is illustrated. As the load factor ζ increases, the settlement obviously increases as well and at the same time the slope material tends to move outside the slope’s initial geometry, leading to a (seemingly rotational) failure. Accordingly, the largest displacements occur in the close vicinity of the slope, which is indicative of the occurrence of slope failure (or collapse). Furthermore, in Figure 5.2(c), plastic strain values (in %) are depicted throughout the entire domain (=FE model), where they have the highest values along a thin curved zone. This zone acts as the slope’s slip line/surface (critical shear zone), and mainly contributes to the above-mentioned failure/collapse of slope.



(a)



(b)



(c)

Fig. 5.2. (a) Loading path: Gravity load factor vs. settlement on top of slope, (b) Displacement pattern of slope at failure, (c) Plastic strain throughout the domain.

Different studies have focused on mechanical properties of frozen soils, as several of them are already mentioned and briefly reviewed in Chapters 2 and 4. Here, our main goal is to collect the respective data from some of these studies, determine reasonable values for the above-mentioned mechanical properties at below zero temperatures, and use them within our MATLAB code to perform stability analyses for frozen soil slopes. It should be noted that we only focus on the parameter analysis of the critical region of a slope where strain localization tends to happen. We are not conducting FEM modeling on the temperature variations along the buried depth. The obtained results will only be used to investigate the sensitivity of strain localization development at shear regions to the applied frozen temperatures.

5.1 Clay soils

●●● Based on the proposed approach by *Akhtar and Li (2020)*, the mechanical properties of frozen Hong Kong marine clay deposit (mixture of clay, silt, and fine sand) are determined at negative temperatures, and used for the slope stability analysis:

Table 5.2. Mechanical parameters based on the approach by Akhtar and Li (2020).

Parameters $T (^{\circ}C)$	Specific weight γ (kN/m ³)	Young's modulus E (MPa) = $2.676 (-T)^{1.324}$	Poisson's ratio ν = $0.413 (-T)^{-0.177}$	Cohesion c (kPa) = $125 (-T)^{1.065} / (2 \cdot \tan(45 + \phi/2))$	Friction angle ϕ ($^{\circ}$)
-0.5	16.68	1.069	0.467	17.95	28
-1	16.68	2.676	0.413	37.55	28
-2	16.68	6.7	0.365	78.57	28
-3	16.68	11.46	0.34	121	28
-4	16.68	16.773	0.323	164.38	28
-5	16.68	22.54	0.311	208.48	28

Akhtar and Li (2020) proposed that temperature had little effect on the friction angle of frozen clay soils. In their study, the peak friction angle for the frozen Hong Kong marine clay under investigation is reported as ϕ_{\max} (peak friction angle) =

28°. Here, this value is considered for the stability analysis at different below zero temperatures (Table 5.2).

The slope stability analyses are performed at different negative temperatures, considering the mechanical parameters in Table 5.2. However, none of the analyses resulted in slope failure/collapse. The dominant mode of displacement for slope material was downward movement, i.e. settlement, without developing any slip line (=critical shear zone). As a representative for all the analyses, the plots for the analysis results corresponding to $T = -3\text{ }^{\circ}\text{C}$ are illustrated in Figure 5.3. As clear from Figure 5.3(a), the settlement on top of slope increased linearly with increasing the load factor, until it reached and passed the maximum pre-defined settlement, i.e. 3m, and that's when the analysis stopped. The plot for the displacement pattern of slope material, Figure 5.3(b), also shows that there was no failure of the slope, and just occurred the excessive settlement, and also the largest total displacement did not occur in the close vicinity of slope (as this is the case when the slope failure occurs), and instead, it was widely distributed over an area extending to the upper and left boundaries of the model/domain. In addition, according to the plot for plastic strain (Fig. 5.3(c)), throughout the entire domain, plastic straining was negligible, and no slip surface/line developed as a result. This can be mainly attributed to the low value of Young's modulus, in combination with comparatively high values of friction angle and cohesion. This resulted in slope material experiencing incremental settlements under incremental load factors (Fig. 5.3(a)), i.e. small load factors causing small displacements until the total settlement on top of slope reached the maximum pre-defined value, (where in case of slope failure, normally at some point during the analysis, under a few subsequent load increments large settlements would take place and the analysis would end soon after that).

It is worth mentioning that according to Table 5.2, the frozen soil under investigation develops more strength as the temperature decreases, i.e. the values of Young's modulus E and cohesion c have increased and the Poisson's ratio ν has decreased as the temperature changed from -0.5 to -5°C .

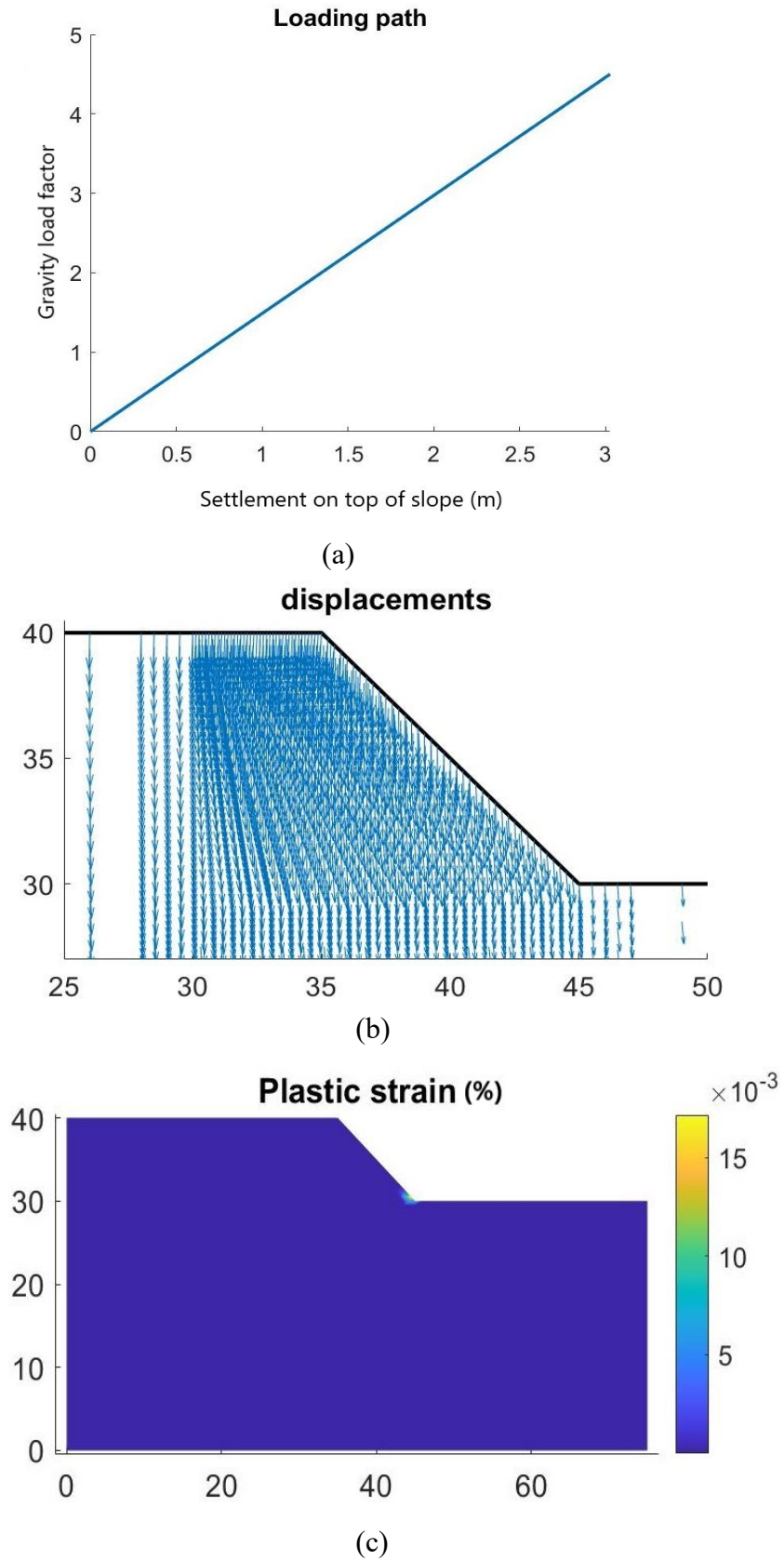


Fig. 5.3. $T = -3^{\circ}\text{C}$: (a) Loading path: Gravity load factor vs. settlement on top of slope, (b) Displacement pattern of slope, (c) Plastic strain throughout the domain.

●●● According to the studies by *Li et al. (2015b)* and *Bai et al. (2020)*, mechanical properties of an experimental frozen clay are determined at negative temperatures, and used for the slope stability analysis:

Table 5.3. Mechanical parameters for an experimental frozen clay according to Li et al. (2015) and Bai et al. (2020).

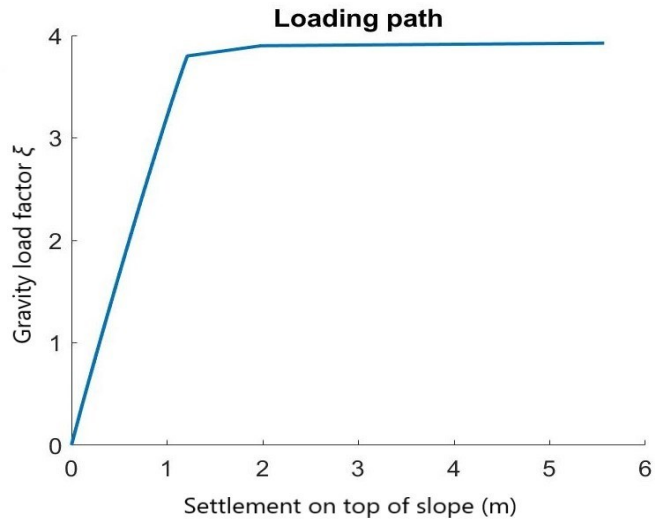
Parameters $T (^{\circ}C)$	Specific weight γ (kN/m ³)	Young's modulus E (MPa) = $22.5 + 11.3 (-T)^{0.6}$	Poisson's ratio ν = $0.28 - 0.007 (-T)$	Cohesion c (kPa) = $20 + 6 (-T)^{1.24}$	Friction angle ϕ ($^{\circ}$) = $20 + 3.4 (-T)^{0.38}$
-0.5	20	29.955	0.2765	22.54	22.613
-1	20	33.8	0.273	26	23.4
-2	20	39.63	0.266	34.172	24.42
-3	20	44.345	0.259	43.43	25.16
-4	20	48.461	0.252	53.474	25.76
-5	20	52.18	0.245	64.144	26.27
-6	20	55.611	0.238	75.3425	26.72
-7	20	58.82	0.231	87	27.12
-8	20	61.85	0.224	99.065	27.493

The soil under investigation was taken from the field of the Beiyin Canal (with the liquid limit and plastic limit of 50.9% and 26.4% respectively, dry density of 1550 kg/m³, and porosity of 0.46). Considering the specific gravity as $G_s = 2.70$, the specific weight γ is calculated to be 20 kN/m³ and presented in Table 5.3. According to Table 5.3, as already expected, with decreasing the temperature the Young's modulus, cohesion, and friction angle increase, while the Poisson's ratio decreases. Although, the increase in friction angle is very small compared to the one in Young's modulus and cohesion. This is somehow in agreement with the aforementioned proposition of Akhtar and Li (2020). The frozen slope stability analyses are performed considering the parameters in Table 5.3. All the stability analyses corresponding to $T = -0.5, -1, -2, -3, -4, -5$, and -6 °C resulted in slope failure/collapse. However, at more negative temperatures, i.e. $T = -7$ and -8 °C, the slip surface could not develop completely, and the dominant mode of displacement for slope material was downward movement (i.e. settlement). In Figures 5.4 and 5.5, the analysis results

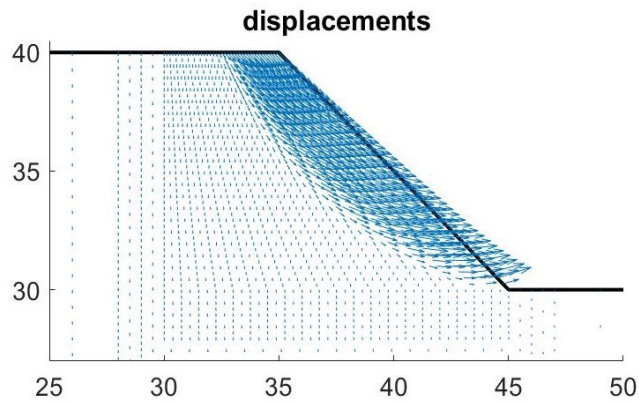
obtained for $T = -2$ and -4 °C are presented, as two examples for the slope analyses resulting in failure. According to Figure 5.4(a) and the numerical results from the MATLAB code, at -2 °C, as the load factor ξ increased incrementally, through the final steps of FE analysis, the settlement on top of slope increased as well from 1.13 to 1.17, 1.21, 1.98, and finally 5.569m, which clearly indicated the occurrence of collapse of the slope. The FOS against failure, i.e. the final accumulated value of load factor, is obtained to be ≈ 3.9 . The displacement pattern at collapse is depicted in Figure 5.4(b), vividly illustrating large displacements in the close vicinity of slope. In addition, according to Figure 5.4(d), the largest plastic strains occurred along a thin curved zone extending from somewhere at the top to the toe of slope, developing a critical slip line/surface (=critical shear zone). The failure obviously happened along this line. As for the analysis results at -4 °C (presented in Fig. 5.5), a similar argument applies, only with FOS ≈ 6.8 , which was because of the higher shear strength developed at -4 °C.

In Figure 5.6, the plots for the displacement pattern and the plastic strain at different temperatures of -2 , -3 , -4 , -5 , -6 and -8 °C are presented. As mentioned before, at $T = -2$, -3 , -4 , -5 and -6 °C, the slope collapse occurred, while at $T = -8$ °C slope failure did not happen (and only the excessive downward displacement of slope material continued until the settlement on top of slope reached and passed the maximum pre-defined value for the FE MATLAB code, i.e. 3m).

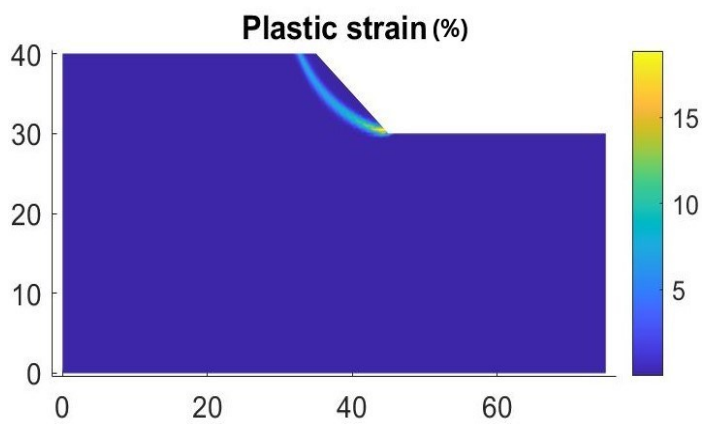
In case of slope failure, as explained before, the largest plastic strains occurred along a thin shear zone extending from the top to the toe of slope. This is obvious in Figures 5.6(b), (d), (f), (h), and (j), where it can also be confirmed that for different temperatures the plastic strains are of the same order of magnitude and within a narrow range. In addition, it can be observed that as the temperature decreases, the plastic strain values decrease as well (except for the case of $T = -6$ °C). Finally, at $T = -8$ °C, the plastic strains are about one order of magnitude smaller, the slip line has not developed completely (Figs. 5.6(k) and (l)), and the slope failure has not occurred.



(a)

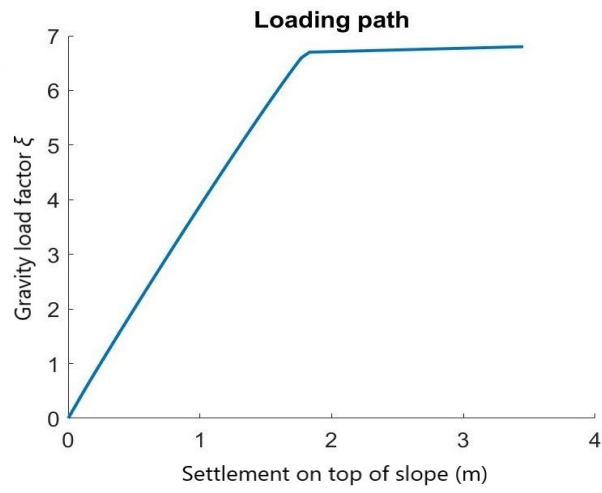


(b)

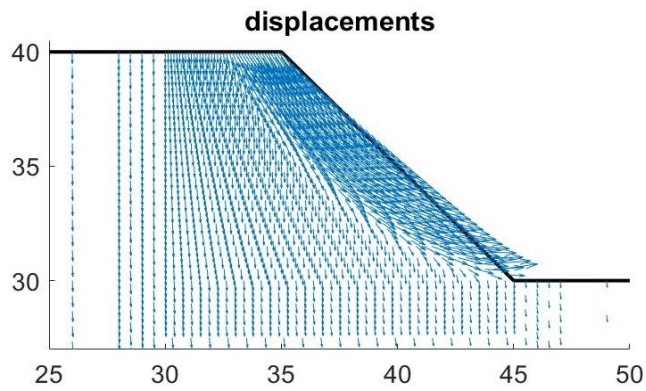


(c)

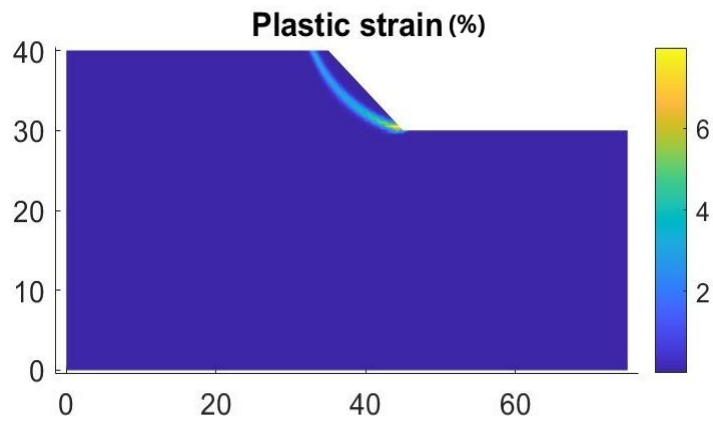
Fig. 5.4. $T = -2^\circ\text{C}$: (a) Loading path: Gravity load factor vs. settlement on top of slope, (b) Displacement pattern of slope at collapse, (c) Plastic strain throughout the domain.



(a)

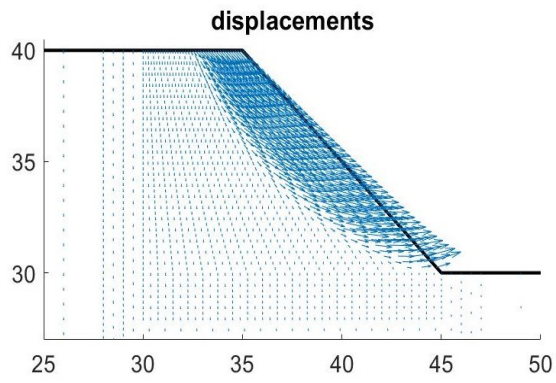


(b)

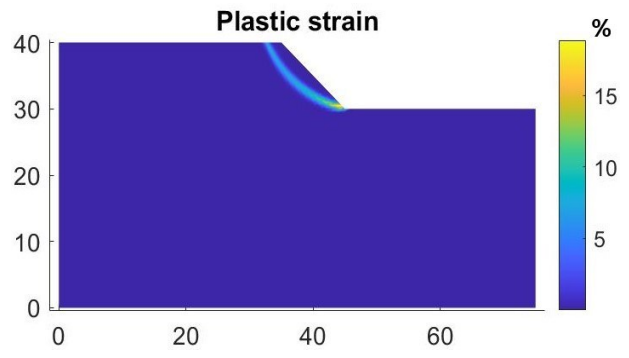


(c)

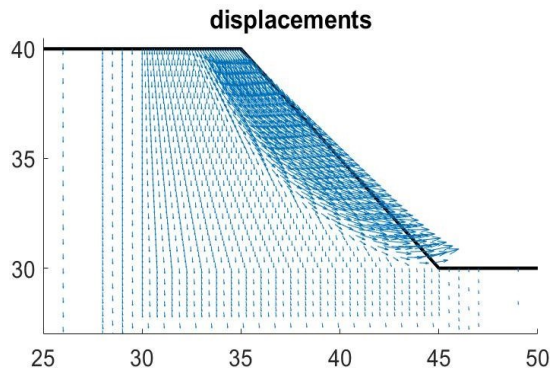
Fig. 5.5. $T = -4^{\circ}\text{C}$: (a) Loading path: Gravity load factor vs. settlement on top of slope, (b) Displacement pattern of slope at collapse, (c) Plastic strain throughout the domain.



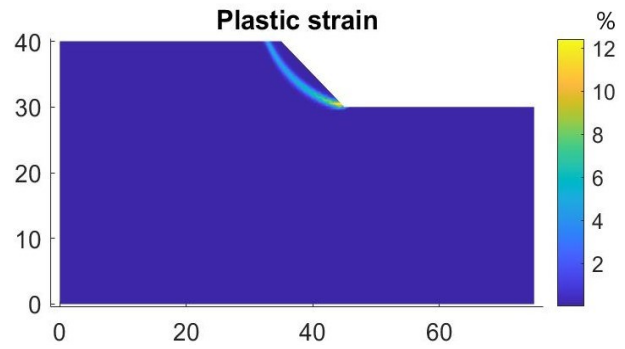
(a) Displacement pattern at $T = -2\text{ °C}$



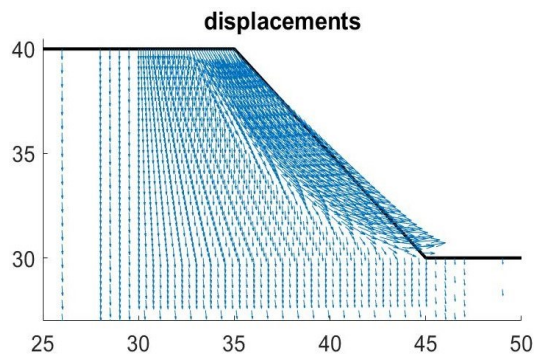
(b) Plastic strain distribution at $T = -2\text{ °C}$



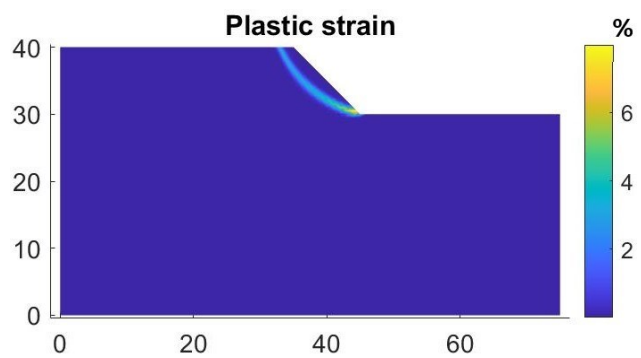
(c) Displacement pattern at $T = -3\text{ °C}$



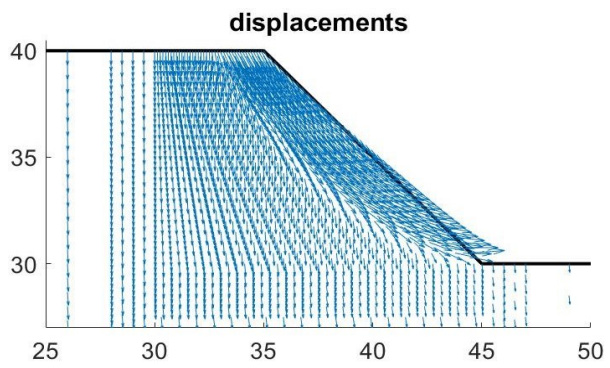
(d) Plastic strain distribution at $T = -3\text{ °C}$



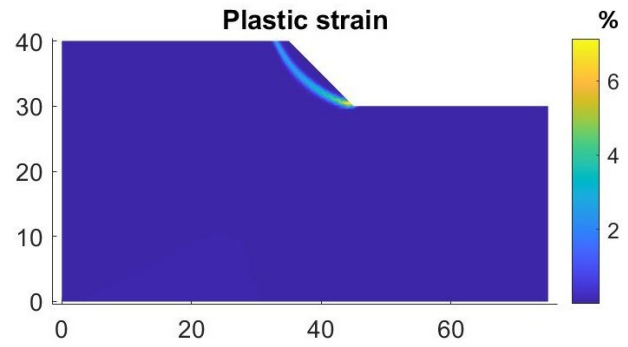
(e) Displacement pattern at $T = -4\text{ °C}$



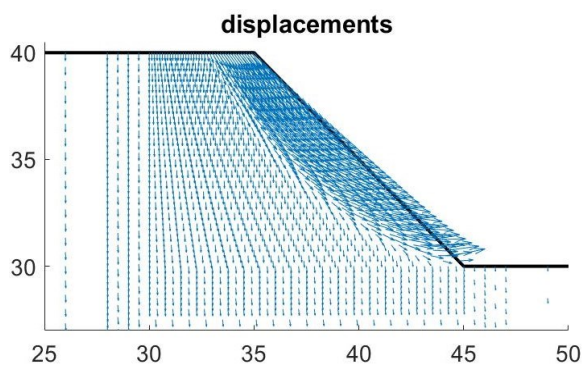
(f) Plastic strain distribution at $T = -4\text{ °C}$



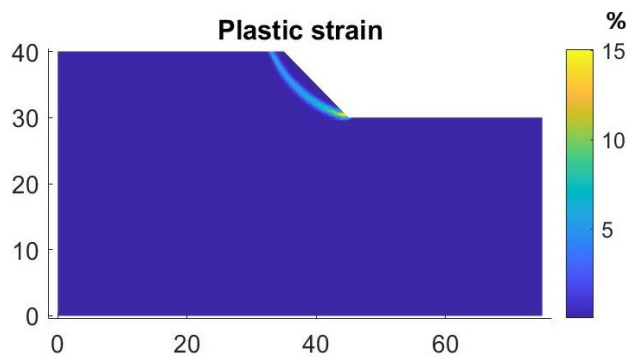
(g) Displacement pattern at $T = -5\text{ }^{\circ}\text{C}$



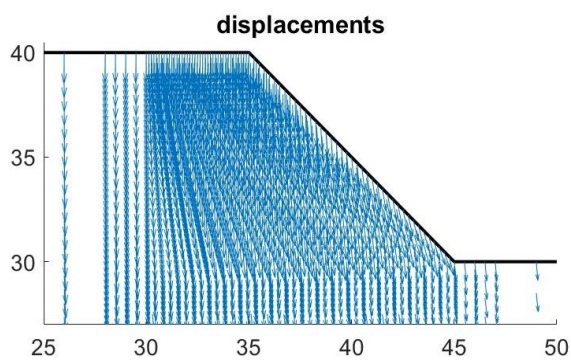
(h) Plastic strain distribution at $T = -5\text{ }^{\circ}\text{C}$



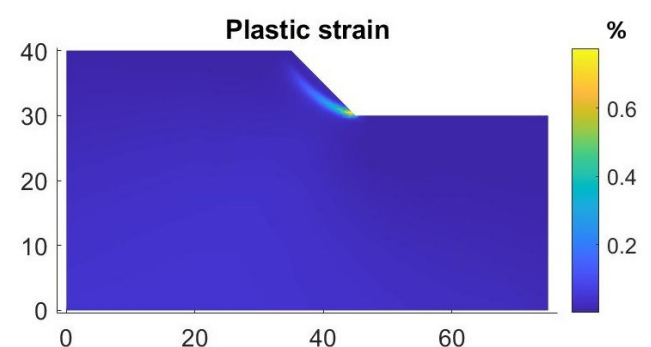
(i) Displacement pattern at $T = -6\text{ }^{\circ}\text{C}$



(j) Plastic strain distribution at $T = -6\text{ }^{\circ}\text{C}$



(k) Displacement pattern at $T = -8\text{ }^{\circ}\text{C}$



(l) Plastic strain distribution at $T = -8\text{ }^{\circ}\text{C}$

Fig. 5.6. Displacement pattern and Plastic strain plots at different negative temperatures.

As clear from the plots presented in Figures 5.4, 5.5, and 5.6, whenever slope failure has occurred, the thickness of the failure section along the slope (based on the dimensions shown on the plots) changes approximately within a range of 1 to 2.5m measured from the slope/ground surface. Within this range, the temperature is the most negative (the lowest) and can be considered to be almost constant. This was also shown in Figure 2.14 (from the study by Nater et al. (2008) and borehole measurements on the Muragl rock glacier during the Winter season). Also, regarding Figure 2.14, at depth of 10m (which is the depth of the toe of slope in our study), temperature is about -1 to -2 °C, still being close to the temperature measured near the ground surface. Accordingly, here the assumption of a constant negative temperature for the entire slope body seems to be acceptable. For the rest of our frozen slope analyses, this assumption will be considered as well.

●●● In another study, by *Girgis et al. (2020)*, strength and deformation parameters including the uniaxial unconfined compression strength σ_c , the Young's modulus E (determined by the tangent method at the point with 50% peak strength), and the Poisson's ratio ν (determined at the same stress that the Young's modulus is calculated) are determined for the artificial frozen sandy clay soils (Kaolinite-Sand and Bentonite-Sand). For the frozen Kaolinite-Sand (K-S) and the frozen Bentonite-Sand (B-S) samples, the values for the specific gravity parameter G_s are 2.65 and 2.63 respectively. In addition, the liquid limit and the plastic limit for the frozen K-S are 30% and 20%, and for the frozen B-S are 97% and 34%. According to the uniaxial compressive tests performed under the medium strain rate of 1.64E-4/sec, the mechanical parameters at negative temperatures are determined (presented in Tables 5.4 and 5.5) and used for the slope stability analyses:

Table 5.4. Mechanical parameters for the frozen Kaolinite-Sand according to the approach by Girgis et al. (2020).

Parameters $T (^{\circ}C)$	Specific weight γ (kN/m ³)	Young's modulus E (MPa) = $3.154 (-T)^{1.422} + 8.77$	Poisson's ratio ν = $-0.061 (-T)^{0.3} + 0.409$	Cohesion c (kPa) = $[197 (-T)^{1.093} + 192] / [2 \cdot \tan(45 + \phi/2)]$	Friction angle ϕ ($^{\circ}$) = $20 + 3.4 (-T)^{0.38}$
-0.5	17.27	9.95	0.359	94.796	22.613
-1	17.27	11.924	0.348	127.763	23.4
-2	17.27	17.221	0.334	197.2036	24.42
-3	17.27	23.813	0.324	268.834	25.16
-4	17.27	31.416	0.3165	341.651	25.76
-5	17.27	39.873	0.31	415.239	26.27

Table 5.5. Mechanical parameters for the frozen Bentonite-Sand according to the approach by Girgis et al. (2020).

Parameters $T (^{\circ}C)$	Specific weight γ (kN/m ³)	Young's modulus E (MPa) = $4.468 (-T)^{1.31} + 9.594$	Poisson's ratio ν = $-0.069 (-T)^{0.3} + 0.399$	Cohesion c (kPa) = $[206 (-T)^{1.11} + 307] / [2 \cdot \tan(45 + \phi/2)]$	Friction angle ϕ ($^{\circ}$) = $20 + 3.4 (-T)^{0.38}$
-0.5	15	11.396	0.343	134.163	22.613
-1	15	14.062	0.33	168.489	23.4

-2	15	20.672	0.314	242.11	24.42
-3	15	28.437	0.303	318.947	25.16
-4	15	37.061	0.294	397.62	25.76
-5	15	46.387	0.287	477.539	26.27

Here, the friction angles for these frozen sandy clay soils are calculated using the approach proposed by Li et al. (2015b) and Bai et al. (2020).

The slope stability analyses are performed at different temperatures, considering the mechanical parameters in Tables 5.4 and 5.5. However, none of the analyses resulted in slope failure/collapse. The dominant mode of displacement for the slope material was downward movement, i.e. settlement, without developing any slip line (=critical shear zone). As a representative for all the analyses, the analysis results corresponding to $T = -2$ °C for the frozen Kaolinite-Sand and Bentonite-Sand soils are illustrated in Figures 5.7 and 5.8. As clear from these figures, there is no failure of the slope, and just has occurred the excessive settlement. The argument and discussion presented earlier for the analysis results considering the frozen Hong Kong marine clay (from the study by Akhtar and Li 2020) apply here as well. The plastic strain values were negligible throughout the entire domain, and no slip surface/line has developed as a result (Figs. 5.7(b) and 5.8(b)). Again here, this can be attributed to the low values of Young's modulus, in combination with comparatively high values of friction angle and cohesion. The high values of cohesion and friction angle simply correspond to a high (shear) strength level for slope material, while the comparatively low values of Young's modulus imply the fact that, under incremental loading (load factor increment being $\delta\zeta = 0.1$ for instance), the slope material experience a wide range of elastic displacement/strain until they reach plastic yielding. This contributes to the insignificant plastic straining (shown in Figs. 5.7(b) and 5.8(b)). The only difference between the frozen K-S and the frozen B-S is that the frozen Bentonite-Sand has lower specific weight and higher strength values at the investigated negative temperatures. As a result, the FOS against excessive settlement (under self-weight) is obviously higher for the frozen Bentonite-Sand slope compared to the frozen Kaolinite-Sand slope.

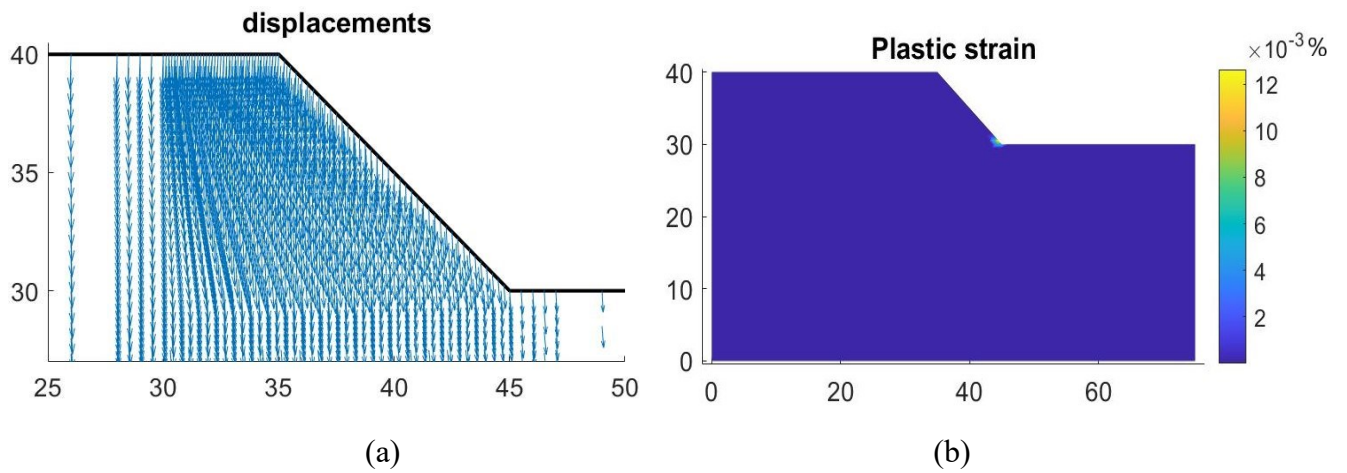


Fig. 5.7. Analysis results at $T= -2\text{ }^{\circ}\text{C}$ for the frozen Kaolinite-Sand: (a) Displacement pattern of slope material, (b) Plastic strain throughout the domain (values shown on the side bar are in percent %).

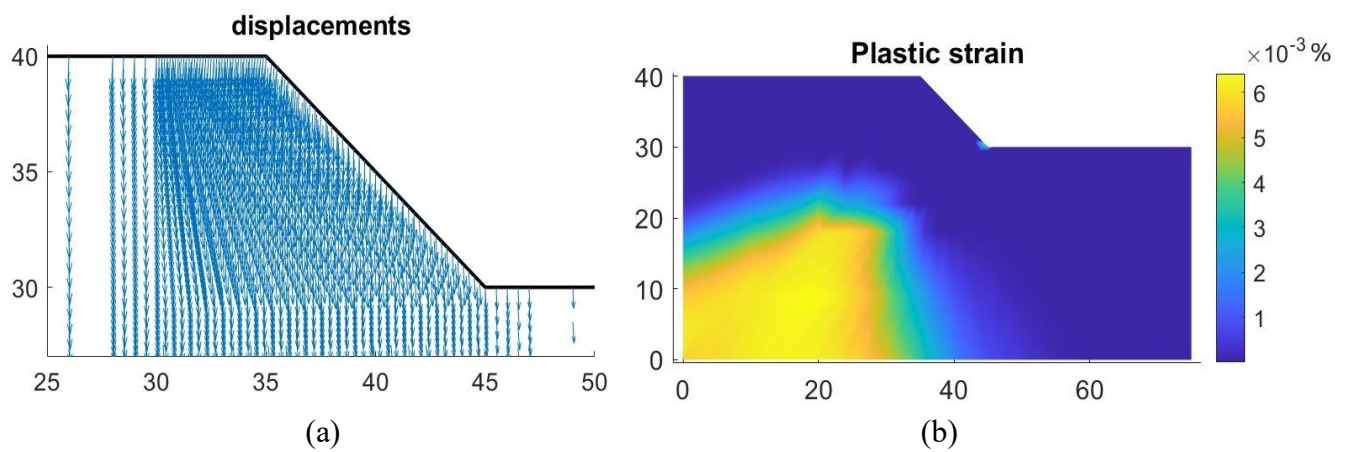


Fig. 5.8. Analysis results at $T= -2\text{ }^{\circ}\text{C}$ for the frozen Bentonite-Sand: (a) Displacement pattern of slope material, (b) Plastic strain throughout the domain (values shown on the side bar are in percent %).

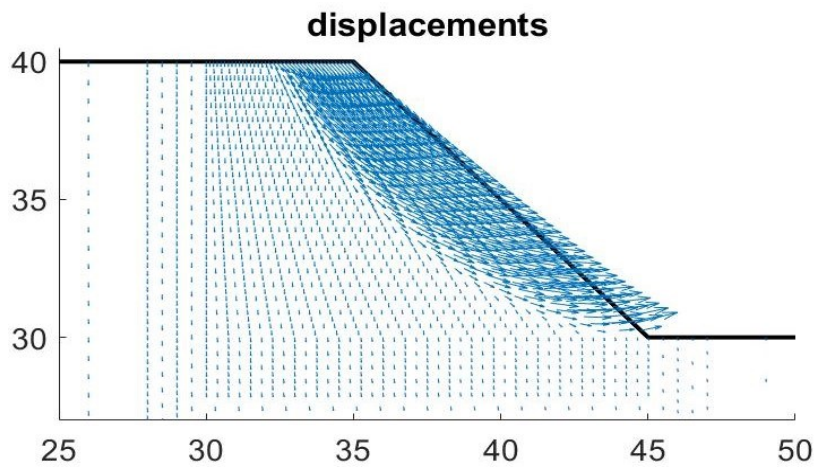
●●● *Li et al. (2019)* analyzed the freezing process and frost heave mechanism of a cold-region canal. They constructed a centrifuge model of a canal in a freezing environment, considering a frost-susceptible clay with the liquid limit $LL = 29.1\%$, plastic limit $PL = 15.2\%$, maximum dry density $\rho_{dmax} = 1890 \text{ kg/m}^3$ and void ratio $e = 0.4$. In their study, some formulae were proposed to calculate the mechanical parameters of frozen clay. Accordingly, these parameters are determined at negative temperatures and used for the slope stability analysis:

Table 5.6. Mechanical parameters for the frozen clay according to Li et al. (2019).

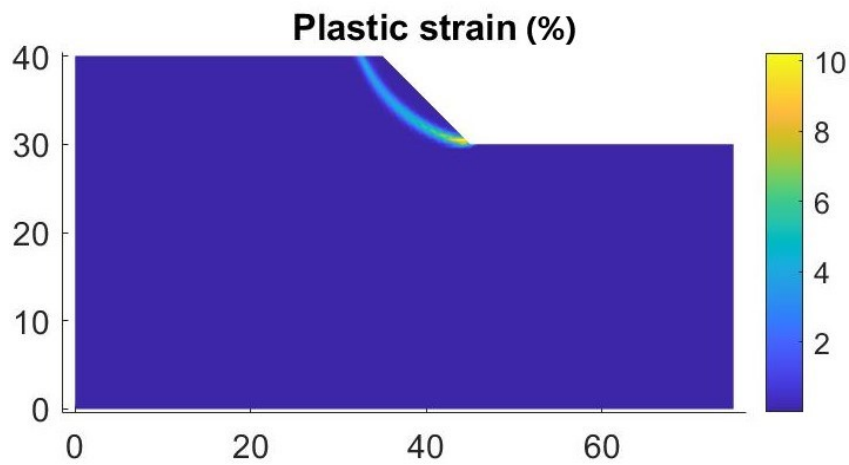
Parameters $T (^{\circ}C)$	Specific weight γ (kN/m^3)	Young's modulus E (MPa) = $75 [1 + 0.345 (T / -0.2)^{0.6}]$	Poisson's ratio $\nu =$ $0.28 [1 - 5E-3 (T / -0.2)]$	Cohesion c (kPa) = $10 [1 + 1.2 (T / -0.2)]$	Friction angle ϕ ($^{\circ}$) = $20 [1 + 6.41E-2 \times (T / -0.2)^{0.39}]$
-0.5	21.1	119.838	0.2765	40	21.83
-1	21.1	142.9614	0.273	70	22.4
-2	21.1	178.01	0.266	130	23.15
-3	21.1	206.382	0.259	190	23.69
-4	21.1	231.1343	0.252	250	24.124
-5	21.1	253.5025	0.245	310	24.5
-6	21.1	274.1375	0.238	370	24.83
-7	21.1	293.4345	0.231	430	25.13
-8	21.1	311.655	0.224	490	25.4
-9	21.1	328.985	0.217	550	25.66

According to Table 5.6, similar to the previous cases, with decreasing the temperature the Young's modulus, cohesion, and friction angle increase, while the Poisson's ratio decreases. Also, the increase in friction angle is small in comparison with the ones in Young's modulus and cohesion. In addition, between the Young's modulus and the cohesion, the increase in cohesion is more marked, i.e. the strength of frozen soil increases while the tangent to (=slope of) the initial/elastic portion of the stress-strain curve does not increase at that level. This implies that, at lower temperatures, under each load increment, the frozen slope material would experience a wider range of elastic displacements/strains until they reach plastic straining.

Slope stability analyses are performed using the mechanical parameters presented in Table 5.6. All the stability analyses corresponding to $T = -0.5, -1, -2, -3, -4, -5, -6,$ and $7\text{ }^{\circ}\text{C}$ resulted in slope failure/collapse. However, at lower temperatures, i.e. $T = -8$ and $-9\text{ }^{\circ}\text{C}$, the slip surface could not develop completely, and the dominant mode of displacement was the downward movement (i.e. settlement). According to the numerical results from the FE MATLAB code, at $T = -8$ and $-9\text{ }^{\circ}\text{C}$, the frozen slope experienced larger settlements (=higher number of settlement increments) under higher numbers of load factor increments without showing any sign of failure/collapse (until the maximum pre-defined settlement value was reached and the analysis ended). In Figure 5.9, the plots for the displacement pattern and plastic strain at different temperatures of $-2, -4, -6, -7, -8,$ and $-9\text{ }^{\circ}\text{C}$ are presented.

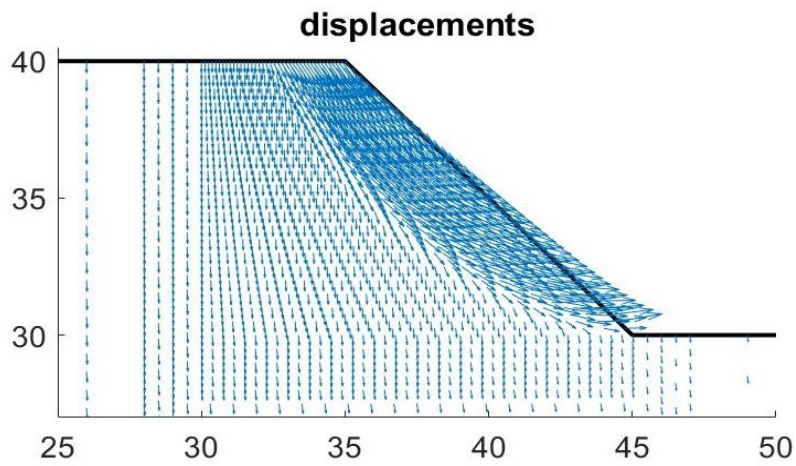


(a-1) Displacement pattern throughout the domain

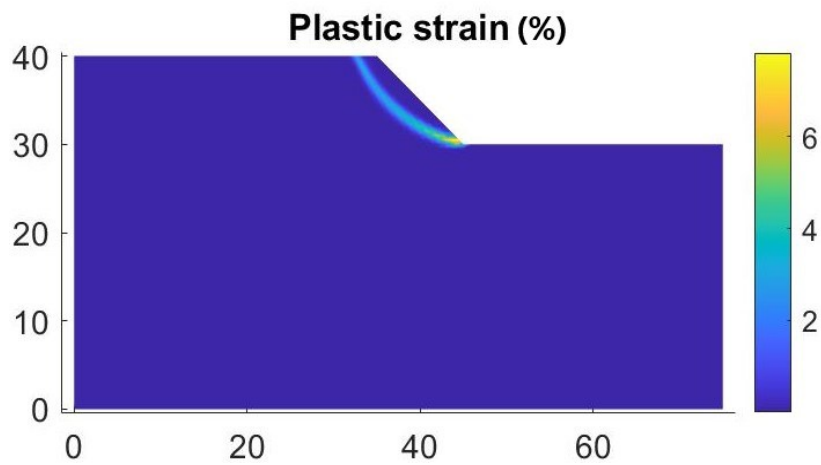


(a-2) Plastic strain throughout the domain/model

(a) Analysis results at $T = -2\text{ }^{\circ}\text{C}$

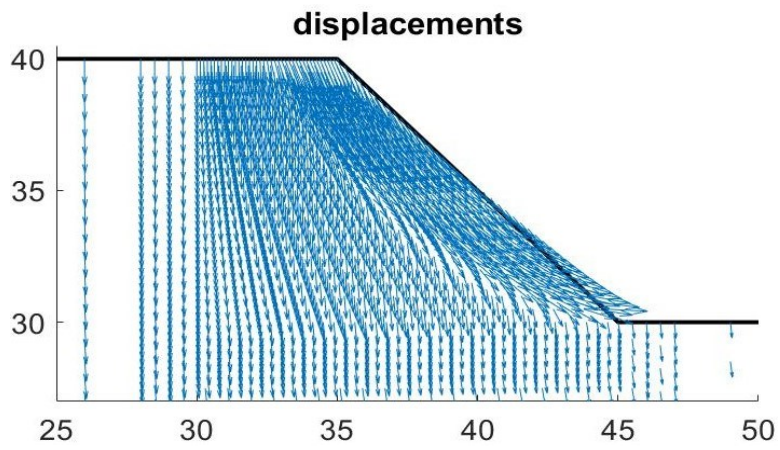


(b-1) Displacement pattern throughout the domain

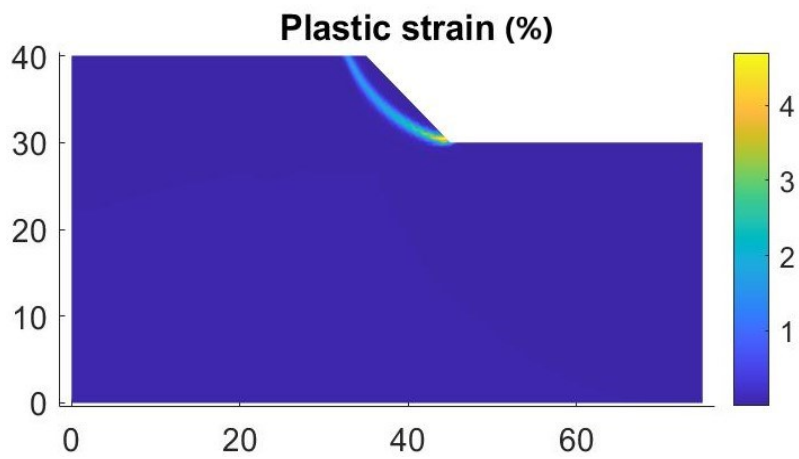


(b-2) Plastic strain throughout the domain/model

(b) Analysis results at $T = -4 \text{ }^\circ\text{C}$

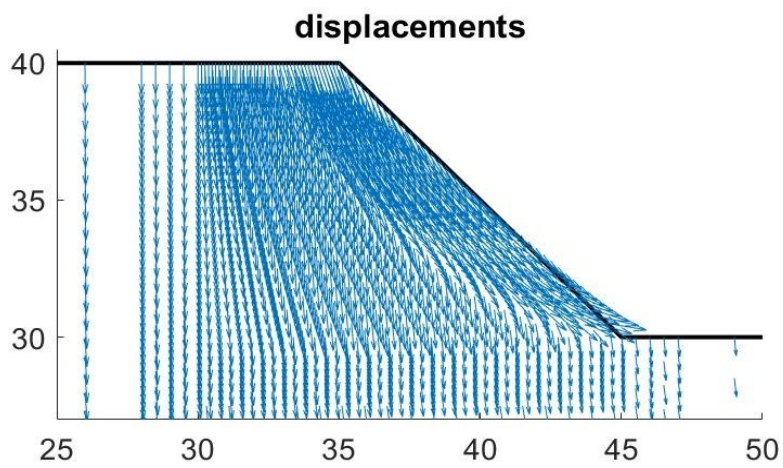


(c-1) Displacement pattern throughout the domain

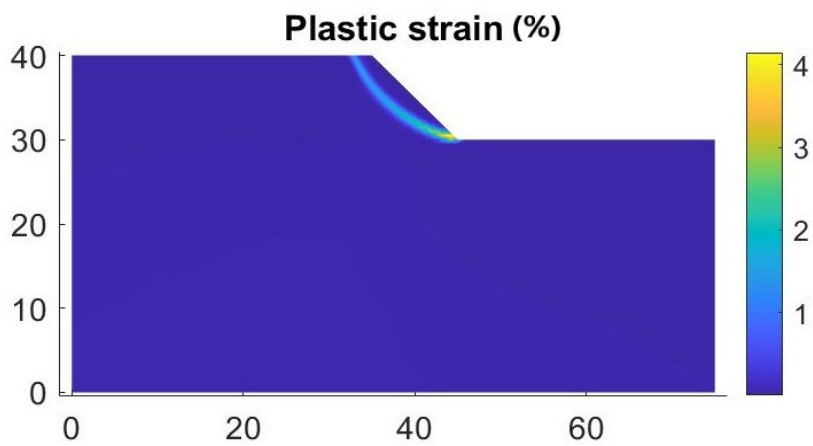


(c-2) Plastic strain throughout the domain/model

(c) Analysis results at $T = -6 \text{ }^\circ\text{C}$

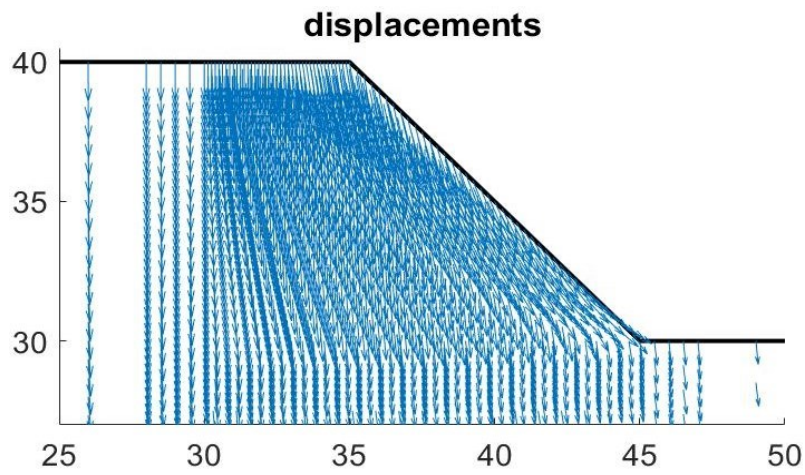


(d-1) Displacement pattern throughout the domain

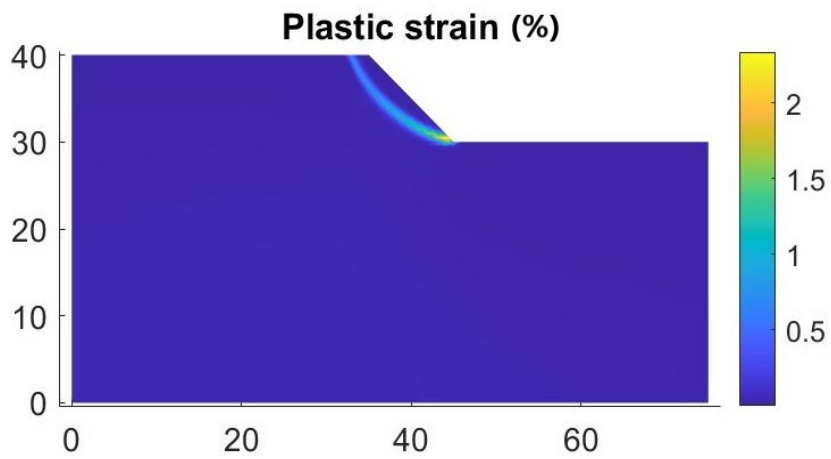


(d-2) Plastic strain throughout the domain/model

(d) Analysis results at $T = -7 \text{ }^\circ\text{C}$

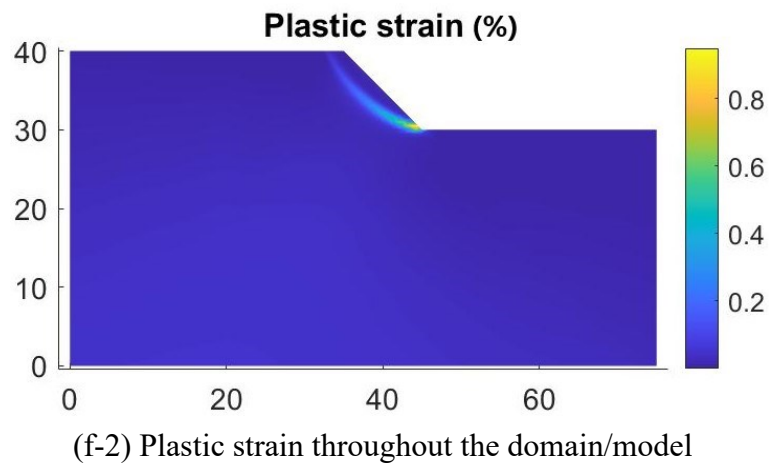
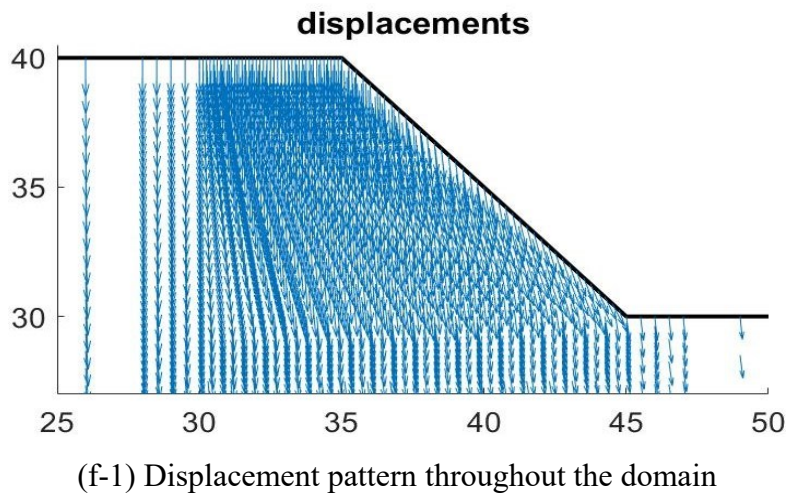


(e-1) Displacement pattern throughout the domain



(e-2) Plastic strain throughout the domain/model

(e) Analysis results at $T = -8 \text{ }^\circ\text{C}$



(f) Analysis results at $T = -9\text{ }^{\circ}\text{C}$

Fig. 5.9. Analysis results at (a) $T = -2\text{ }^{\circ}\text{C}$, (b) $T = -4\text{ }^{\circ}\text{C}$, (c) $T = -6\text{ }^{\circ}\text{C}$, (d) $T = -7\text{ }^{\circ}\text{C}$, (e) $T = -8\text{ }^{\circ}\text{C}$, and (f) $T = -9\text{ }^{\circ}\text{C}$.

It is clear from Figure 5.9 that at $T = -2, -4, -6$ and -7 °C the slope collapse has occurred, while at $T = -8$ and -9 °C slope failure did not happen and only the excessive downward displacement continued until the settlement on top of slope reached and passed the maximum pre-defined value of 3m.

In cases of slope failure, the plots for the displacement pattern (Figs. 5.9(a-1), (b-1), (c-1), and (d-1)) clearly depict the collapse of the slope, where the largest displacements have taken place in the close vicinity of slope, which is reasonable. Also, the largest plastic strains have occurred along a thin shear zone extending from the top to the toe of slope, developing a slip line within the slope. For different temperatures, the plastic strains are of the same order of magnitude and within a narrow range (Figs. 5.9(a-2), (b-2), (c-2), and (d-2)). In addition, it can be observed that as the temperature decreases, the plastic strains decrease as well.

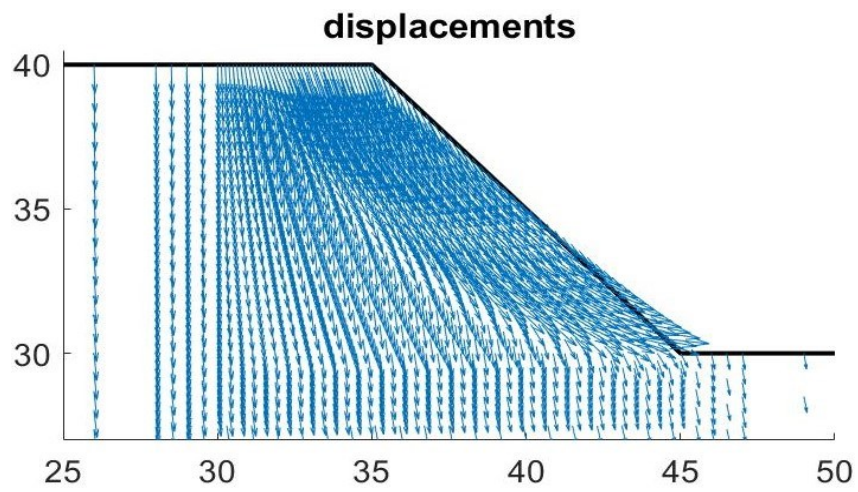
At $T = -8$ and -9 °C, on the other hand, the plots for the displacement patterns (Figs. 5.9(e-1) and (f-1)) do not represent slope failure, and the largest displacements did not occur in the vicinity of slope, instead, they are widely distributed over a zone extending to the upper and left boundaries of the model. Although, there is a sign of slightly developed slope failure at $T = -8$ °C, when compared to the results from higher temperatures, it is negligible and insignificant. As for the plastic strains, they are noticeably smaller than the ones from higher temperatures, and the slip lines has not developed completely (Figs. 5.9(e-2) and (f-2)). Even in the case of $T = -8$ °C where the slip line seems to be fully developed, the low values of plastic strain indicate why the slope failure/collapse could not occur.

●●● In the study by *Wang et al. (2017)*, triaxial compression tests (undrained shearing under a constant axial strain rate) were conducted on the reconstituted high plasticity frozen Kasaoka clay, with the specific gravity $G_s = 2.65$, and liquid limit (LL) and plastic limit (PL) of 62%, and 28% respectively. The confining pressure values for the tests were kept within the low-to-medium range (100-400 kPa), which fairly corresponds to temporary excavations, slope stability problems, near surface permafrost, etc. At such stress levels, mechanisms such as pressure melting and ice fracturing are not dominant. According to the results by Wang et al. (2017) at temperatures $T = -2, -5, \text{ and } -10$ °C, mechanical parameters are determined and used for the slope stability analysis:

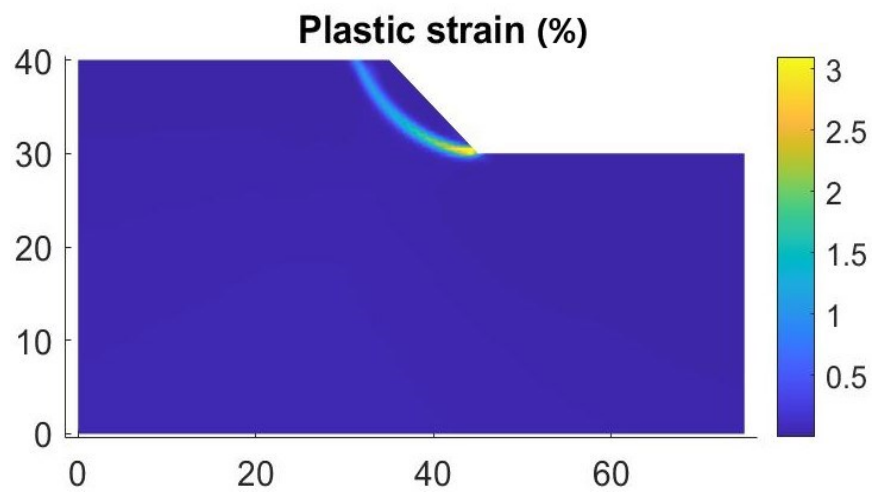
Table 5.7. Mechanical parameters for the frozen high plasticity Kasaoka clay.

Parameters T (°C)	Specific weight γ (kN/m ³)	Young's modulus E (MPa) =	Poisson's ratio $\nu =$ $0.28 - 0.007(-T)$	Cohesion c (kPa)	Friction angle ϕ (°)
-2	18	45	0.266	100	17
-5	18	184.5	0.245	280	18
-10	18	100	0.210	200	36

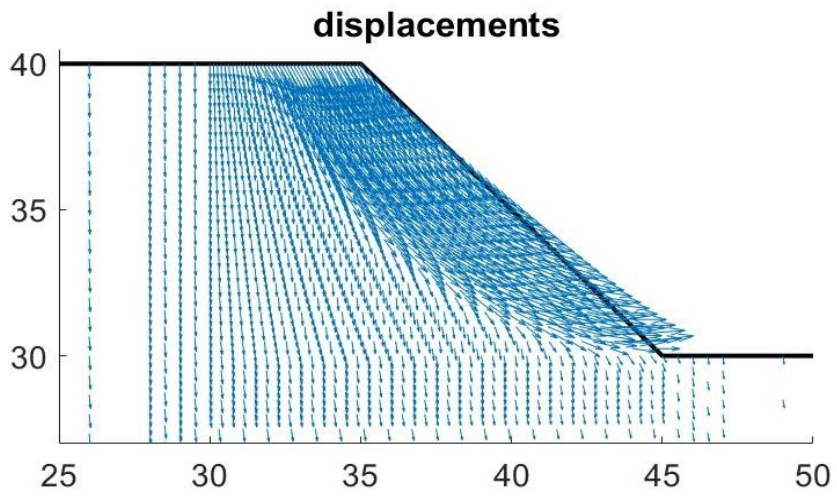
Here, the Poisson's ratio is calculated based on the formula proposed by Li et al. (2015b) and Bai et al. (2020). The analysis results namely the displacement pattern, total displacement, and plastic strain throughout the domain are presented in the following figure. As clear from Figure 5.10, at $T = -2$ and -5 °C slope failure has occurred, while at $T = -10$ °C slope failure did not happen (and just occurred the excessive settlement). All the arguments and discussions presented earlier for the cases with or without slope failure/collapse apply here as well. It is noteworthy that as the temperature decreased from -2 to -5 °C the plastic strains slightly increased, but the values were within a narrow range, and clearly in both cases the thin critical shear zones (curved slip lines/surfaces) were completely developed (Figs. 5.10(a-2) and (b-2)). At $T = -10$ °C, on the other hand, the plastic strain values obtained are about one order of magnitude smaller, and the slip line has not developed (Fig. 5.10(c-2)).



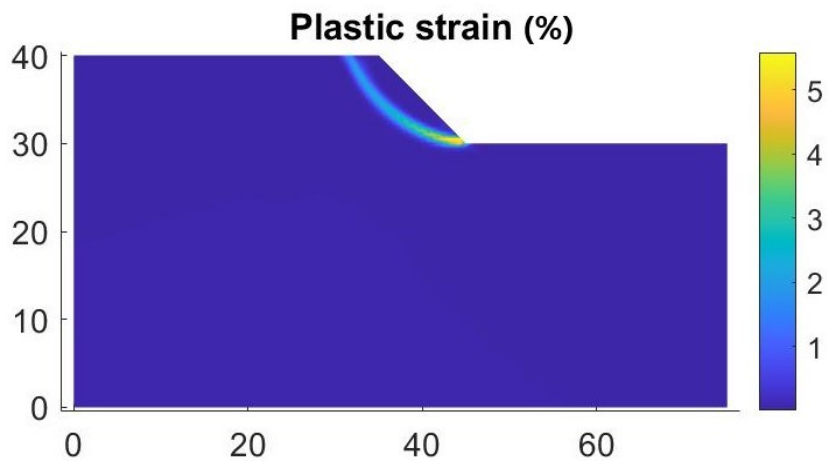
(a-1) Displacement pattern throughout the domain



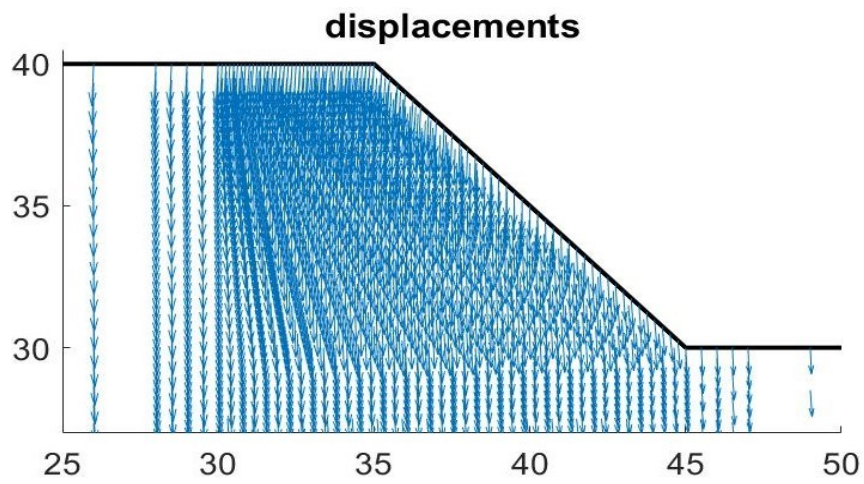
(a-2) Plastic strain throughout the domain



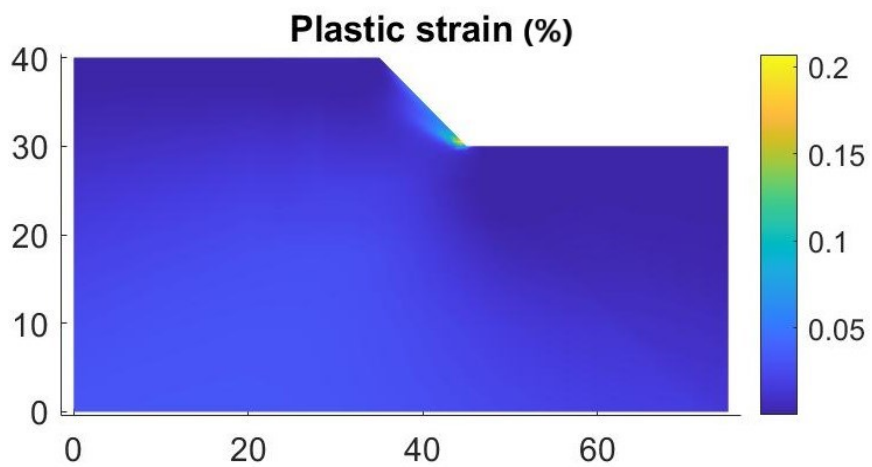
(b-1) Displacement pattern throughout the domain



(b-2) Plastic strain throughout the domain



(c-1) Displacement pattern throughout the domain



(c-2) Plastic strain throughout the domain

Fig. 5.10. Analysis results at (a) $T = -2\text{ }^{\circ}\text{C}$, (b) $T = -5\text{ }^{\circ}\text{C}$, and (c) $T = -10\text{ }^{\circ}\text{C}$.

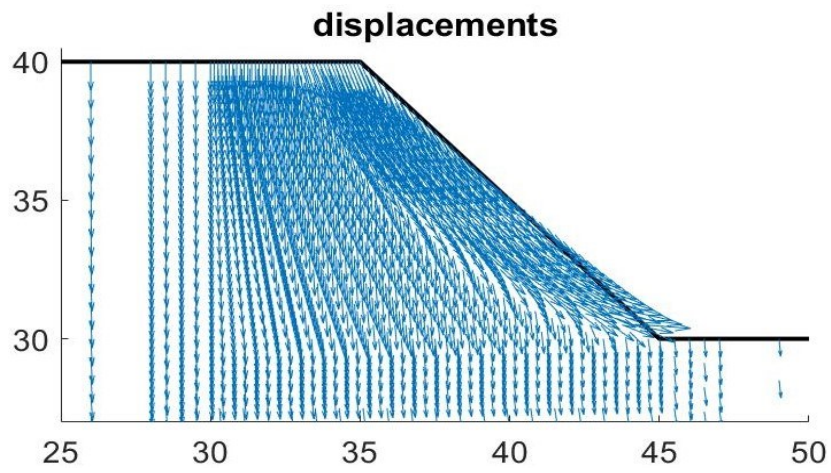
5.2 Silt soils

●●● According to the study by *Haynes and Karalius (1977)*, mechanical properties of frozen Fairbanks silt are determined and used for the slope stability analysis:

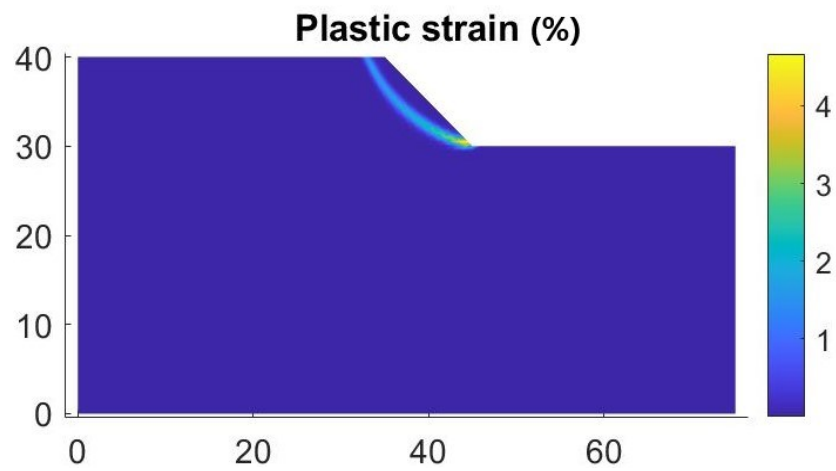
Table 5.8. Mechanical parameters of the frozen Fairbanks silt according to Haynes and Karalius (1977).

Parameters $T (^{\circ}C)$	Specific weight γ (kN/m ³)	Young's modulus E (MPa)	Poisson's ratio $\nu =$ $-0.061 (-T)^{0.3} + 0.409$	Cohesion c (kPa) = $[2150 - 330.T + 10.T^2] /$ $[2.\tan(45+\phi/2)]$	Friction angle ϕ ($^{\circ}$)
-2	18.1	516.730	0.334	890.44	26
-4	18.1	778.102	0.3165	1134.14	26
-6	18.1	1045.736	0.3046	1402.832	26
-8	18.1	1336.406	0.2952	1696.52	26

As clear from Table 5.8, strength parameters including Young's modulus E and cohesion c increase, while the Poisson's ratio ν decreases, as the temperature decreases. The assumption of a constant friction angle $\phi = 26^{\circ}$ seems to be reasonable for the frozen Fairbanks silt within the considered temperature range. As mentioned previously, in their tests, Haynes and Karalius (1977) employed high axial strain rates and a "relatively stiff" testing machine, which resulted in comparatively high values for the parameters E and c . The specific gravity of soil was $G_s = 2.71$, the dry density $\rho_d = 1.43 \text{ g/cm}^3$, the void ratio $e = 0.9$, and the moisture content $w = 29\%$ at saturation. The Fairbanks silt was classified as a fine-grained, low plasticity silt. For determining the Poisson's ratio values, the formula proposed by Girgis et al. (2020) for the frozen Kaolinite-Sand mixture is employed, because, similarly, the Fairbanks silt is fine-grained and has low plasticity. In Figure 5.11, the stability analysis results are presented. Accordingly, at different negative temperatures, slope failure has occurred. The plots for the displacement pattern confirm that the largest displacements take place in the close vicinity of slope. In addition, the plastic strain values are the highest along a thin curved shear zone, extending from the top to the toe of slope. Also, for different temperatures, plastic strains are within a very close range and of the same order of magnitude (Figs. 5.11 (a-2), (b-2), (c-2), and (d-2)).

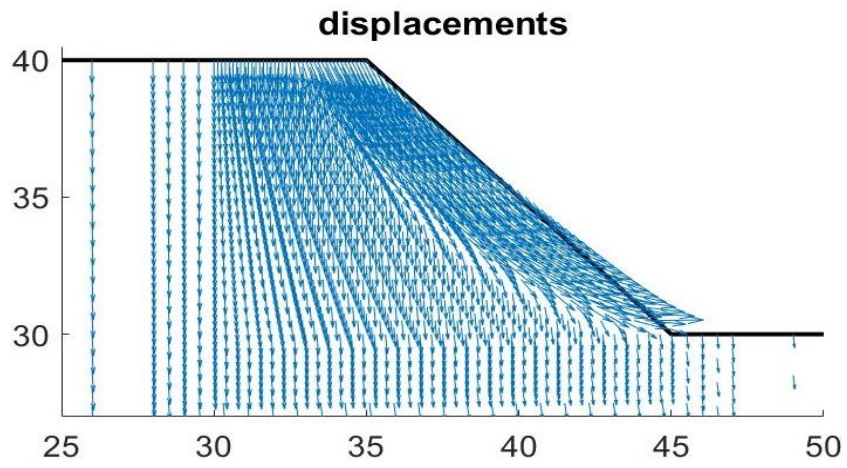


(a-1) Displacement pattern throughout the domain

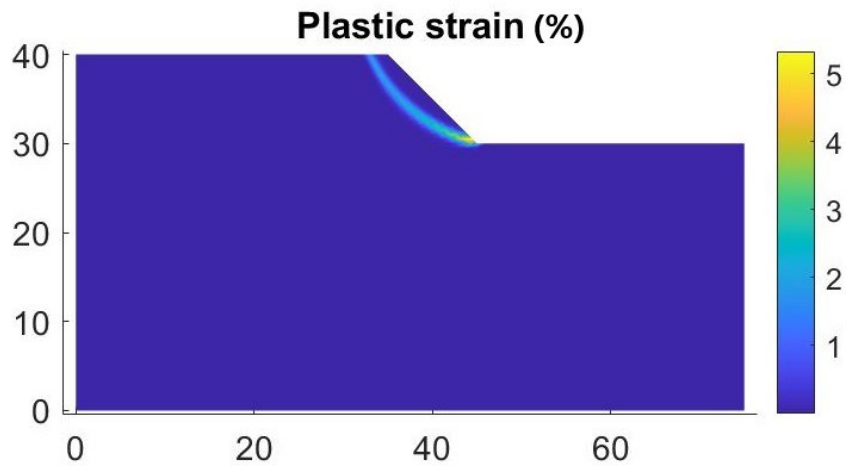


(a-2) Plastic strain throughout the domain

(a) Analysis results at $T = -2\text{ }^{\circ}\text{C}$

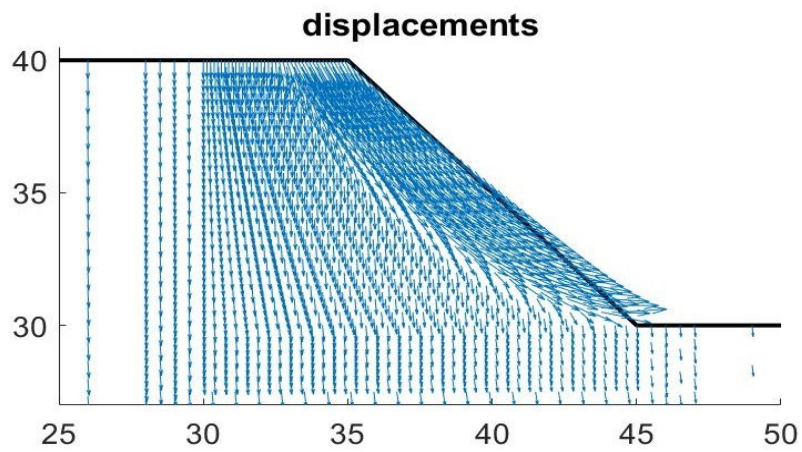


(b-1) Displacement pattern throughout the domain

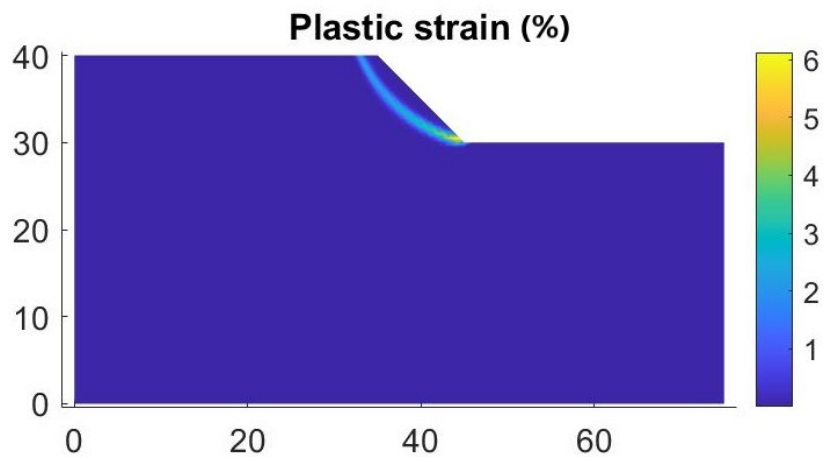


(b-2) Plastic strain throughout the domain

(b) Analysis results at $T = -4\text{ }^{\circ}\text{C}$

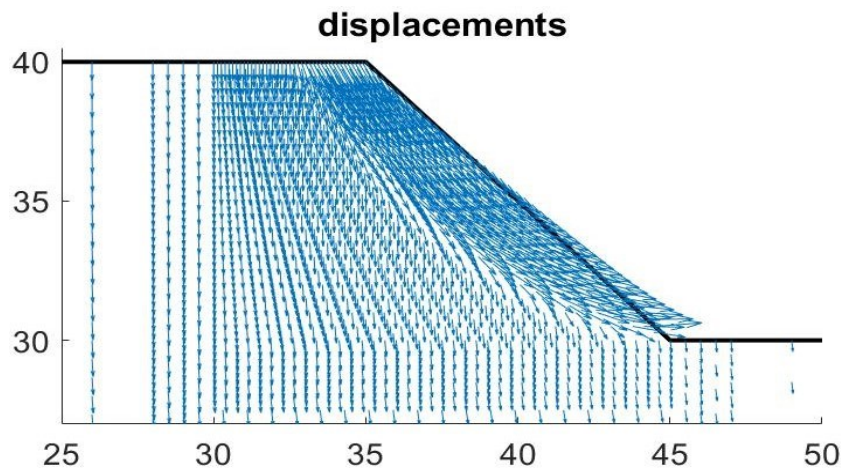


(c-1) Displacement pattern throughout the domain

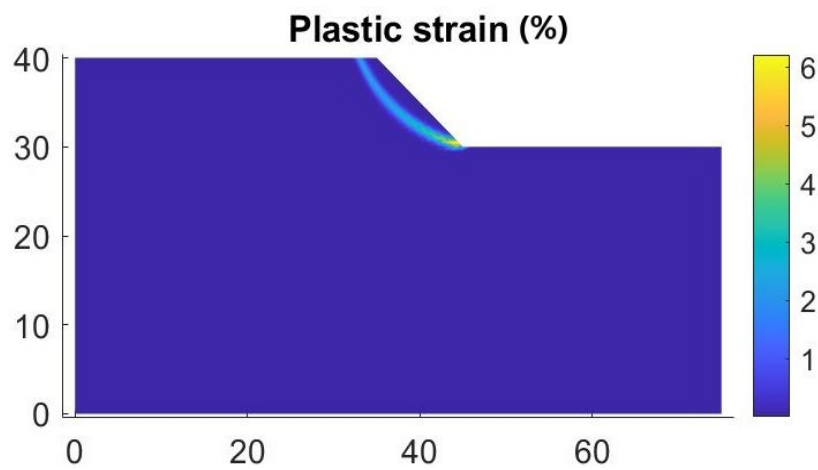


(c-2) Plastic strain throughout the domain

(c) Analysis results at $T = -6\text{ }^{\circ}\text{C}$



(d-1) Displacement pattern throughout the domain



(d-2) Plastic strain throughout the domain

(d) Analysis results at $T = -8^\circ\text{C}$

Fig. 5.11. Analysis results at (a) $T = -2^\circ\text{C}$, (b) $T = -4^\circ\text{C}$, (c) $T = -6^\circ\text{C}$, and (d) $T = -8^\circ\text{C}$.

●●● In another study, by *Zhu and Carbee (1984)*, uniaxial compressive strength tests were conducted on remolded, saturated frozen Fairbanks silt at different negative temperatures. The physical parameters of the Fairbanks silt under investigation were liquid limit $LL = 38.4\%$, plastic limit $PL = 34.2\%$, and specific gravity $G_s = 2.68$. It was classified as a fine-grained low plasticity silt, which is similar to the previous case from Haynes and Karalius (1977). Accordingly, the mechanical properties of frozen Fairbanks silt, at negative temperatures, are determined and used for the slope stability analysis:

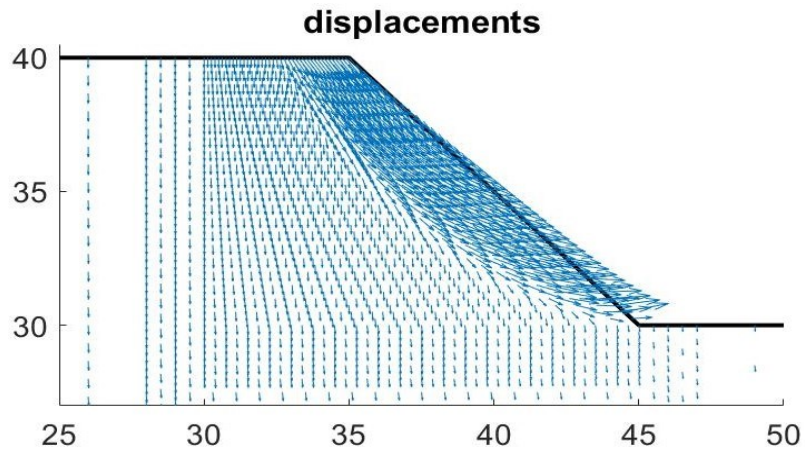
Table 5.9. Mechanical parameters of the frozen Fairbanks silt according to Zhu and Carbee (1984).

Parameters $T (^{\circ}C)$	Specific weight γ (kN/m ³)	Young's modulus E (MPa) = $740 (1.1E-5)^{0.122} (-T)^{0.624}$	Poisson's ratio ν = $-0.061 (-T)^{0.3} + 0.409$	Cohesion c (kPa) = $\frac{\sigma_m}{[2 \cdot \tan(45 + \varphi/2)]}$	Friction angle φ ($^{\circ}$)
-2	17	283.22	0.334	319.308	26
-4	17	436.483	0.3165	521.766	26
-6	17	562.145	0.3046	707.977	26
-8	17	672.682	0.2952	937.304	26
-10	17	773.182	0.2873	1231.305	26

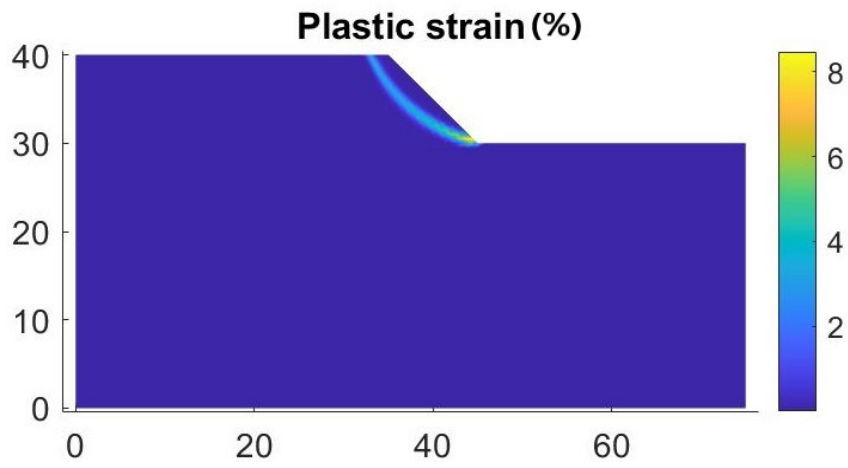
According to Table 5.9, the strength parameters change as a function of temperature, similar to previous cases. The value of specific weight for the frozen Fairbanks silt is determined based on the dry density and water content at saturation reported by Zhu and Carbee (1984). Young's modulus (=50% peak strength tangent modulus) is calculated at different temperatures using a formula in which the moderate axial strain rate is incorporated. The values of Poisson's ratio are determined using the relationship presented by Girgis et al. (2020), which was also used for the previous case (i.e. data from Haynes and Karalius 1977). The parameter σ_m in the formula for cohesion is the peak uniaxial unconfined compressive strength, measured by Zhu and Carbee (1984). Finally, similar to the previous case, the assumption of constant friction angle $\varphi = 26^{\circ}$ seems to be reasonable for the current

case, within the considered range of negative temperatures. The slope analysis results at different temperatures are presented in Figure 5.12, i.e. the plots for displacement pattern and plastic strain throughout the domain.

As clear from Figure 5.12, all the analyses resulted in slope failure. According to the displacement pattern plots, the largest displacements take place in the vicinity of slope. Furthermore, the highest values of plastic strain are observed along the thin curved zones extending from the top to the toe of slopes, developing the slip surfaces. It is also worth noting that as the temperatures decreases the highest values of plastic strain (along the critical shear zones) decrease as well. This can be mainly attributed to the fact that the increase in cohesion and Young's modulus is not at the same level, i.e. as the temperature decreases the increase in cohesion is more marked than the one in Young's modulus (see Table 5.9). This issue is noted and discussed at length in previous cases.

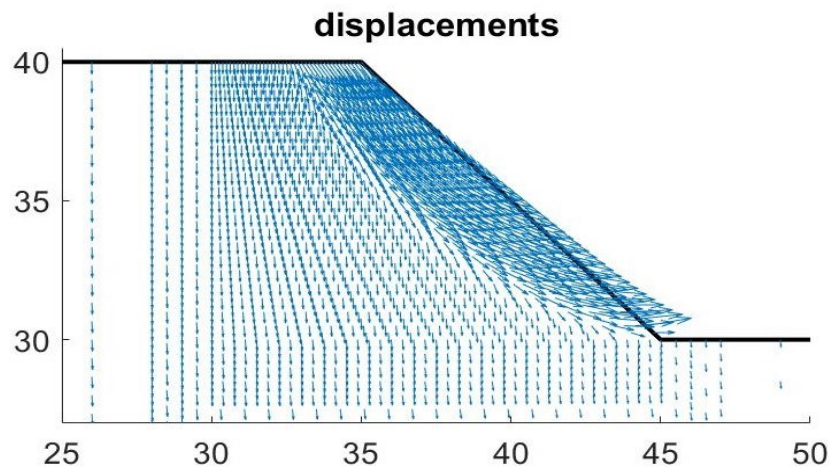


(a-1) Displacement pattern throughout the domain

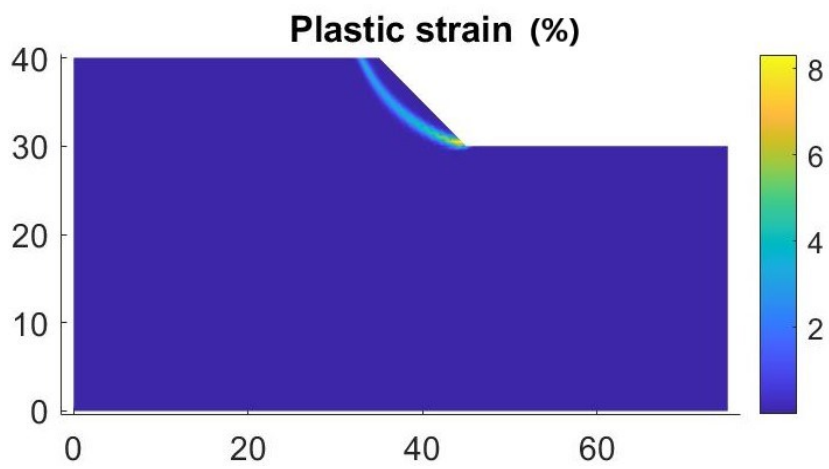


(a-2) Plastic strain throughout the domain

(a) Analysis results at $T = -2\text{ }^{\circ}\text{C}$

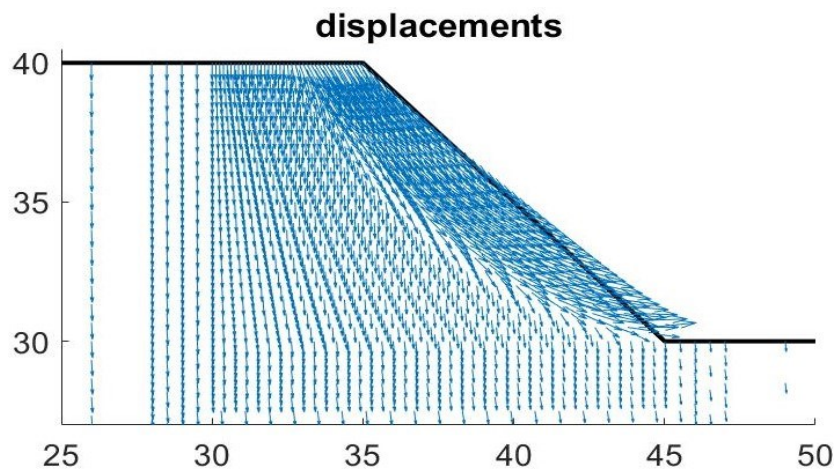


(b-1) Displacement pattern throughout the domain

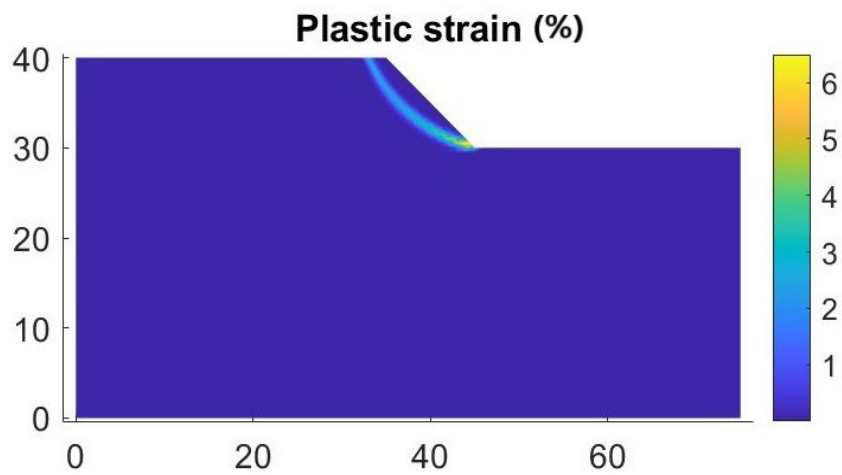


(b-2) Plastic strain throughout the domain

(b) Analysis results at $T = -4\text{ }^{\circ}\text{C}$

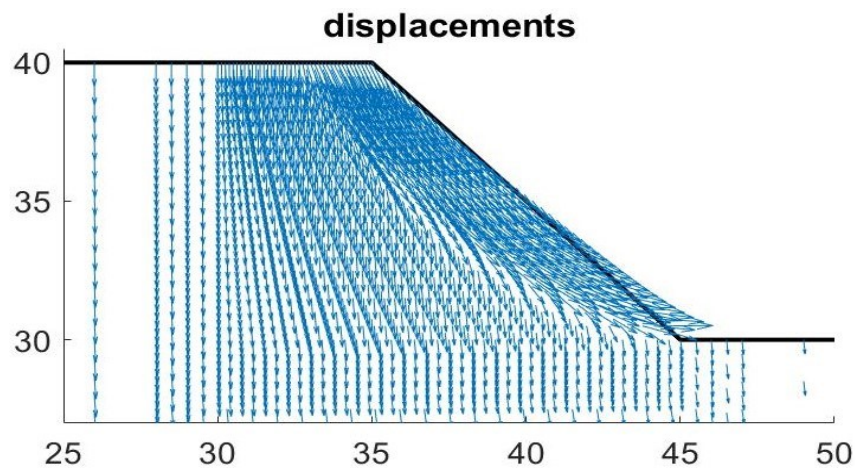


(c-1) Displacement pattern throughout the domain

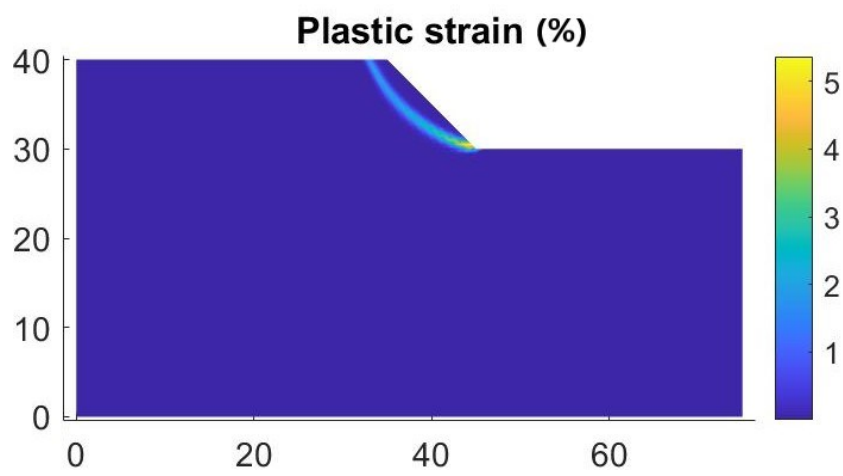


(c-2) Plastic strain throughout the domain

(c) Analysis results at $T = -6\text{ }^{\circ}\text{C}$



(d-1) Displacement pattern throughout the domain



(d-2) Plastic strain throughout the domain

(d) Analysis results at $T = -8\text{ }^{\circ}\text{C}$

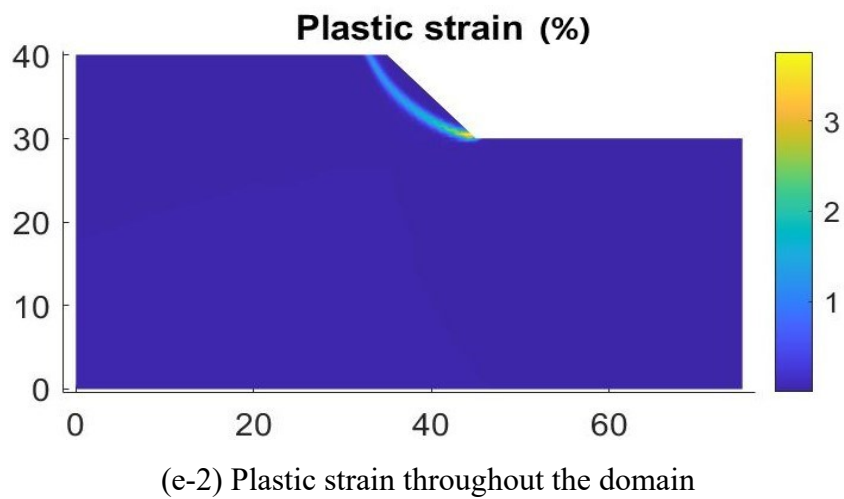
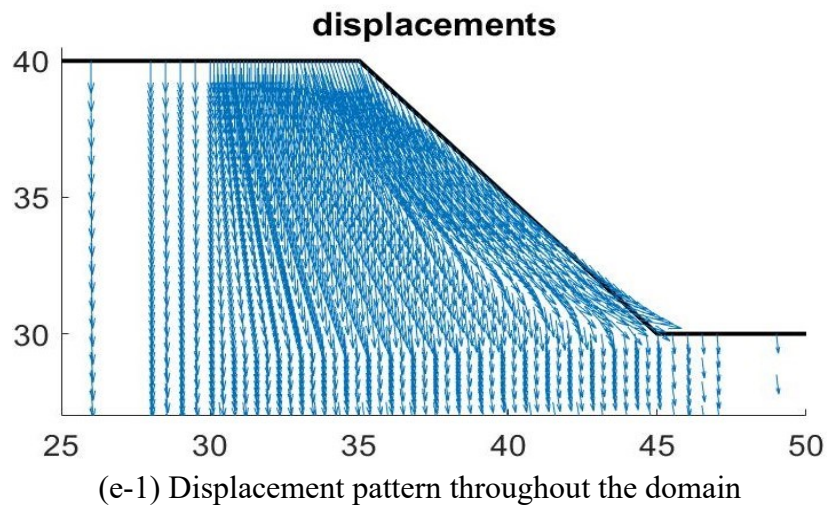


Fig. 5.12. Analysis results at (a) $T = -2^\circ\text{C}$, (b) $T = -4^\circ\text{C}$, (c) $T = -6^\circ\text{C}$, (d) $T = -8^\circ\text{C}$, and (e) $T = -10^\circ\text{C}$.

●●● In the study by *Yugui et al. (2016)*, as explained previously, triaxial compressive tests were performed on frozen silt, at negative temperatures $T = -2, -4, -6$, and -8 °C. According to their results, mechanical parameters are determined and used for our stability analysis of frozen slope:

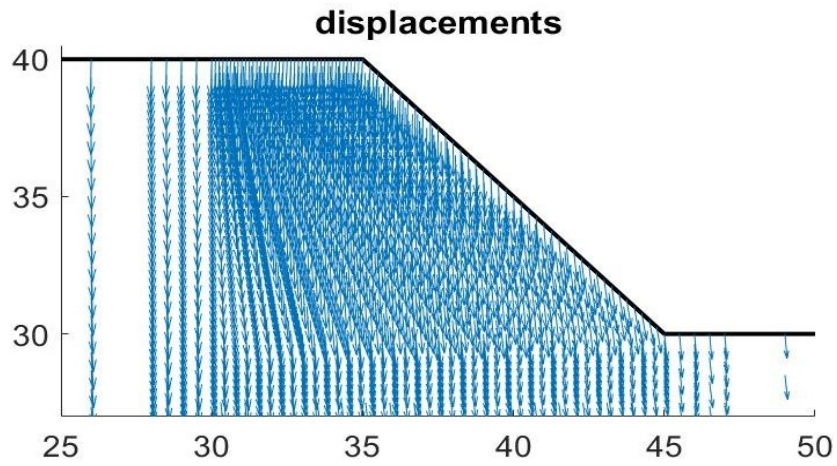
Table 5.10. Mechanical parameters of frozen silt according to *Yugui et al. (2016)*.

Parameters T (°C)	Specific weight γ (kN/m ³)	Young's modulus E (MPa) =	Poisson's ratio ν = $-0.061 (-T)^{0.3} + 0.409$	Cohesion c (kPa) =	Friction angle φ (°)
-2	20.5	181.8	0.334	825	25.9
-4	20.5	310.4	0.3165	1180	25.56
-6	20.5	373.44	0.3046	1730	25.75
-8	20.5	471.1	0.2952	1430	31.16

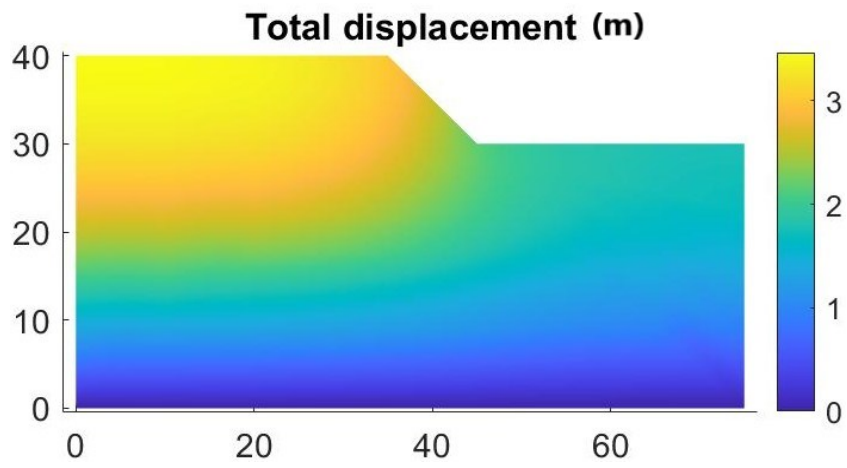
The specific weight is calculated based on the measured properties for the silt samples, i.e. water content $w = 12.8\%$ and dry density $\rho_d = 1.85$ g/cm³. Also, the plastic limit (*PL*) and liquid limit (*LL*) were measured as 15% and 23.2% respectively, which shows that the silt under investigation had low plasticity. The proposed value, by *Yugui et al. (2016)*, for the Poisson's ratio was 0.35, but in our analysis, we have employed the formula by *Girgis et al. (2020)* for the frozen Kaolinite-Sand mixture. The other parameters, as explained in Chapter 4, are determined according to the deviatoric stress-axial strain curves (i.e. $\sigma_1 - \sigma_3$ vs. ε_1 curves), and considering the linear Mohr-Coulomb (MC) strength criterion $\sigma_1 - \sigma_3 = (\sigma_1 + \sigma_3) \cdot \sin\varphi + 2 \cdot c \cdot \cos\varphi$. According to Table 5.10, the values of friction angle are almost the same as the ones considered in two previous cases, i.e. *Haynes and Karalius (1977)* and *Zhu and Carbee (1984)*. Also, the Young's modulus (=secant modulus at 50% peak strength) and cohesion increase as the temperature decreases, however, between these two parameters, the increase in cohesion is more marked.

Slope stability analyses are performed at different temperatures, considering the parameters in Table 5.10. None of the analyses resulted in slope failure/collapse, and the dominant displacement mode for the slope was downward movement, i.e.

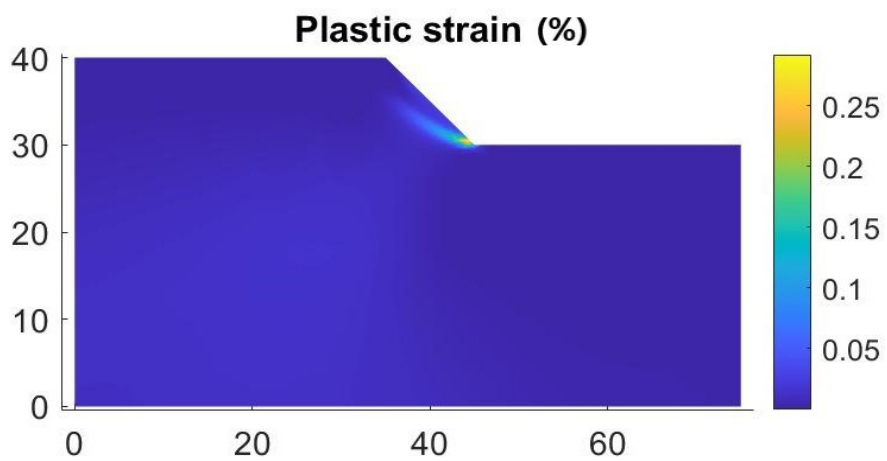
settlement, without developing any slip line (=critical shear zone). As a representative for all the analyses results, the plots for the displacement pattern, total displacement, and plastic strain corresponding to $T = -4$ °C are presented in Figure 5.13. As clear from this figure, there is no failure of the slope, and just has occurred the excessive settlement (Fig. 5.13(a)). Also, the largest total displacement has not occurred in the close vicinity of slope, and instead, it is widely distributed over an area extending to the upper and left boundaries of the domain (Fig. 5.13(b)). In addition, throughout the entire domain, plastic straining is negligible, and no slip surface/line has developed as a result (Fig. 5.13(c)). This can be attributed to the comparatively low value of Young's modulus, in combination with high values of friction angle and cohesion. The high values of cohesion and friction angle simply correspond to a high strength level for slope material, while the comparatively low value of Young's modulus implies the fact that, under each load increment, slope material would experience a wide range of elastic displacement/strain until yielding occurs, which results in less plastic straining.



(a) Displacement pattern throughout the domain



(b) Total displacement throughout the domain



(c) Plastic strain throughout the domain

Fig. 5.13. Analysis results at $T = -4\text{ }^{\circ}\text{C}$.

5.3 Sand soils

●●● *Sayles (1974)* conducted triaxial compression tests on saturated frozen Ottawa sand, using constant axial strain rate, at $T = -3.89 \text{ }^\circ\text{C}$ ($=25 \text{ }^\circ\text{F}$), considering a wide range of confining pressures. The average dry density, void ratio, porosity, and specific gravity for the samples were $\rho_d = 1670 \text{ kg/m}^3$, $e = 0.59$, $n = 37.1\%$, and $G_s = 2.65$ respectively. Considering the results reported by Sayles (1974) corresponding to low-to-medium range of confining pressure ($\approx 0.68 \text{ MPa}$) and medium range of applied axial strain rate ($\approx 7.5\text{E-}5/\text{sec}$), $V_i / V_s = (\text{vol. of ice}) / (\text{vol. of soil grains}) = 0.622$ and $S_i = \text{percent of voids filled with ice} = 105.6\%$. As a result, the volumetric ice content (depicted in Fig. 2.2 in Chapter 2) is determined based on the explanation by Sayles (1974) that “no expansion of the specimens was observed during the freezing process, and the increase in volume because of phase change from water to ice was absorbed in the free water supply connected to the bottom of the sample”. Therefore, $w_i = V_i / V = (\text{vol. of ice content}) / (\text{total vol.}) \approx V_i / (V_s + V_i) \approx 0.38$ (which is almost equal to the average porosity n for the samples), assuming that there was no air within the sample’s pore space and the sample was completely frozen. The frozen soil can be classified as intermediate ice-content. The Young’s modulus, i.e. tangent modulus at 50% peak strength, was reported by Sayles (1974) as $E_{50\%} \approx 1500 \text{ MPa}$. Also, for our analysis, the Poisson’s ratio is assumed to be $\nu = 0.3$.

In order to determine the shear strength parameters c and ϕ , the approach proposed by Nater et al. (2008) is employed and slightly modified:

Since in the study by Sayles (1974), at $T = -3.89 \text{ }^\circ\text{C}$ the saturated Ottawa sand samples were completely frozen, at higher temperatures, the ice content of the sample (as a fraction of volumetric ice content when completely frozen) can be calculated as $w_{\text{ice}} = (-T / 3.89)^{0.5}$. At the reference temperature $T = -2.1 \text{ }^\circ\text{C}$, introduced by Nater et al. (2008), $w_{\text{ice}} = 0.735$, then the volumetric ice content will be $w_i (\text{at } T = -2.1^\circ\text{C}) = 0.735 * 0.38 = 0.28$. The cohesion at the reference temperature is $c (T = -2.1^\circ\text{C}) = 534.93 \bullet w_i^{1.91} (\text{at } T = -2.1) = 47.03 \text{ kPa}$. Then cohesion at $T = -3.89 \text{ }^\circ\text{C}$ will be $c = - [c (T = -2.1^\circ\text{C}) / 2.1] \bullet T = 87.12 \text{ kPa}$. As for the friction angle, it is mentioned by Sayles (1974) that the friction

angle for the unfrozen Ottawa sand is $\varphi_{\text{initial}} \approx 31^\circ$. According to the proposed approach by Nater et al. (2008), at $T = -3.89^\circ\text{C}$, $\varphi = \varphi_{\text{initial}} - \varphi_{\text{initial}} \bullet w_i^{2.6} = 31 - 31 \bullet (0.38)^{2.6} = 28.5^\circ$. The obtained values for the strength parameters are in agreement with the remarks of Sayles (1974): “The resistance of saturated frozen Ottawa sand in a confined stress condition consists of the cohesion of the ice matrix and the frictional resistance of the sand grains. In addition, at medium axial strain rates (and lower rates), while the confining pressure is applied, friction between the sand grains is more activated, since the ice matrix is allowed time to creep from between the sand grains where the stress concentration is high, thus bringing more sand grains into closer contact and creating greater frictional resistance.” Moreover, it is pointed out by Arenson et al. (2004) that frozen soils with a volumetric ice content lower than about 40% (i.e. sand-rich samples) start behaving like pure ice at the beginning of loading. However, after some straining the ice matrix starts to fail and the behaviour approaches that of an unfrozen material.

The mechanical parameters of the frozen Ottawa sand, presented in the table below, are used for the slope stability analysis.

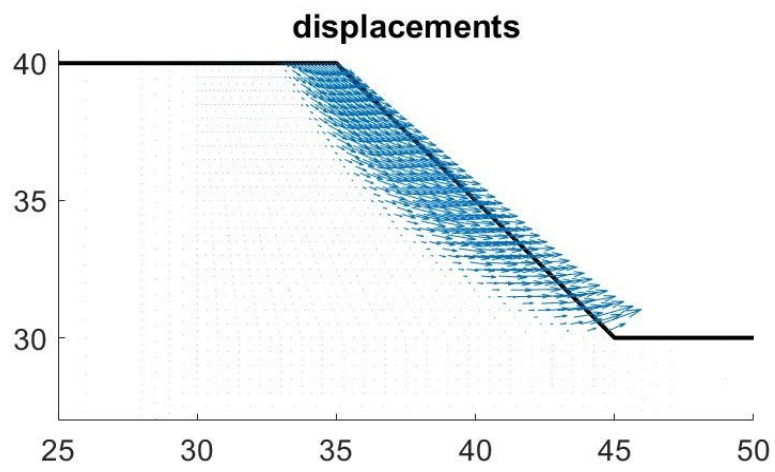
Table 5.11. Mechanical parameters of frozen Ottawa sand determined based on the study by Sayles (1974).

Parameters $T (^{\circ}\text{C})$	Specific weight γ (kN/m ³)	Young's modulus E (MPa)	Poisson's ratio ν	Cohesion c (kPa)	Friction angle φ ($^{\circ}$)
-3.89	20	1500	0.3	87.12	28.5

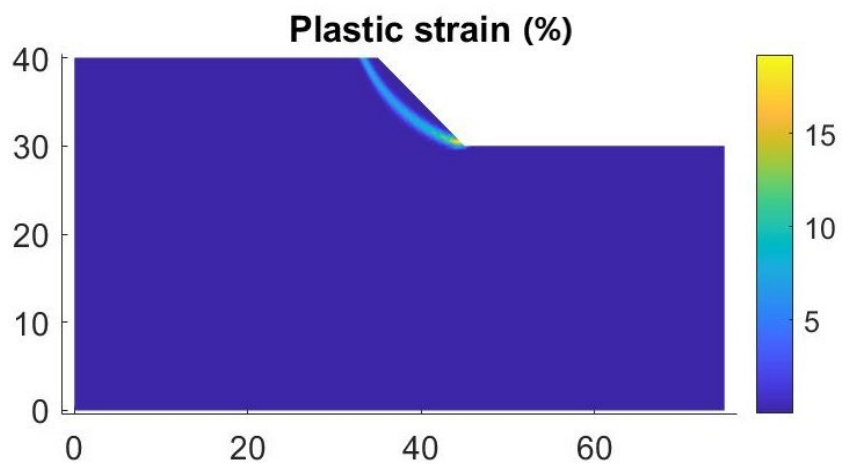
It should be emphasised that for the intermediate ice-content frozen sands (or frozen sand-rich soils) both the cohesion and frictional terms of strength play important roles. Specially, when it comes to the analysis of phenomena such as frozen slope instability, normally the slope material would experience a range of straining to reach their strength, and then failure occurs. Therefore, the values determined for the strength properties seem to be valid and acceptable. The analysis results are presented in the Figure 5.14, considering the mechanical parameters in Table 5.11. As clear

from the figure, similar to the previous cases where the analyses resulted in slope failure, the plot for the displacement pattern (Fig. 5.14a) illustrates that the largest displacements has taken place in the vicinity of slope. In addition, the highest values of plastic strain are observed along the thin curved zone extending from the top to the toe of slope, developing the slip surface along which the slope collapse has occurred (Fig. 5.14b).

It is noted by Nater et al. (2008) that when the frictional component of shear strength is large comparing to the cohesion term, like in the current case, the failure surface shifts towards the surface of the slope. On the other hand, when the cohesion strength is comparatively large, a deeper lying failure surface develops.



(a) Displacement pattern throughout the domain



(b) Plastic strain throughout the domain

Fig. 5.14. Analysis results at $T = -3.89\text{ }^{\circ}\text{C}$.

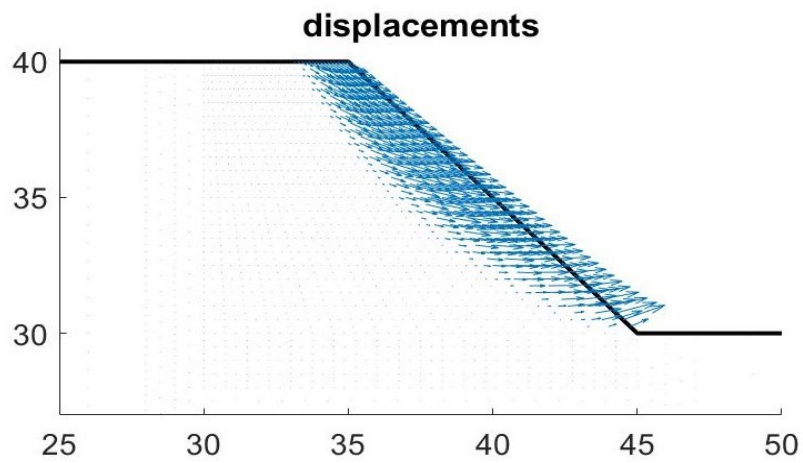
●●● In the study by *Parameswaran (1980)*, also addressed in Chapters 2 and 4, uniaxial unconfined compression tests were performed on frozen saturated Ottawa sand. The average dry density of the samples was close to the optimum, $\rho_d = 1700 \text{ kg/m}^3$, and the total moisture content was about $w = 20\%$ at saturation. Since the values of compressive strength and initial Young's modulus obtained from the curves/plots presented by Parameswaran (1980) were relatively high to be considered for the slope stability analysis, instead, slightly modified values are determined here by using the proposed approach by Nater et al. (2008). It is not explicitly mentioned by Parameswaran (1980) at what temperature the specimens were completely frozen. Therefore, based on the assumption by Nater et al. (2008), it is assumed that at $T = -5 \text{ }^\circ\text{C}$ the soil is completely frozen. At higher temperatures, the ice content of the sample (as a fraction of the volumetric ice content when completely frozen) can be calculated as $w_{\text{ice}} = (-T / 5)^{0.5}$, and at lower temperatures, obviously, $w_{\text{ice}} = 1$. A temperature range of -2 to $-6 \text{ }^\circ\text{C}$ is considered for our slope analysis. Similar to the previous case, i.e. study by Sayles (1974), the specific gravity, Poisson's ratio and unfrozen friction angle are assumed to be $G_s = 2.65$, $\nu = 0.3$, and $\varphi = 31^\circ$ respectively. Using the common relationship $S \bullet e = G_s \bullet w$, void ratio and porosity are calculated as $e = 0.53$ and $n = 0.35$. According to Parameswaran (1980), the Ottawa sand specimen was connected to a vacuum pump to remove air, then saturated with deaerated distilled water. In addition, during the freezing process, expelled water was removed from the bottom of the sample. Accordingly, it is assumed that there was no air within the pore space and no sample expansion during freezing, therefore, the volumetric ice content at $-5 \text{ }^\circ\text{C}$ is $w_i \text{ (at } T = -5^\circ\text{C)} = n = 0.35$. At the reference temperature $T = -2.1 \text{ }^\circ\text{C}$ (introduced by Nater et al. 2008), $w_{\text{ice}} = 0.65$, then the volumetric ice content will be $w_i \text{ (at } T = -2.1^\circ\text{C)} = 0.65 * 0.35 = 0.23$. The cohesion at the reference temperature, as defined by Nater et al. (2008), is $c \text{ (} T = -2.1^\circ\text{C)} = 534.93 \bullet w_i^{1.91} \text{ (at } T = -2.1) = 32.3 \text{ kPa}$. Cohesion values at other negative temperatures T will be $c \text{ (kPa)} = - [c \text{ (} T = -2.1^\circ\text{C)} / 2.1] \bullet T$. As for the friction angle, according to Nater et al. (2008), at negative temperatures, $\varphi \text{ (}^\circ\text{)} = \varphi_{\text{initial}} - \varphi_{\text{initial}} \bullet w_i^{2.6} = 31 - 31 * (w_{\text{ice}} \bullet 0.35)^{2.6}$. Mechanical parameters are determined at negative temperatures and presented in the table below.

Table 5.12. Mechanical parameters of frozen Ottawa sand determined based on the study by Parameswaran (1980).

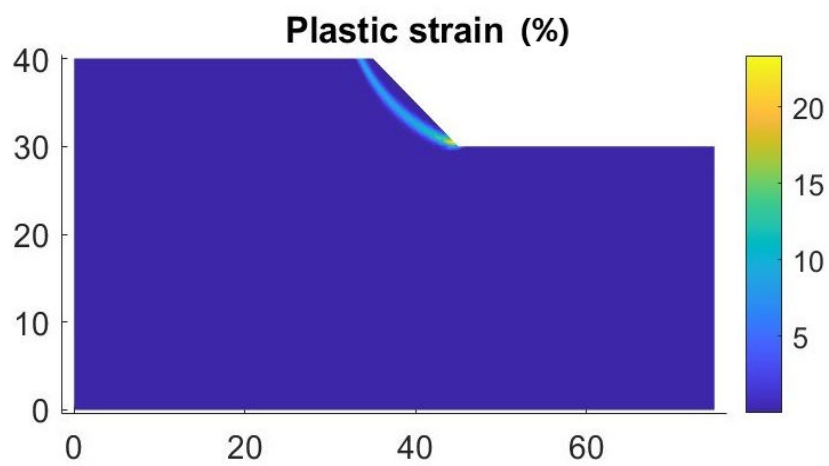
Parameters T (°C)	Specific weight γ (kN/m ³)	Young's modulus E (MPa)	Poisson's ratio ν	Cohesion c (kPa)	Friction angle ϕ (°)
-2	20	599.67	0.3	30.762	30.4
-3	20	836.18	0.3	46.143	29.96
-4	20	1072.685	0.3	61.524	29.5
-5	20	1309.1925	0.3	76.905	28.98
-6	20	1545.7	0.3	92.286	28.98

As mentioned before, the initial tangent moduli reported by Parameswaran (1980) were relatively high to be used for the slope analysis. As a result, the secant modulus at 50% peak strength is determined using the stress-strain curves measured at $T = -2$ (under the strain rates of 1.3 to 2.6E-5 /sec) and $T = -6$ °C (under the strain rates of 1.2E-5 to 1.2E-4 /sec). For temperatures in between, simple linear interpolation is employed. The $E_{50\%}$ values are presented in Table 5.12 as well. Accordingly, within the considered temperature range, at lower temperatures, the Young's modulus and the cohesion have higher values, while the friction angle slightly decreases. The slope analysis results at different temperatures are presented in Figure 5.15. The results include the plots for displacement pattern and plastic strain throughout the domain. As clear from the figure, all the analyses resulted in slope failure. Similar to the previous cases with slope failure, the largest displacements have taken place in the vicinity of slope. Also, the highest values of plastic strain are observed along the thin curved zones extending from the top to the toe of slopes, developing the slip surfaces. The plastic strain values (at different temperatures) are of the same order of magnitude and within a narrow range.

Here, similar to the previous case by Sayles (1974), the frozen Ottawa sand is of intermediate ice-content (it can be considered as a sand-rich frozen soil). Therefore, the discussion and argument presented before, about how the shear strength would develop for frozen sand-rich soil, apply here as well.

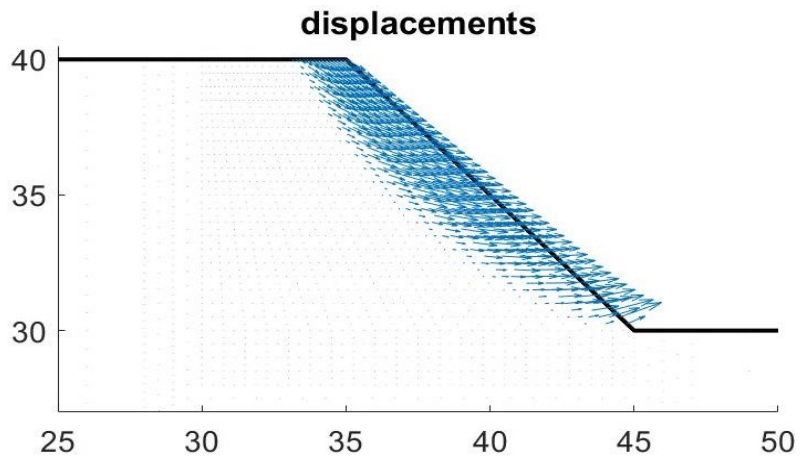


(a-1) Displacement pattern throughout the domain

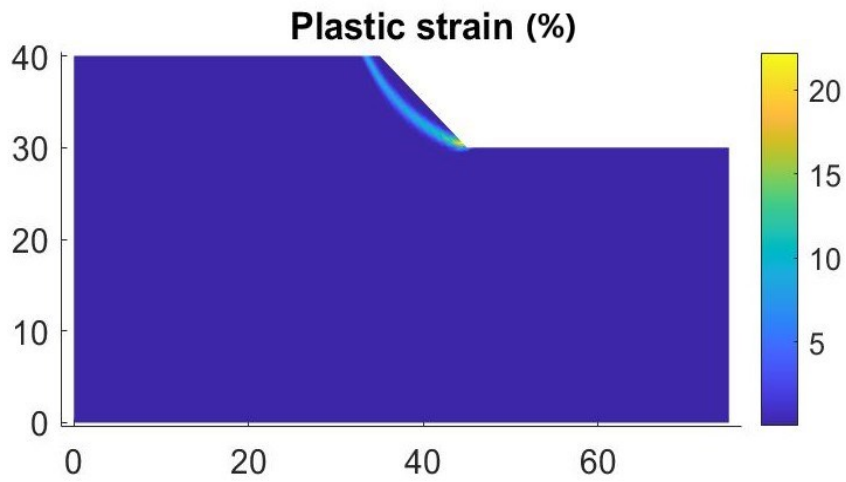


(a-2) Plastic strain throughout the domain

(a) Analysis results at $T = -2\text{ }^{\circ}\text{C}$

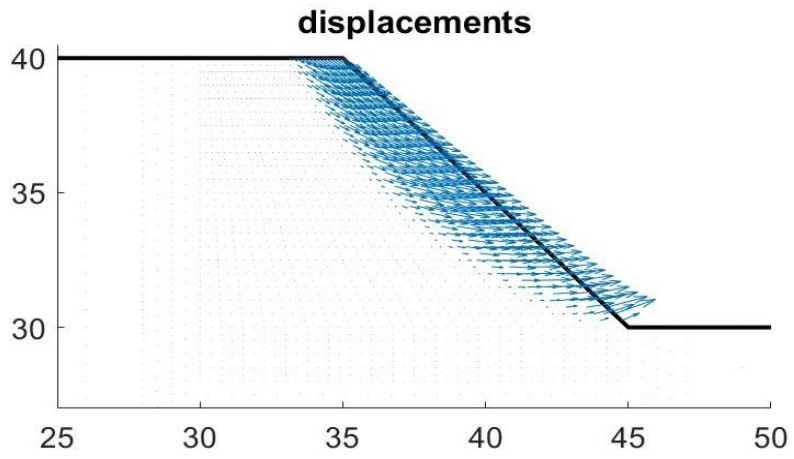


(b-1) Displacement pattern throughout the domain

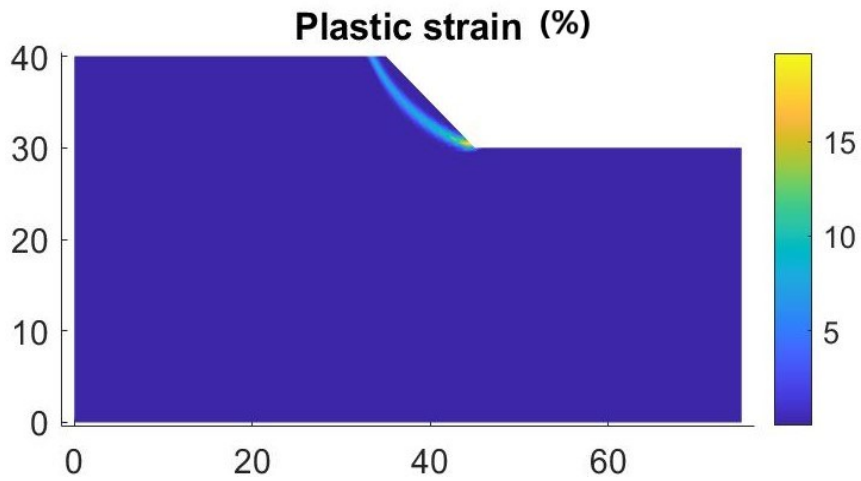


(b-2) Plastic strain throughout the domain

(b) Analysis results at $T = -3\text{ }^{\circ}\text{C}$

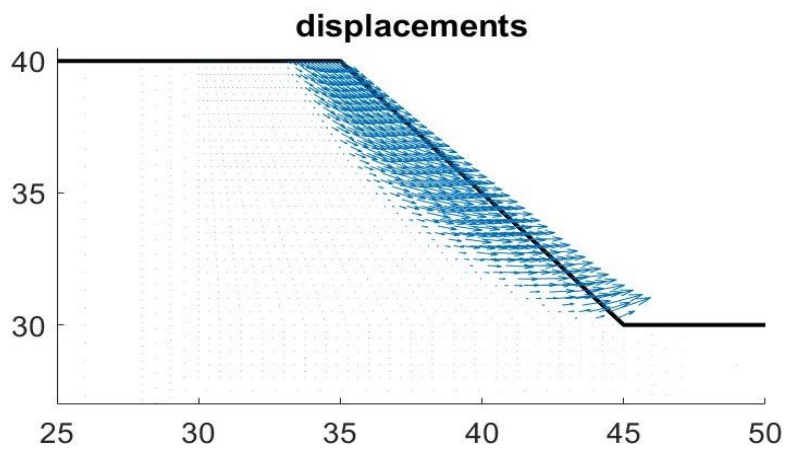


(c-1) Displacement pattern throughout the domain

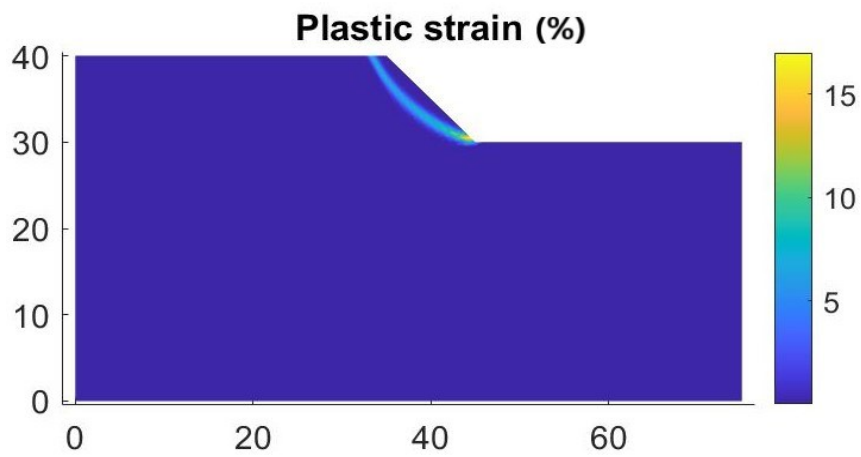


(c-2) Plastic strain throughout the domain

(c) Analysis results at $T = -4\text{ }^{\circ}\text{C}$

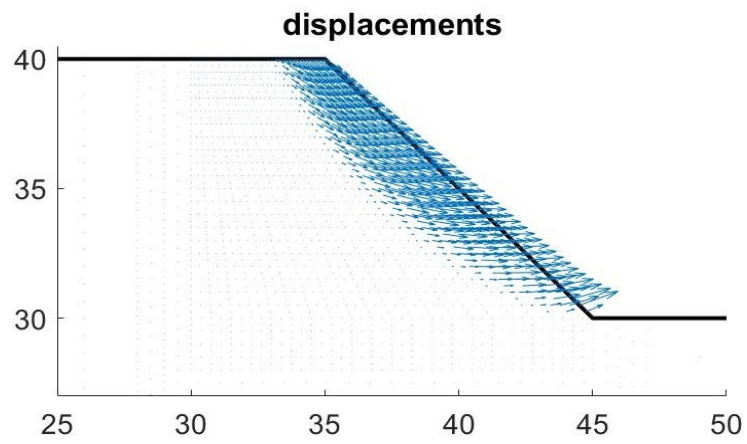


(d-1) Displacement pattern throughout the domain

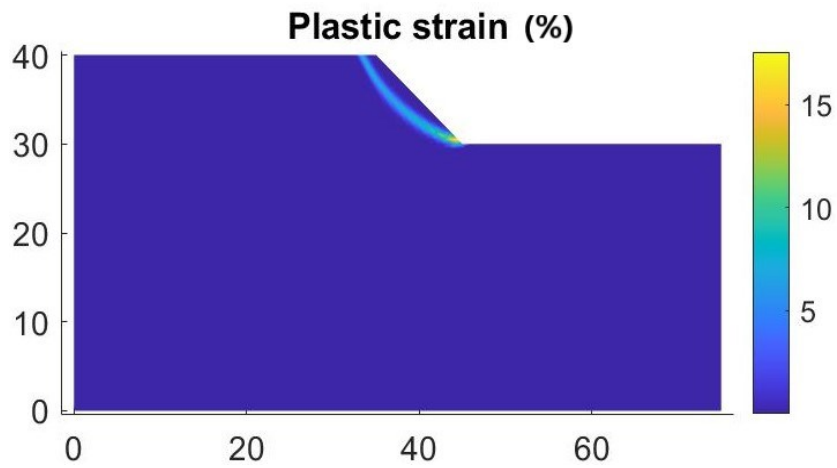


(d-2) Plastic strain throughout the domain

(d) Analysis results at $T = -5\text{ }^{\circ}\text{C}$



(e-1) Displacement pattern throughout the domain



(e-2) Plastic strain throughout the domain

(e) Analysis results at $T = -6^\circ\text{C}$

Fig. 5.15. Analysis results at (a) $T = -2^\circ\text{C}$, (b) $T = -3^\circ\text{C}$, (c) $T = -4^\circ\text{C}$, (d) $T = -5^\circ\text{C}$, and (e) $T = -6^\circ\text{C}$.

●●● In the study by *Yang et al. (2010)*, a series of triaxial compression tests were conducted on frozen sand, at $T = -6$ °C, under the axial strain rate of $1.67E-4/\text{sec}$ (moderate strain rate). It is mentioned by Yang et al. (2010) that “frozen soil medium is comprised of mineral particles, ice, liquid water, and gas inclusions, which makes it sensitive to temperature, water content and pressure. Therefore, the mechanical characteristic of frozen soil is more complicated compared to unfrozen soil”. The sand material used in their study had the dry density $\rho_d = 1810 \text{ kg/m}^3$ and water content $w\% = 15\%$. Initially, the specimens were quickly frozen to -35 °C to prevent water transmission within the sample, and then before tests, they were kept in a cold room at -6 °C. Based on their test results under a wide range of confining pressures, Yang et al. (2010) generated different formulae for parameters including the Young’s modulus E , cohesion c , and friction angle ϕ as functions of confining pressure. Since a wide range of confining pressures was considered in their study, the non-linear Mohr-Coulomb (MC) criterion was employed to describe the strength characteristics of frozen sand. However, it is worth mentioning that for low-to-medium stress levels, the linear MC criterion works well and is widely used in geotechnical applications. Accordingly, mechanical parameters are determined and presented in the table below. These parameters are used for our slope stability analysis.

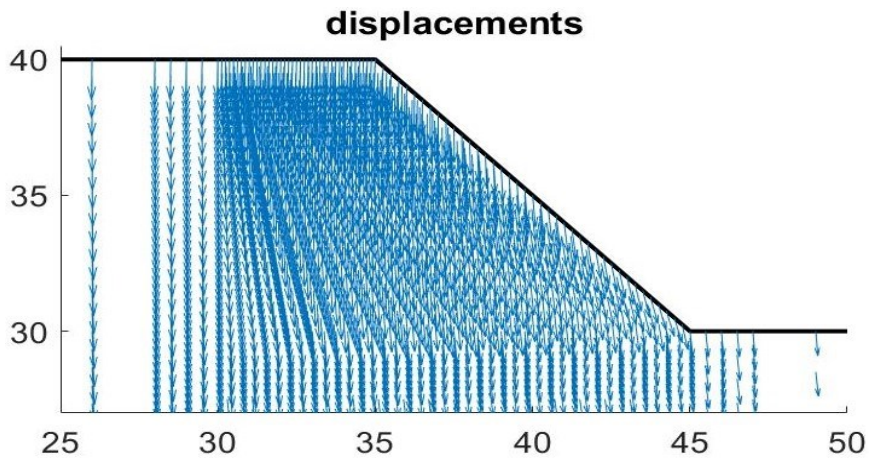
Table 5.13. Mechanical parameters of frozen sand based on the study by Yang et al. (2010).

Parameters T (°C)	Specific weight γ (kN/m ³)	Young’s modulus E (MPa) = $[1.704E-4 * (\sigma_3/P_a)^3 + 0.113 * (\sigma_3/P_a)^2 - 14.411 * (\sigma_3/P_a) + 3462.538] * P_a$	Poisson’s ratio ν	Cohesion c (kPa) = $[2.822E-5 * (\sigma_3/P_a)^3 - 8.45E-3 * (\sigma_3/P_a)^2 + 0.969 * (\sigma_3/P_a) + 6.604] * P_a$	Friction angle ϕ (°) = $-1.085E-7 * (\sigma_3/P_a)^4 + 4.8826E-6 * (\sigma_3/P_a)^3 + 5.26E-3 * (\sigma_3/P_a)^2 - 0.7744 * (\sigma_3/P_a) + 28.784$
-6	20.42	349.393	0.3	766.481	28.015

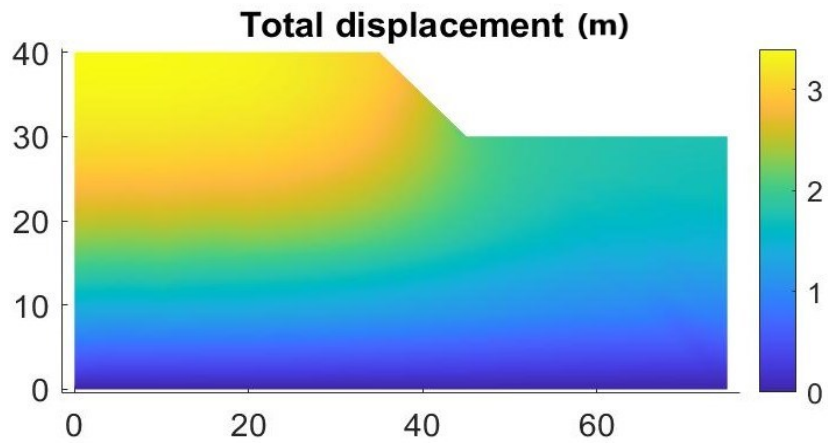
The Poisson’s ratio is assumed to be $\nu = 0.3$, similar to the previous cases for the frozen sand soil. Within the formulae for E , c , and ϕ , the parameters σ_3 and P_a are the confining pressure and atmospheric pressure (=101.325 kPa) respectively. For the

current slope stability problem, an average value of $\sigma_3 = P_a$ is considered, which is well within the low-to-medium range (0-200 kPa) corresponding to the stress level from the top to the bottom of slope.

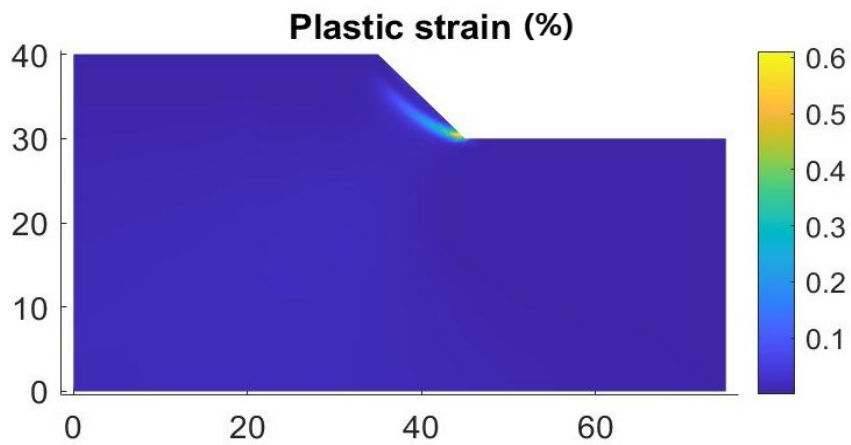
The analysis results are presented in Figure 5.16. As clear from this figure, slope failure has not occurred, and the dominant mode of displacement for slope material was downward movement (Fig. 5.16a), i.e. excessive settlement, without developing any slip line (=critical shear zone). Also, the largest total displacement is widely distributed over an area extending to the upper and left boundaries of the domain (Fig. 5.16b). In addition, over the entire domain, plastic straining was negligible, and no slip surface/line has developed as a result (Fig. 5.16c). This is attributed to the high values of cohesion and friction angle (compared to the Young's modulus), which obviously resulted in a high shear strength level for the slope material. In this case, the Young's modulus is not small, but in comparison, cohesion and friction angle are of much higher values. Therefore, the slope would experience large elastic displacements/strains, under applied load increments, until plastic straining is reached. As a result, at the end of analysis, plastic stains were insignificant throughout the entire domain.



(a) Displacement pattern throughout the domain



(b) Total displacement throughout the domain



(c) Plastic strain throughout the domain

Fig. 5.16. Analysis results at $T = -6\text{ }^{\circ}\text{C}$.

6 Summary and recommendations for future work

In this research, first, many studies available in the literature were carefully investigated in order to find a common approach for deriving/determining reliable mechanical parameters for the stability analysis of frozen soil slopes. Many researchers have worked on shear strength characteristics of frozen soils by conducting uniaxial unconfined or triaxial compressive and tensile tests, at different ranges of below zero temperatures, and under various (=high, moderate, low) strain rates. In our study, those results corresponding to moderate axial strain rates ($1.1E-5$ to $4E-4$ /sec) were considered. Not all the data from literature were appropriate for our frozen slope stability analysis, and at times, slight modifications were required/made. Next, the derived material and mechanical parameters were used as the input data for a finite element (FE) MATLAB code incorporating the Drucker-Prager yield criterion (as the failure criterion), with perfect plasticity at small strains and associative plastic flow rule. The FE analysis was performed for a slope with fixed geometry, under self weight, considering strain localization to define the slip surface (=critical shear zone) for the failure/collapse mechanism. The (negative) temperature range considered in our analyses depended mainly on the reviewed studies, and yet it was kept (below zero and) higher than -10°C . This was because in common practice of frozen slope analysis, the average temperature between the ground surface and the depth of the slope (temperature profile) is not below (or colder than) this range. The analyses were performed for frozen clay, silt, and sand soils (as presented and discussed in Chapter 5).

6.1 Conclusions

According to our study, several *conclusions* are drawn as follows:

- As the temperature is decreased, the shear strength of frozen soil increases. At lower temperatures, parameters such as Young's modulus E and cohesion c almost always increased, while the Poisson's ratio ν decreased. The friction angle ϕ , however, depending on the frozen soil under

investigation, experienced an increase or a decrease. The increase in E and c was more marked and significant than the decrease in ν and the change in ϕ within the range of negative temperatures considered.

- There appeared to be no unique or common approach for deriving/determining appropriate strength parameters to be considered for the stability analysis of frozen soil slopes; For frozen clay soils, in each case, the formulae proposed by the respective researcher(s) were used to determine the strength parameters at various negative temperatures. For frozen silt soils, the stress-strain curves reported in each study were employed directly to determine the Young's modulus (secant or tangent at 50% peak strength) and cohesion (considering the linear Mohr-Coulomb criterion). Also, for friction angle and Poisson's ratio reasonable values or relationships were assumed. Wherever the strength properties were to be defined with respect to the applied confining pressure, the low-to-medium range of stress levels was considered which corresponded to our slope stability problem. And finally for frozen sand soils, the Young's modulus (at 50% peak strength) was determined using the stress-strain curves and the cohesion and friction angle were determined based on the approach by Nater et al. (2008), incorporating the volumetric ice content w_i of the frozen soil into the calculation procedure.
- In many cases, the stability analyses resulted in slope failure. The plots showed the pattern and distribution of total displacements and plastic strains throughout the domain. The highest total displacements and plastic strains occurred in the close vicinity of slope which is where the slope material would experience excessive movement and collapse. In fact, the highest values of plastic strains (well above 2 or 3% in most cases) developed a thin curved zone (=critical shear zone) extending from the top to the toe of slope. In some cases, on the other hand, stability analyses didn't result in slope failure/collapse, due to the values of mechanical

parameters E , c , and ϕ . Whenever Young's modulus was not high compared to cohesion and friction angle, under each load increment the frozen slope material would experience a wider range of elastic displacements/strains until they reach plastic straining. Therefore, plastic strains throughout the domain were not large enough, and the slip surface/line could not develop (close to the slope). In these cases, plastic strains remained well below 1%.

- The case studies performed here show that the MATLAB code is fairly capable of capturing the mechanism of slope failure considering the frozen soil strength characteristics (obtained at different negative temperatures and under moderate applied strain rates).

6.2 Recommendations for future work

Regarding our study, there are several areas and related aspects that need further investigation. The following are a few *suggestions/recommendations* for future work:

- As presented in Chapter 5, the strength parameters reported in (or obtained from) different studies for each soil type (i.e. clay, silt, and sand) were not always consistent with each other. For instance, for frozen clays from different sites, there were different formulae/relationships or plots giving the values of mechanical parameters at various negative temperatures. The main reason seems to be the fact that different researchers used soils with different mineralogy, they might have used different sampling techniques, test devices, test conditions, etc. Accordingly, it is highly recommended that for each specific site, and geotechnical or construction application (being slope stability analysis, foundation design, etc.), the appropriate tests, sampling methods and devices should be employed.
- Regarding the numerical modeling and analysis in this study, the Drucker-Prager criterion was defined as the yield criterion for the frozen slope

material. Also, the stress-strain behavior of frozen soil was defined to be elastic-perfectly plastic at small strains. Because of the complicated multiphase nature of frozen soil, and the fact that as straining continues phase change/transition occurs within the medium, it is suggested that for investigating different phenomena such as slope stability (which involves medium-to-large straining), more sophisticated yield criteria and stress-strain models be considered.

- Normally in practice, frozen slopes, and more specifically slopes in permafrost regions, consist of a top shallow (active) layer where the seasonal temperature changes are more marked, underlain by a much deeper layer with less temperature variations over time. During the freezing/cold days the temperature near the surface becomes more negative, while at depth, it stays close to 0°C. In our study, each negative constant temperature was considered for the entire depth of slope, and there was no temperature profile showing how it changed from the ground surface to the depth of the toe of slope. It is suggested that for future work, temperature profile should be incorporated into the numerical modeling. This way, the mechanical parameters would change with depth as well, resulting in more realistic simulation results.
- Two major factors influencing the strength of frozen soils include the unfrozen water content (directly related to the ice content) and the volumetric ice content ($= \text{volume of ice} / \text{total volume of frozen soil specimen}$). The unfrozen water content is closely related to the temperature. In case of fine-grained soils, even at very low temperatures, there can still be some amount of unfrozen water content within the pore space of the frozen soil. This plays a significant role in shear strength characteristics of frozen soil. It is suggested that, if possible, the formulae derived and employed for determining mechanical parameters at negative temperatures incorporate the unfrozen water content (or the pore ice

content) and temperature values to be more realistic. The other major factor, i.e. the volumetric ice content, is very important in developing the shear failure mechanisms of frozen soil. In our study, almost all the frozen soil test samples investigated were of intermediate ice content (where both cohesion and friction angle terms of strength are important). For the ice-rich frozen soils, on the other hand, the peak strength is normally governed by the cohesion strength of the pore ice. It is highly recommended that based on the volumetric ice content of the frozen soil under investigation, the effective shear strength parameters should be determined properly and employed in the numerical modeling.

References

1. Akhtar S. and Li B. (2020). Numerical analysis of pipeline uplift resistance in frozen clay soil considering hybrid tensile-shear yield behaviors. *International Journal of Geosynthetics and Ground Engineering* 2020 6:47, 6(4):1–12. <https://doi.org/10.1007/S40891-020-00228-9>.
2. Andersland O.B. and AlNouri I. (1970). Time-dependent strength behavior of frozen soils. *Journal of the Soil Mechanics and Foundation Division (ASCE)*, 96(4):1249–1265. <https://doi.org/10.1061/JSFEAQ.0001438>.
3. Anderson D.M and Tice A.R. (1972). Predicting unfrozen water content in frozen soils from surface area measurements. *Highway Research Record*, Issue 393.
4. Arenson L.U. (2002). Unstable Alpine permafrost: a potentially important natural hazard. Variations of geotechnical behavior with time and temperature. *Doctoral thesis*. <https://doi.org/10.3929/ETHZ-A-004442393>.
5. Arenson L.U., Johansen M.M., Springman S.M. (2004). Effects of volumetric ice content and strain rate on shear strength under triaxial conditions for frozen soil samples. *Permafrost and Periglacial Processes*, 15(3):261–271. [doi:10.1002/ppp.498](https://doi.org/10.1002/ppp.498).
6. Arenson L.U. and Sego D.C. (2006). The effect of salinity on the freezing of coarse-grained soils. *Canadian Geotechnical Journal*, 43(3):325–337. <https://doi.org/10.1139/T06-006>.
7. Arenson L.U. and Springman S.M. (2005a). Triaxial constant stress and constant strain rate tests on ice-rich permafrost samples. *Canadian Geotechnical Journal*, 42(2):412–430. <https://doi.org/10.1139/t04-111>.
8. Arenson L.U. and Springman S.M. (2005b). Mathematical description for the behavior of ice-rich frozen soils at temperatures close to zero centigrade. *Canadian Geotechnical Journal*, 42(2):431–442. <https://doi.org/10.1139/t04-109>.

9. Arenson L.U., Springman S.M., Segoo D.C. (2007). The rheology of frozen soils. *Journal of Applied Rheology*, 17(1):1–14. doi:10.1515/arh-2007-003.
10. Arenson L.U., Xia D.D., Segoo D.C., Biggar K.W. (2005). Brine and unfrozen water migration during the freezing of Devon silt. *4th Biennial Workshop on Assessment and Remediation of Contaminated Sites in Arctic and Cold Climates (ARCSACC)*, Issue January:35–44.
11. Bai R., Lai Y., Pei W., Zhang M. (2020). Investigation on frost heave of saturated–unsaturated soils. *Acta Geotechnica 2020 15:11*, 15(11):3295–3306. <https://doi.org/10.1007/S11440-020-00952-6>.
12. Barker J. and Thomas H. (2013). Geotechnical engineering in cold regions. *ISCORD 2013: Planning for Sustainable Cold Regions (ASCE 2013)*. <https://doi.org/10.1061/9780784412978.020>.
13. Beskow G. (1935). Soil freezing and frost heaving with special applications to roads and railroads. *Swedish Geological Society, C, No. 375, Year Book No. 3 (translated by J.O. Osterberg) in Historical Perspectives in Frost Heave Research, USA Cold Region Research and Engineering Laboratory, Special Report*, 91(23):41–157.
14. Black P.B. and Hardenberg M.J. (1991). Historical perspectives in frost heave research. *U.S. Army Corps of Engineers, Cold Regions Research and Engineering Laboratory*.
15. Bragg R.A. and Andersland O.B. (1981). Strain rate, temperature, and sample size effects on compression and tensile properties of frozen sand. *Engineering Geology*, 18(1–4):35–46. [https://doi.org/10.1016/0013-7952\(81\)90044-2](https://doi.org/10.1016/0013-7952(81)90044-2).
16. Chen W.F. (1982). *Plasticity in reinforced concrete*. McGraw-Hill in New York, London, 474 pages.
17. Chen W.F. and Mizuno E. (1990). *Nonlinear analysis in soil mechanics: theory and implementation*. Amsterdam, New York: Elsevier.

18. de Souza Neto E.A., Perić D., Owen D.R.J. (2008). Computational methods for plasticity: theory and applications. Civil and Computational Engineering Centre, Swansea University. A John Wiley and Sons, Ltd, Publication.
19. Fish J. and Belytschko T. (2007). A first course in finite elements. John Wiley and Sons Ltd, The Atrium, Southern Gate, Chichester, West Sussex PO19 8SQ, England.
20. Fish A.M. and Zaretsky Y.K. (1997). Temperature effect on strength of ice under triaxial compression. *In Seventh International Offshore and Polar Engineering Conference, Honolulu, Hawaii, USA, May 1997*:415–422.
21. Girgis N., Li B., Akhtar S., Courcelles B. (2020). Experimental study of rate-dependent uniaxial compressive behaviors of two artificial frozen sandy clay soils. *Cold Regions Science and Technology*, 180(2020):103166. <https://doi.org/10.1016/J.COLDREGIONS.2020.103166>.
22. Glen J.W. (1955). The creep of polycrystalline ice. *In Proceedings of the Royal Society A: Mathematical, Physical, and Engineering Sciences*, 228(1175):519–538. <https://doi.org/10.1098/rspa.1955.0066>.
23. Gold L.W. (1970). Process of failure in ice. *Canadian Geotechnical Journal*, 7(4):405–413.
24. Goughnour R.R. and Andersland O.B. (1968). Mechanical properties of a sand-ice system. *Journal of the Soil Mechanics and Foundations Division, ASCE*, 94(4):923–950. <https://doi.org/10.1061/JSFEAQ.0001179>.
25. Guthrie W.S. and Hermansson A. (2003). Frost heave and water uptake relations in variably saturated aggregate base materials. *Transportation Research Record: Journal of the Transportation Research Board*, 1821(1):13–19. [doi:10.3141/1821-02](https://doi.org/10.3141/1821-02).

26. Haeberli W., Wegmann M., Vonder Mühll D.S. (1997). Slope stability problems related to glacier shrinkage and permafrost degradation in the Alps. *Eclogae Geologicae Helvetiae*, 90:407–414.
27. Harris J.S. (1995). Ground freezing in practice. Thomas Telford, Distributed by American Society of Civil Engineers, New York.
28. Haynes F. D. and Karalius J. A. (1977). Effect of Temperature on the Strength of Frozen Silt. *CRREL Rep*, 77–3. [https://doi.org/10.1016/0148-9062\(78\)90991-9](https://doi.org/10.1016/0148-9062(78)90991-9).
29. Hermansson A. (2004). Laboratory and field testing on rate of frost heave versus heat extraction. *Cold Regions Science and Technology*, 38:137–151.
30. Hermansson A. and Guthrie W.S. (2005). Frost heave and water uptake rates in silty soil subject to variable water table height during freezing. *Cold Regions Science and Technology*, 43:128–139.
31. Hivon E.G. and Segó D.C. (1995). Strength of frozen soils. *Canadian Geotechnical Journal*, 32(2):336–354. <https://doi.org/10.1139/T95-034>.
32. Hjort J., Streletskiy D., Doré G., Wu Q., Bjella K., Luoto M. (2022). Impacts of permafrost degradation on infrastructure. *Nature Reviews Earth and Environment*, 3(1):24–38. <https://doi.org/10.1038/S43017-021-00247-8>.
33. Hooke R.L.B., Mellor M., Budd W.F., Glen J.W., Higashi A., Jacka T.H., Jones S.J., Lile R.C., Martin R.T., Meier M.F., Russell-Head D.S., Weertman J. (1980). Mechanical properties of polycrystalline ice: An assessment of current knowledge and priorities for research: Report prepared for the International Commission on Snow and Ice, with support from the U.S. National Science Foundation. *Cold Regions Science and Technology*, 3(4):263–275. [https://doi.org/10.1016/0165-232X\(80\)90033-6](https://doi.org/10.1016/0165-232X(80)90033-6).
34. Hooke R.L., Dahlin B.B., Kauper M.T. (1972). Creep of ice containing dispersed fine sand. *Journal of Glaciology*, 11(63):327–336. <https://doi.org/10.3189/s0022143000022309>.

35. Hu X.D., Wang J.T., Yu R.Z. (2013). Uniaxial compressive and splitting tensile tests of artificially frozen soils in tunnel construction of Hong Kong. *Journal of Shanghai Jiaotong University (Science)* 2013 18:6, 18(6):688–692. <https://doi.org/10.1007/S12204-013-1450-X>.
36. Johnston G.H. (1981). *Permafrost: engineering design and construction*. Wiley, New York.
37. Konrad J.M. (1999). Frost susceptibility related to soil index properties. *Canadian Geotechnical Journal*, 36(3):403–417. <https://doi.org/10.1139/t99-008>.
38. Konrad J.M. and McCammon A.W. (1990). Solute partitioning in freezing soils. *Canadian Geotechnical Journal*, 27(6):726–736. <https://doi.org/10.1139/T90-086>.
39. Konrad J.M. and Morgenstern N.R. (1980). A mechanistic theory of ice lens formation in fine-grained soils. *Canadian Geotechnical Journal*, 17(4):473–486. <https://doi.org/10.1139/t80-056>.
40. Konrad J.M. and Morgenstern N.R. (1981). The segregation potential of a freezing soil. *Canadian Geotechnical Journal*, 18(4):482–491. <https://doi.org/10.1139/t81-059>.
41. Ladanyi B. (1972). An engineering theory of creep of frozen soils. *Canadian Geotechnical Journal*, 9(1):63–80.
42. Ladanyi B. and Johnston G.H. (1973). Evaluation of in situ creep properties of frozen soils with the pressuremeter. *In Proceedings of the Second International Conference on Permafrost, January 1973*, pp:310–318.
43. Li H., Zhu Y., Zhang J., Lin C. (2004). Effects of temperature, strain rate and dry density on compressive strength of saturated frozen clay. *Cold Regions Science and Technology*, 39(1), 39–45. <https://doi.org/10.1016/J.COLDREGIONS.2004.01.001>.

44. Li S., Lai Y., Zhang M., Yu W. (2015a). Seasonal differences in seismic responses of embankment on a sloping ground in permafrost regions. *Soil Dynamics and Earthquake Engineering*, 76:122–135. <https://doi.org/10.1016/J.SOILDYN.2015.01.005>.
45. Li S., Zhang M., Tian Y., Pei W., Zhong H. (2015b). Experimental and numerical investigations on frost damage mechanism of a canal in cold regions. *Cold Regions Science and Technology*, 116:1–11. <https://doi.org/10.1016/J.COLDREGIONS.2015.03.013>.
46. Li S., Lai Y., Zhang M., Pei W., Zhang C., Yu F. (2019). Centrifuge and numerical modeling of the frost heave mechanism of a cold-region canal. *Acta Geotechnica*, 14(4):1113–1128. <https://doi.org/10.1007/S11440-018-0710-1>.
47. Linell K.A. and Kaplar C.W. (1966). Description and classification of frozen soils. *Corps of Engineers, U.S. Army, Cold Regions Research and Engineering Laboratory*.
48. Mageau D.W. and Rooney J.W. (1984). Thermal erosion of cut slopes in ice-rich soil. *Alaska Department of Transportation and Public Facilities, Division of Planning and Programming Research Section 2301 Peger Road, Fairbanks Alaska 99701*.
49. McRoberts E.C. and Morgenstern N.R. (1974). Stability of slopes in frozen soil, Mackenzie Valley, N.W.T. *Canadian Geotechnical Journal*, 11(4):554–573. <https://doi.org/10.1139/t74-058>.
50. Morgenstern N.R. and Price V.E. (1965). The analysis of the stability of general slip surfaces. *Geotechnique*, 15(1):79–93. <https://doi.org/10.1680/GEOT.1965.15.1.79>.
51. Muller S.W. (1947). Permafrost or permanently frozen ground and related engineering problems. J.W. Edwards, Ann Arbor, MI.

52. Nater P., Arenson L.U., Springman S.M. (2008). Choosing geotechnical parameters for slope stability assessments in Alpine permafrost soils. *9th International Conference on Permafrost, May 2015*, pp:1261–1266.
53. Nickling G. and Bennett L. (1984). The shear strength characteristics of frozen coarse granular debris. *Journal of Glaciology*, 30(106):348–357. <https://doi.org/10.3189/S0022143000006201>.
54. Niu F., Cheng G., Ni W, Jin D. (2005). Engineering-related slope failure in permafrost regions of the Qinghai-Tibet Plateau. *Cold Regions Science and Technology*, 42(3):215–225. <https://doi.org/10.1016/j.coldregions.2005.02.002>.
55. Parameswaran V.R. (1980). Deformation behavior and strength of frozen sand. *Canadian Geotechnical Journal*, 17(1):74–88. <https://doi.org/10.1139/T80-007>.
56. Sayles F.H. (1974). Triaxial constant strain rate tests and triaxial creep tests on frozen Ottawa sand. *US Army Corps of Engineers, Cold Regions Research and Engineering Laboratory*, Technical Report 253. [https://doi.org/10.1016/0148-9062\(75\)91294-2](https://doi.org/10.1016/0148-9062(75)91294-2).
57. Sayles F.H. and Carbee D.L. (1981). Strength of frozen silt as a function of ice content and dry unit weight. *Engineering Geology*, 18(1–4):55–66. [https://doi.org/10.1016/0013-7952\(81\)90046-6](https://doi.org/10.1016/0013-7952(81)90046-6).
58. Sayles F.H., ASCE M., Baker T.H.W., Gallavres F., Jessberger H.L., Kinoshita S., Sadovskiy A.V., Sego D., Vyalov S.S. (1987). Classification and laboratory testing of artificially frozen ground. *Journal of Cold Regions Engineering*, 1(1):22–48.
59. Sego D.C. and Morgenstern N.R. (1983). Deformation of ice under low stresses. *Canadian Geotechnical Journal*, 20(4):587–602. <https://doi.org/10.1139/T83-069>.
60. Siva Subramanian S., Ishikawa T., Tokoro T. (2017). Stability assessment approach for soil slopes in seasonal cold regions. *Engineering Geology*, 221:154–169. <https://doi.org/10.1016/J.ENGGEOL.2017.03.008>.

61. Stahli M. and Stadler D. (1997). Measurement of water and solute dynamics in freezing soil columns with time domain reflectometry. *Journal of Hydrology*, 195(1–4):352–369. doi:10.1016/s0022-1694(96)03227-1.
62. Su X., Wang B., Nichol S. (2006). Back Analysis of a Slope Failure in Permafrost in the Mackenzie Valley, Canada. *Proceedings of the 13th International Conference on Cold Regions Engineering*, 1–12. [https://doi.org/10.1061/40836\(210\)50](https://doi.org/10.1061/40836(210)50).
63. Sumgin M.I. (1927). Permafrost of soil in the limit of USSR, Moscow.
64. Sysala S., Cermak M., Koudelka T., Kruis J., Zeman J., Blaheta R. (2016). Subdifferential-based implicit return-mapping operators in computational plasticity. *ZAMM Zeitschrift Fur Angewandte Mathematik Und Mechanik*, 96(11):1318–1338. <https://doi.org/10.1002/zamm.201500305>.
65. Taber S. (1929). Frost heaving. *Journal of Geology*, 37:428–461.
66. Taber S. (1930). The mechanics of frost heaving. *Journal of Geology*, 38:303–317.
67. Ting J.M., Martin R.T., Ladd C.C. (1983). Mechanisms of Strength for Frozen Sand. *Journal of Geotechnical Engineering*, 109(10):1286–1302. [https://doi.org/10.1061/\(ASCE\)0733-9410\(1983\)109:10\(1286\)](https://doi.org/10.1061/(ASCE)0733-9410(1983)109:10(1286)).
68. van Everdingen R.O. (1998, revised May 2005). Multi-language glossary of permafrost and related ground-ice terms. *National Snow and Ice Data Center/World Data Center for Glaciology, Boulder, CO*.
69. von Baer K.E. (1838). The ground ice or frozen soil of Siberia. *Journal of the Royal Geographical Society London*, 8:210–213.
70. Voytkovskiy K.F. (1960). The mechanical properties of ice. *Izvestiya Akademii Nauk*.

71. Vyalov S.S. (1963). Rheology of frozen soil. *In Proceedings of the International Conference on Permafrost, National Academy of Sciences: National Research Council, Indiana, USA*, Publication 1287:332–339.
72. Vyalov S.S. and Tsytoovich S. (1955). Cohesion of frozen soils. *Doklady Akademii Nauk*, 104(4):527–529.
73. Wang J., Nishimura S., Tokoro T. (2017). Laboratory study and interpretation of mechanical behavior of frozen clay through state concept. *Soils and Foundations*, 57(2):194–210. <https://doi.org/10.1016/J.SANDF.2017.03.003>.
74. Washburn A.L. (1947). Reconnaissance geology of portions of Victoria Island and adjacent regions, Arctic Canada. *Geology Society of America*, Memoir 22.
75. Watanabe K. and Mizoguchi M. (2002). Amount of unfrozen water in frozen porous media saturated with solution. *Cold Regions Science and Technology*, 34(2):103–110. [https://doi.org/10.1016/S0165-232X\(01\)00063-5](https://doi.org/10.1016/S0165-232X(01)00063-5).
76. Wijeweera H. and Joshi R.C. (1990). Compressive strength behavior of fine-grained frozen soils. *Canadian Geotechnical Journal*, 27(4):472–483. <https://doi.org/10.1139/T90-062>.
77. Williams P.J. (1964). Unfrozen water content of frozen soils and soil moisture suction. *Geotechnique*, 14(3):231–246. <https://doi.org/10.1680/geot.1964.14.3.231>.
78. Williams P.J. (1967). Unfrozen water in frozen soils. *Publications of the Norwegian Geotechnical Institute*, 72:37–48.
79. Yang Y., Lai Y., Chang X. (2010a). Laboratory and theoretical investigations on the deformation and strength behaviors of artificial frozen soil. *Cold Regions Science and Technology*, 64(1):39–45. <https://doi.org/10.1016/J.COLDREGIONS.2010.07.003>.

80. Yang Y., Lai Y., Li J. (2010b). Laboratory investigation on the strength characteristic of frozen sand considering effect of confining pressure. *Cold Regions Science and Technology*, 60(3):245–250. <https://doi.org/10.1016/J.COLDREGIONS.2009.11.003>.
81. Yasufuku N., Springman S.M., Arenson L.U., Ramholt T. (2003). Stress-dilatancy behaviour of frozen sand in direct shear. *Proceedings of the 8th International Conference on Permafrost*, pp:1253–1258.
82. Yong R. (1962). Research on fundamental properties and characteristics of frozen soils. *Soil Mechanics Series No. 3. Paper Prepared for Presentation at First Canadian Conference on Permafrost, Ottawa, Canada, April 17 – 18, 1962*.
83. Yuanming L., Zhihua G., Shujuan Z., Xiaoxiao C. (2010). Stress-strain relationships and nonlinear Mohr strength criteria of frozen sandy clay. *Soils and Foundations*, 50(1):45–53. <https://doi.org/10.3208/SANDF.50.45>.
84. Yugui Y., Feng G., Yuanming L., Hongmei C. (2016). Experimental and theoretical investigations on the mechanical behavior of frozen silt. *Cold Regions Science and Technology*, 130:59–65. <https://doi.org/10.1016/J.COLDREGIONS.2016.07.008>.
85. Zhu Y. and Carbee D. L. (1984). Uniaxial compressive strength of frozen silt under constant deformation rates. *Cold Regions Science and Technology*, 9(1):3–15. [https://doi.org/10.1016/0165-232X\(84\)90043-0](https://doi.org/10.1016/0165-232X(84)90043-0).
86. Zienkiewicz O.C. and Taylor R.L. (2000a). The finite element method, Vol. 1: The basis. 5th edition, Butterworth-Heinemann.
87. Zienkiewicz O.C. and Taylor R.L. (2000b). The finite element method, Vol. 2: Solid mechanics. 5th edition, Butterworth-Heinemann.